EXPLORING THE CHALLENGES OF A FAR-INFRARED POST-DISPERSED POLARISING FOURIER TRANSFORM SPECTROMETER

ANTHONY IRVING HUBER
Bachelor of Science, Physics, University of Lethbridge, 2019

A thesis submitted
in partial fulfilment of the requirements for the degree of

MASTER OF SCIENCE

in

PHYSICS

Department of Physics and Astronomy
University of Lethbridge
LETHBRIDGE, ALBERTA, CANADA

EXPLORING THE CHALLENGES OF A FAR-INFRARED POST-DISPERSED POLARISING FOURIER TRANSFORM SPECTROMETER

ANTHONY IRVING HUBER

Date of Defence: August 4, 2021

Dr. D. Naylor Thesis Supervisor	Professor	Ph.D.
Dr. L. Spencer Thesis Examination Committee Member	Associate Professor	Ph.D.
Dr. C. Povey Thesis Examination Committee Member	Instructor	Ph.D.
Dr. K. Vos Chair, Thesis Examination Committee	Associate Professor	Ph.D.

Dedication

To my love, Tessa, and to my sources of joy: Soren, Reuben, and Nox.

Abstract

Recent advances in superconducting far-infrared (FIR) bolometer detectors have resulted in increases to their sensitivity of at least two orders of magnitude over broadband detectors flown on previous far-infrared spaceborne astronomy instruments. Such sensitivity means that observations employing a Fourier transform spectrometer (FTS) will require techniques to reduce the spectral bandwidth of a detector to limit the photon noise. The proposed SPICA SAFARI instrument employs grating spectrometers to post-disperse the light that has been modulated by a polarizing FTS onto a detector array: a post-dispersed polarizing FTS (PDPFTS). This thesis presents the development of a FIR PDPFTS consisting of a FTS and grating spectrometer. The challenges of phase correction given the narrow bandwidth of the PDPFTS were explored and a technique was developed for reliable phase correction. The results show that the PDPFTS works as predicted, and allows one to recover a broadband spectrum at high resolution.

Acknowledgments

First, I would like to thank my supervisor, Professor David Naylor, for his willingness to take me on the week I transferred to Lethbridge. You have been incredibly patient and supportive of me and my family through our abundance of struggles. You are truly a great educator and inspire me to share my knowledge and love of learning with those around me. You have truly changed the life of this simple broccoli farmer.

I would like to thank the members of my committee, Professor Locke Spencer and Dr. Chad Povey. Throughout both my undergraduate and Master's degrees you have both made yourselves available for numerous long discussions about my classes, experiments, and the challenges in raising a family as a student. Your advice on all of these fronts has greatly helped me become both a better scientist and father. Thank you most of all for your patience throughout these last four years.

I would like to thank the members of the Astronomical Instrumentation Group, without whom I surely would have struggled greatly. Thank you Brad Gom for your seemingly unlimited knowledge and patience. If I could be half of what you are, I would truly be a great scientist. Thanks to the many engineers who have propped me up along the way: Pawel Kapusta, Steve Zimmerman, and Matthew Buchan. I would especially like to thank Matthew for taking time from his busy schedule to proofread this thesis and provide figures for my public defense. Thank you, Jacob Groeneveld and Dr. Ian Veenendaal, for your support all these years. Thanks as well to Adam Christiansen for your help with all of my photonics needs and your willingness to painfully proofread my code when I was desperately stuck. Thank you as well to Greg Tompkins. Although you have long passed away, your work on the detector and photomixer have made my thesis possible and saved me more than once.

I would like to give a special thanks to Dr. Sudhakar Gunuganti and Trevor Fulton of Blue Sky Spectroscopy. You have both served as supervisors, teachers, and most importantly friends. Sudhakar, your example of meticulous notetaking and double checking everything has ensured that I have not caused too much damage to our test suite (except for one blackbody). Trevor, when I started my degree, I had almost no experience programming. You truly dragged me through the coals as I learned at an accelerated pace. Thank you for your patience and assistance.

Thank you to Alicia Anderson and Rebecca Sirota, my closest friends in Lethbridge. You have both at various times stayed late with me to set up experiments and collect data for my thesis. You are both examples of discipline and kindness, even though you are both stubborn to a fault. You are both beloved by my family, especially my children, and I thank you for being wonderful examples and friends.

I would like to thank my parents, Curtis and Susan Huber, and my parents-in-law, Roger and Joanne Jensen, for keeping me motivated, supporting me, and pretending to be interested whenever I talked about physics. Thank you to my numerous siblings and siblings-in-law, as well as my horde of nieces and nephews. I would especially like to thank my grandmother, Rita Moe, who unfortunately left us a week before my defense at the age of 95. You will be missed.

Thank you to Soren, my firstborn, whose passion for learning rivals my own. I love your creativity and enthusiasm, and you are an example of the best kind of learner. Throughout my degree we have spent our mornings reading books and fighting ghosts, often making me late for work. It was always worth it.

Thank you to Reuben, my second born, whose persistence and stubbornness is the perfect example of never giving up. I love your ability to make new best friends wherever you go. You never hesitate to speak your mind and tell everyone you love them. In the mornings you tried to physically block my way so I couldn't go to work, and rest assured I missed you every moment I was working.

Thank you to Nox, my third born, who is sweeter than a cherub. Throughout the pandemic your crib sat next to my desk. You were the perfect officemate throughout the entire year, keeping a strict schedule of naps punctuated with periods of the biggest smiles. Your chubby cheeks have kept me going through the most challenging of times. You are the perfect reminder of the rewards that come from temperance.

Lastly, I owe my eternal love and gratitude to my beautiful wife, Tessa. You have supported my decision to go back to school and have not faltered for even a moment. You are my rock, and none of this would have been possible without you. I am not nearly eloquent enough to convey the praises you deserve.

Contents

List of Tables

List of Figures

Chapter 1

Introduction

> In a restless search for new opportunities and new ways of living, the mystery and the promise of distant horizons always have called men forward.
>
> *Where the Skies End*
>
> STARSET

This chapter briefly explores the justification of the post-dispersed polarising Fourier transform spectrometer (PDPFTS). An introduction to far-infrared (FIR) astronomy is presented together with some challenges faced by making observations in this wavelength range. A review of previous spaceborne infrared observatories will be presented, and plans for the next generation of FIR missions will be discussed, with a focus on the Space Infrared Telescope for Cosmology and Astrophysics (SPICA). This thesis explores a prototype PDPFTS, an analogue of an instrument proposed for the SPICA mission.

1.1 Far-Infrared Astronomy

FIR astronomy plays a crucial role in our understanding of the Universe due to the fact that approximately half of all radiation which reaches Earth falls within the FIR and submillimetre wavelength range (30 - 1000 μm) [1]. This fact is the result of two mechanisms. Firstly, the Universe is full of cool dust and gas clouds which absorb radiation with a shorter wavelength and re-radiate at longer wavelengths (i.e., as infrared radiation), which is able to pass through the interstellar medium without being absorbed. The shorter wave-

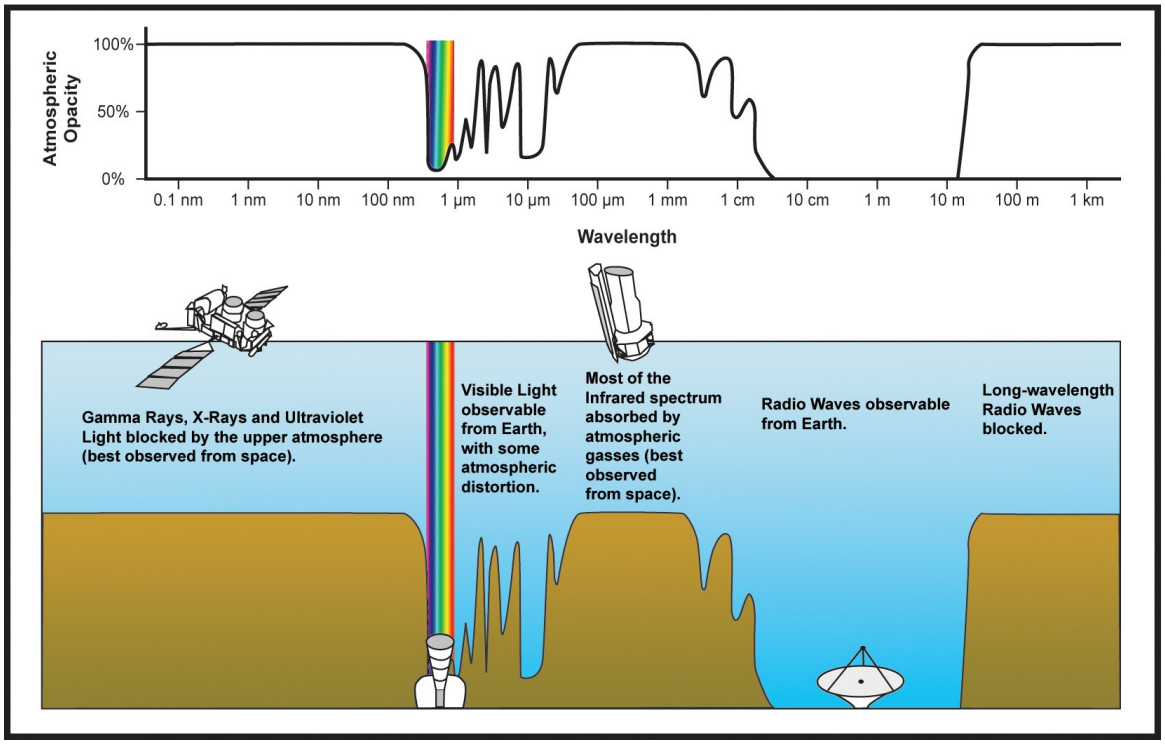

Figure 1.1: Opacity of the atmosphere across the electromagnetic spectrum. Visible light is represented by the rainbow. Note that with few exceptions the Earth's atmosphere is opaque to far-infrared radiation (FIR) [3].

length radiation, typically visible and ultraviolet light, arise from high energy conditions such as star formation regions which are embedded in cool dust, meaning FIR radiation observations can be used to probe such regions. Secondly, the accelerating expansion of the Universe results in a redshift in the emitted radiation from the distant Universe such that shorter wavelength radiation is shifted to longer wavelengths [2].

As shown in Figure 1.1, Earth's atmosphere is opaque to a majority of the electromagnetic spectrum, including the FIR. Much of this is due to the absorption of infrared radiation by atmospheric water vapour and carbon dioxide found in Earth's atmosphere [4]. Thus, to observe the FIR Universe, one must go above the atmosphere. For terrestrial observatories this means placing telescopes at high altitude locations with dry climates, such as the summit of Mauna Kea, Hawaii [5]. An alternative is the use of an airborne observatory, such as is used on the Stratospheric Observatory for Infrared Astronomy (SOFIA) [6]. However, to completely remove the effects of atmospheric extinction, the ideal FIR observatory must

be spaceborne.

In this thesis I utilize two general forms of spectral features: continua and lines. A spectrum is formed from any combination of these features, which may be observed as either emission or absorption. Continua are features associated with condensed matter or synchrotron radiation which are observed over a broad range of wavelengths, thus the spectra appear smooth and continuous [7]. On the other hand, spectral lines arise from gas (molecular, atomic, or ionic) which experiences a change in its net configurational energy (rotational, vibrational, or electronic) from one energy state to another, ΔE [7]. This change in energy corresponds to a particular frequency of light:

$$\Delta E = h\nu = \frac{hc}{\lambda} = hc\sigma, \qquad \text{[J]} \quad (1.1)$$

where h is *Planck's constant* (6.626×10^{-34} kgm^2/s), ν is the frequency of the radiation, c is the speed of light in vacuum, λ is the wavelength of the radiation, and σ is the wavenumber of the radiation.

When radiation is absorbed, the net energy of a system increases; when radiation is emitted, the net energy decreases. The energy levels of a given atom or molecule are unique to that entity, and transition between them can be used as a fingerprint to identify their existence in an astronomical source. For example, emission lines in a molecular cloud reveal the cloud's composition and can provide further information, such as the temperature, pressure, and velocity of particles in the cloud. These features are commonly used to characterize star-forming regions [7].

On the other hand, continuum features arise when the interaction of a large number of particles spread out the discrete emission lines such that they are no longer distinguishable. In general FIR continuum features are observed in warm dust and dense gas clouds, which emit blackbody radiation. Such clouds are generally warmed through collisional excitation or absorption of short wavelength radiation, and radiation is then emitted as the particles cool. The *spectral radiance* or intensity per unit wavelength, B_λ, is defined by the *Planck*

distribution [8]:

$$B_\lambda(\lambda, T) = \frac{2hc^2}{\lambda^5} \frac{10^{-6}}{e^{hc/\lambda kT} - 1}, \qquad [\mathrm{Wm}^{-2}\mu\mathrm{m}^{-1}\mathrm{sr}^{-1}] \quad (1.2)$$

where k is *Boltzmann's constant* (1.381×10^{-23} J/K), and T is the absolute temperature. The wavelength of the peak emission, λ_{peak}, is defined by the *Wien displacement law*, which is given as

$$\lambda_{peak} = \frac{b}{T}, \qquad [\mu\mathrm{m}] \quad (1.3)$$

where b is *Wiens's displacement constant* (2898 μmK). A series of Planck distributions in both frequency and wavelength for a cool dust cloud, body temperature, and the sun is shown in Figure 1.2.

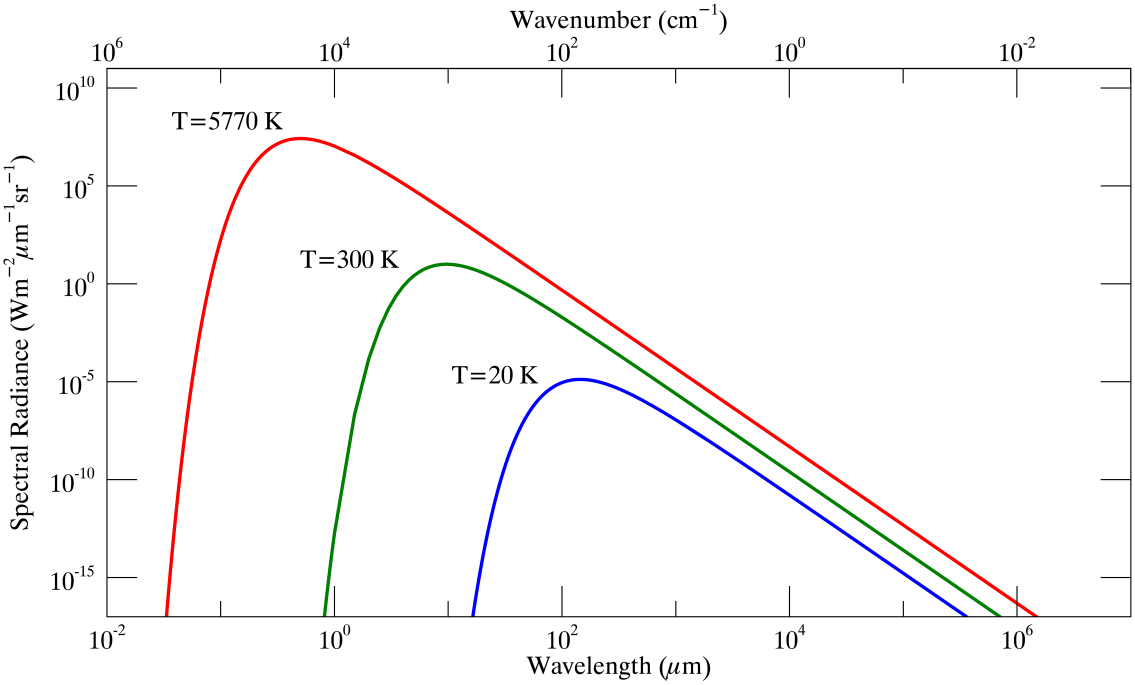

Figure 1.2: Planck distributions for a variety of blackbody temperatures. The peak of the distribution shifts to shorter wavelengths as the temperature increases. The blackbodies in increasing temperature represent a cool dust cloud, a human body, and the surface of the sun.

Beyond atmospheric extinction, FIR observations are also limited by background radiation emitted by the thermal emission of the telescope itself [9]. Thus, infrared observatories

require cryogenic cooling to be effective, which creates a trade-off between mirror size, which determines spatial resolution, and mirror temperature, which determines the sensitivity of the instruments. As shown in Figure 1.3, the first spaceborne observatory was the Infrared Astronomical Satellite (IRAS) launched in 1983, which featured a 57 cm telescope cooled to $<$10 K with detector optics cooled to $<$3 K [10]. Then, after more than a decade, the Infrared Telescope in Space (IRTS) was launched in 1995 [11] on the Space Flyer Unit. The IRTS featured a much smaller mirror than IRAS (15 cm), but was cooled with superfluid liquid helium to a stable temperature of 1.9 K. Later that same year, the European Space Agency (ESA) launched the Infrared Space Observatory (ISO) featuring a 60 cm mirror cooled to $\sim$4 K [12]. The Spitzer Space Telescope (Spitzer) then followed in 2003 with an 85 cm telescope cooled to roughly 5 K [13], which was then followed by Akari with a 68.5 cm telescope cooled to 6 K [14]. Each of these observatories provided remarkable data about the infrared universe, but none more so than the Herschel Space Observatory [15].

Since the size of the mirror dictates the spatial resolution, Herschel opted for a larger, warmer mirror, but with precise thermal modelling to counter the increased noise floor. Thus, Herschel, launched in 2009, was the largest infrared telescope to date, featuring a 3.5 m mirror. Due to its size, the passively cooled mirror was only able to reach a temperature of $\sim 85\ K$. Herschel included a mixture of high-resolution and low-resolution instruments: the Heterodyne Instrument for Far-Infrared (HIFI), the Photodetector Array Camera and Spectrometer (PACS), and the Spectral and Photometric Imaging Receiver (SPIRE). Of particular interest is SPIRE, which incorporated an imaging Fourier transform spectrometer (FTS) used to simultaneously observe the whole spectral band, providing key information on the physics of galaxy structure and formation at high redshift (i.e., radiation shifted into the FIR due to the expansion of the Universe) and of star formation within the interstellar medium [16]. Until 29 April, 2013, when its onboard supply of liquid Helium expired, Herschel studied some of the coldest and furthest objects in the universe, providing invaluable

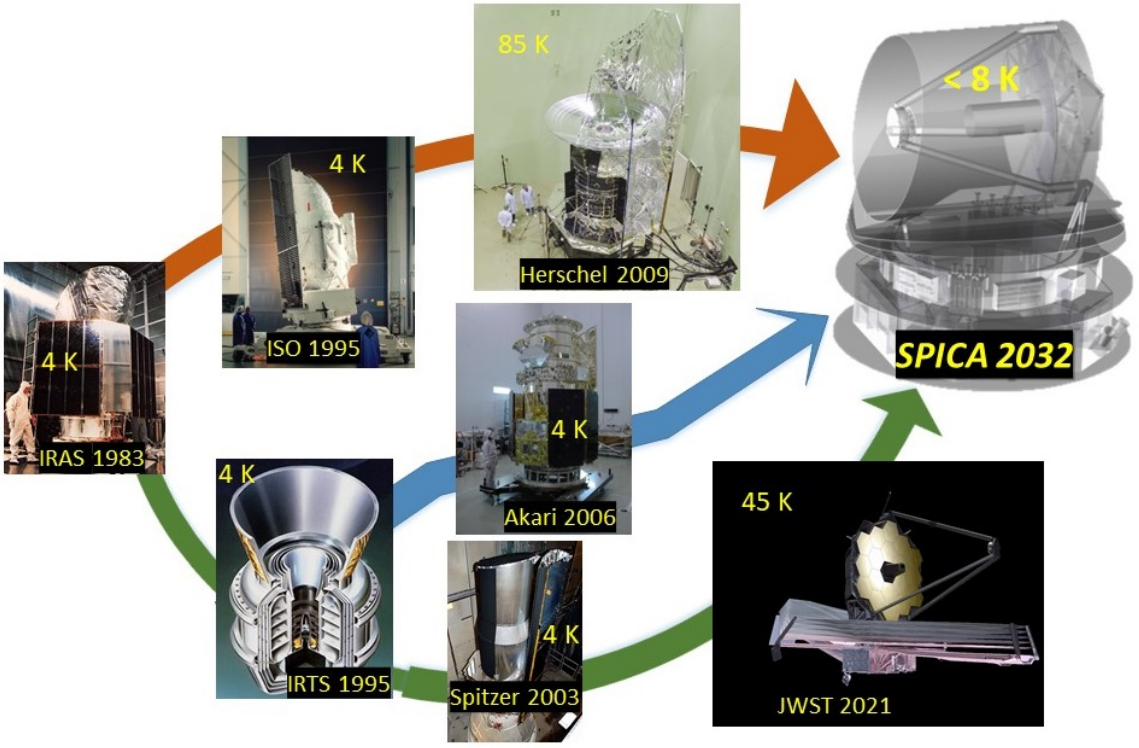

Figure 1.3: The development of spaceborne infrared observatories since 1983. Until the proposal of SPICA, an observatory was limited by either mirror size or mirror temperature. Orange represents the developments of the European Space Agency, blue represents the developments of the Japan Aerospace Exploration Agency, and green represents the developments of the National Aeronautics and Space Administration. (Credit: Peter Roelfsema, SRON).

information on the structure of stars, galaxies and interstellar regions [17, 18, 19], but there is still more to be learned.

The James Webb Space Telescope (JWST), is a near/mid-infrared space observatory which is planned to launch in late 2021 [20]. The JWST features four instruments covering a spectral range of 0.6 - 28.3 μm. The observatory features a 6.6 m primary mirror which will be passively cooled below 50 K, surpassing Herschel in both spatial resolution and sensitivity. The narrowness of the spectral band observed by JWST requires further missions to explore the remainder of the infrared spectrum, the foremost of the proposed missions was SPICA [21], a collaboration between ESA and the Japan Aerospace Exploration Agency (JAXA), with support from both the National Aeronautics and Space Administration (NASA) and the Canadian Space Agency (CSA).

1.2 SPICA

SPICA was designed to incorporate both a large (2.5 m) and cryogenic cooled (<8 K) primary mirror [22]. In order to achieve both, the observatory was designed to include a combination of passive and mechanical coolers rather than using liquid cryogens as was done in the past. The use of mechanical coolers would extend the lifetime of the mission as the system would not be limited by the supply of cryogens. With low thermal emission and state-of-the-art detectors, SPICA promised huge advances on the capabilities of all previous infrared missions. SPICA was selected as one of three finalists for the M5 call of ESA [23], but was unexpectedly cancelled in October 2020 [24]. This decision by ESA led to an unprecedented response from the broad scientific community [25]. However, the technology and concepts developed for SPICA will prove useful for future FIR observatories.

The SPICA Far-infrared Instrument (SAFARI) was one of three instruments proposed for the SPICA observatory, along with the SPICA Mid-infrared Instrument (SMI) and B-fields with Bolometers and Polarizers (B-BOP). SAFARI was designed to use an imaging FTS for wide-band spectroscopic mapping, similar to Herschel, though with an increase in the overall instrument sensitivity of over two orders of magnitude [26]. However, the inclusion of a high-resolution spectrometer in tandem with a new generation of ultra-sensitive detectors (Noise Equivalent Power (NEP) $\sim 10^{-19}$ W/$\sqrt{\text{hz}}$) presents a new challenge: the multiplex advantage (see Chapter 2) becomes a disadvantage unless the spectral bandpass of the instrument can be limited. The solution proposed for SAFARI is to use a diffraction grating as a post-dispersing element which disperses light modulated by a polarising FTS onto an array of detectors, a PDPFTS. Under the leadership of my supervisor, Canada was responsible for the development of the scan mechanism for the FTS of the SPICA SAFARI instrument. While the principles of the PDPFTS are understood, an integrated system has never before been realized and tested under cryogenic conditions. This thesis presents the development of a PDPFTS, an analogue of SAFARI, to explore the challenges presented by this novel instrument.

1.3 Thesis Overview

This chapter presented the motivation for the design and characterization of a FIR PDPFTS as a demonstrator for the SPICA SAFARI instrument. The fundamentals of Fourier transform spectroscopy are described in Chapter 2 with emphasis given to some of the challenges predicted for the PDPFTS, particularly phase correction. Chapter 2 is supplemented by Appendices A and B, which respectively show the derivation of the Fourier transform and provide insight into the process of phase correction. Note that the abbreviation *FTS* will be used interchangeably to mean either Fourier transform spectroscopy and Fourier transform spectrometer, where spectroscopy is the study of how radiated energy and matter interact and a spectrometer is the instrument used [27]. Chapter 3 outlines the theory and design of a prototype PDPFTS, including a cryogenic grating spectrometer [28], an FTS provided by an industrial partner [29], and the extensive test suite used to characterize the PDPFTS. This chapter is supplemented by Appendix C, which outlines the calibration of the laser diodes used in the test suite.

With an understanding of the theory and design of the prototype PDPFTS, Chapter 4 presents a theoretical simulator for the PDPFTS system with the threefold purpose of exploring potential issues in the analysis of data obtained from a PDPFTS, informing the design of a data processing pipeline, and producing theoretical spectra to compare with experimental data. Results obtained from the world's first FIR PDPFTS are presented in Chapter 5. Chapter 6 summarizes the thesis and discusses ongoing and future work in the development of a cryogenic PDPFTS.

Chapter 2

Fourier Transform Spectroscopy

> It is here that the science of measurement shows its importance — where quantitative work is more to be desired than qualitative work. An eminent physicist remarked that the future truths of physical science are to be looked for in the sixth place of decimals.
>
> *Dedication of Ryerson Physical Laboratory*
>
> ALBERT A. MICHELSON

This chapter provides the theoretical background of Fourier Transform Spectroscopy (FTS) that will be used throughout this work. A review of the basic principles and standard practices used for the FTS is required to understand the operation of the post-dispersed polarizing FTS (PDPFTS). As will be seen, the concepts in this chapter will extend into both the realm of instrumentation design and spectral analysis. These concepts will appear throughout this thesis as they apply to the PDPFTS.

2.1 Introduction

Fourier analysis was first introduced over 200 years ago by Jean-Baptiste Joseph Fourier when he made the claim in 1807 that continuous and discontinuous functions may be defined as a series of sine and cosine terms [30, 31]. While his work aimed to model heat flow through a pipe, later work showed its application in other systems, such as optics. Fourier's claim proved to be controversial at the time and Fourier struggled for 15 years to publish his work due to what some believed to be a lack of rigour [32]. Fortunately, in 1829 a friend

and colleague of Fourier by the name of Peter Gustave Lejeune-Dirichlet published a set of conditions under which the sum of the Fourier series will converge [33]. These conditions in tandem with Fourier's theorem provided the foundation for what is now known as the *Fourier Transform* (FT). For the derivation of the FT and a summary of its useful properties, the reader is referred to Appendix A. The FT and the *inverse Fourier Transform* (iFT) are respectively

$$\widetilde{f}(\sigma) = \mathscr{F}[f(x)] = \int_{-\infty}^{\infty} f(x) e^{-i2\pi\sigma x}\, \mathrm{d}x, \qquad [\mathrm{cm}^{-1}] \quad (2.1)$$

and

$$f(x) = \mathscr{F}^{-1}[\widetilde{f}(\sigma)] = \int_{-\infty}^{\infty} \widetilde{f}(\sigma) e^{i2\pi\sigma x}\, \mathrm{d}\sigma. \qquad [\mathrm{cm}] \quad (2.2)$$

The FT and its inverse define the relationship between the spatial and spectral domains [27, 34, 35]. This relation between the spatial and spectral domains allows for the manipulation and analysis of a waveform in either domain, a property that is invaluable in Fourier analysis.

With the invention of the interferometer, Albert Abraham Michelson founded the field of Fourier Transform Interferometry in the late 1800s [36, 37], nearly 100 years after the introduction of Fourier analysis. Michelson's later work formed the basis of FTS [38, 39], though he was unable to explore the intricate techniques of spectroscopy due to a lack of computational power [40, 27]. Without computers the spectra were estimated, and an interferogram was then calculated and compared against the measured interferograms.

With the advent of digital computing and methods of rapidly determining FTs, specifically the Fast Fourier Transform (FFT) algorithm [41], the field of FTS began to flourish. In 1966 Connes and Connes published the first work to apply FTS to astronomical observations [42, 43]. Since then the techniques associated with FTS have gained broader acceptance across the science disciplines, with FTS being used as a tool in a range of scientific and industrial applications. In astronomy, the FTS has become an indispensable tool

in the instrument suites of numerous ground-based and space-based observatories [16, 44].

2.2 Fourier Theorems

There are several theorems that are fundamental to Fourier analysis. This section outlines three of the most important which have been used throughout this thesis. These theorems are the *superposition theorem*, *Parseval's theorem*, and *convolution theorem*.

2.2.1 Superposition Theorem

The FT obeys the superposition theorem, which states that for a linear system with two or more inputs the result is the sum of the response for each individual input. The superposition theorem as it applies to the FT is represented as

$$\mathscr{F}[f(x)+g(x)] = \mathscr{F}[f(x)] + \mathscr{F}[g(x)] = \widetilde{f}(\sigma) + \widetilde{g}(\sigma). \tag{2.3}$$

An example of the superposition theorem is given in Figure 2.1 for the summation of two cosine functions and their corresponding delta functions.

2.2.2 Parseval's Theorem

Parseval's theorem describes the relationship between a function and its transform. The theorem states that the integral of the autocorrelation of a function is proportional to the integral of the autocorrelation of its transform [45]. Parseval's theorem is in essence an expression of the conservation of energy of a signal; the energy of a finite signal is identical when calculated in either domain [32]. The signal energy, U, for a finite signal, $f(x)$ is

$$U = \int_{-\infty}^{\infty} |f(x)|^2 \, \mathrm{d}x = \int_{-\infty}^{\infty} |\widetilde{f}(\sigma)|^2 \, \mathrm{d}\sigma. \qquad \text{[J]} \tag{2.4}$$

The total energy of the system is defined by U. However, it is possible to explore the energy contained within a finite portion of the band. Consider a small band of width $\Delta\sigma$.

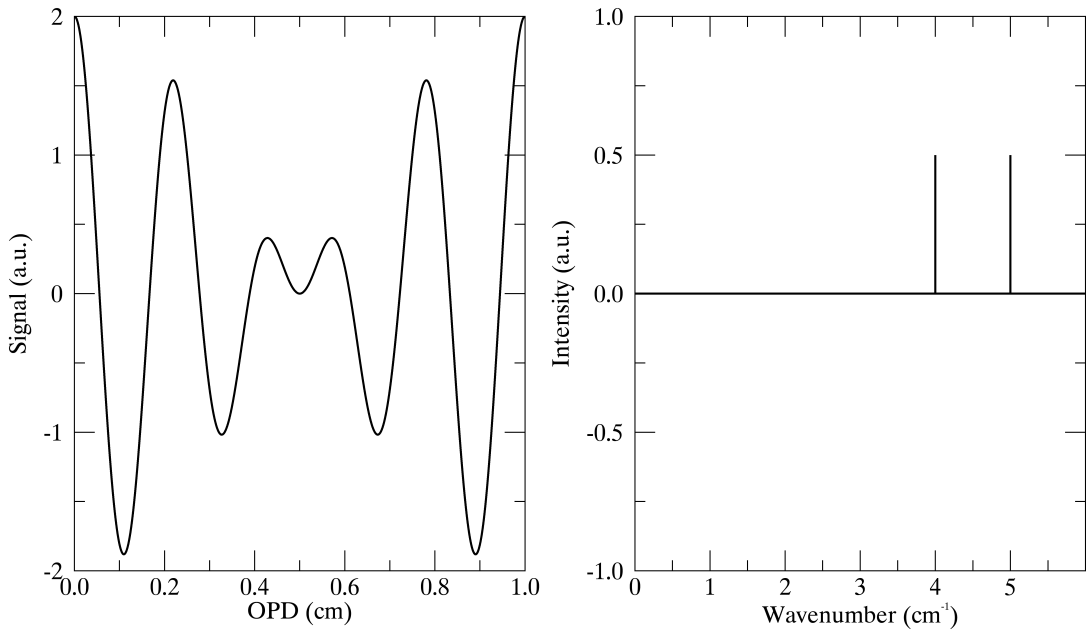

Figure 2.1: Superposition theorem applied through a Fourier transform. Panel a) shows the superposition of two cosine functions with frequencies of $\sigma_1 = 4\ cm^{-1}$ and $\sigma_2 = 5\ cm^{-1}$. Panel b) depicts the Fourier transform of the given summation as the sum of the corresponding delta functions for positive wavenumbers.

The energy within a band centred at a point σ_0 is defined as:

$$\Delta U(\sigma_0) = |\widetilde{f}(\sigma_0)|^2\, \Delta\sigma. \qquad \text{[J]} \quad (2.5)$$

Thus, $|\widetilde{f}(\sigma)|^2$ is proportional to the *energy spectral density*, or energy per unit bandwidth.

2.2.3 Convolution and Correlation Theorems

Convolution is a mathematical operation defined by Equation 2.6. This can be understood as two functions, one which is held fixed and the other is reversed and scanned across the fixed function; the two functions are multiplied together and the integral of the product of the overlapping region is taken. The process of convolution can be easily visualized in the example shown in Figure 2.2.

$$h(z) = f * g = \int_{-\infty}^{\infty} f(x)g(z-x)\ \mathrm{d}x, \qquad (2.6)$$

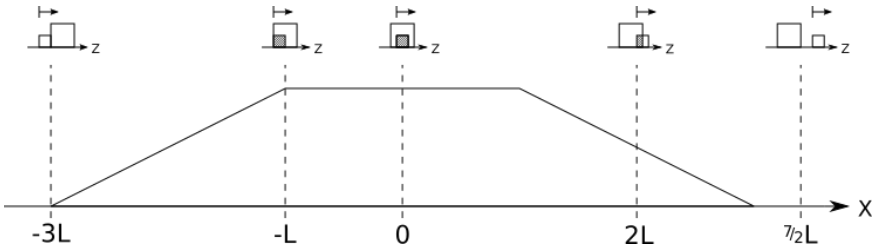

Figure 2.2: Convolution of two boxcar functions. The trapezoid is the result of the convolution of two boxcar functions with differing widths. The upper portion shows the integration over z for each point in x. The arrow indicates the direction of the shifting boxcar function and the hatched region indicates the overlapping area of the two boxcar functions.

where z and x refer to the same physical variable, but are represented differently due to differing roles in the analysis [35, 27]. From Equation 2.6, it is clear that the convolution is commutative ($f * g = g * f$), associative $(f * g) * k = f * (g * k)$), and distributive ($f * (g + k) = f * g + f * k$). The convolution integral may also be defined for a discrete system:

$$h[n] = \sum_{m=-\infty}^{\infty} f[m]g[n-m] = \sum_{m=-\infty}^{\infty} f[n-m]g[m], \tag{2.7}$$

where the commutative nature has been included [46]. In practice observations are finite, thus the convolution can be applied under the assumption that functions are periodic. An example of the convolution of two boxcar functions with different widths is given in Figure 2.2.

Correlation, a mathematical operation closely related to convolution, provides a quantitative measure of the similarity of two functions as one is displaced relative to the other. The correlation operation, similar to convolution, is defined by an integral of the product of overlapping regions for two functions after one is shifted. The difference is that in a correlation neither function is reversed. Correlation is called cross-correlation when $f \neq g$, and auto-correlation when $f = g$. The integral form of the correlation operator is given by

$$h(z) = f \otimes g = \int_{-\infty}^{\infty} f'(x)g(z+x)\,\mathrm{d}x, \tag{2.8}$$

where $'$ indicates the complex conjugate [35, 47]. Similar to the convolution operation, the

correlation operation is associative and distributive. Correlation, however, is in general not commutative, giving a relation of:

$$[f \otimes g](z) = [g \otimes f]'(-z). \tag{2.9}$$

Similar to the convolution integral, the correlation integral may also be defined for a discrete system:

$$h[n] = \sum_{m=-\infty}^{\infty} f'[m]g[n+m]. \tag{2.10}$$

Note the similarities between Equations 2.7 and 2.10. Computationally, the same algorithm may be used to compute discrete convolution and correlation with the exception of reversing one input for the convolution. However, if g is symmetric then reversing the input is redundant and the two operations are identical.

2.3 The Michelson Interferometer

The results presented in this thesis are based upon the Michelson interferometer, which is a two-beam interferometer that measures interferograms which may then be converted to spectra via the FT [36]. A Michelson interferometer operates on the principle of amplitude division. Upon encountering the beamsplitter, the incident beam is divided into two beams, which travel along independent paths within the interferometer. Upon reflecting, the two beams are recombined at the beamsplitter, where interference occurs [48]. The two resulting beams traverse different optical paths within the interferometer back to the beamsplitter. The beams then recombine and are brought to focus on the detector and, based on the *optical path difference* (OPD), interference occurs. The path of light through a Michelson interferometer is shown in Figure 2.3, where Δx represents the path difference between the two arms of the interferometer. The OPD is defined as twice the difference between these two values. Traditionally, the OPD is varied by moving the translating mirror while the second arm typically has a mirror that remains stationary. It is worth noting that the beam-

splitter allows for half the light to be transmitted back to the source, reducing the overall efficiency of the system [40, 27].

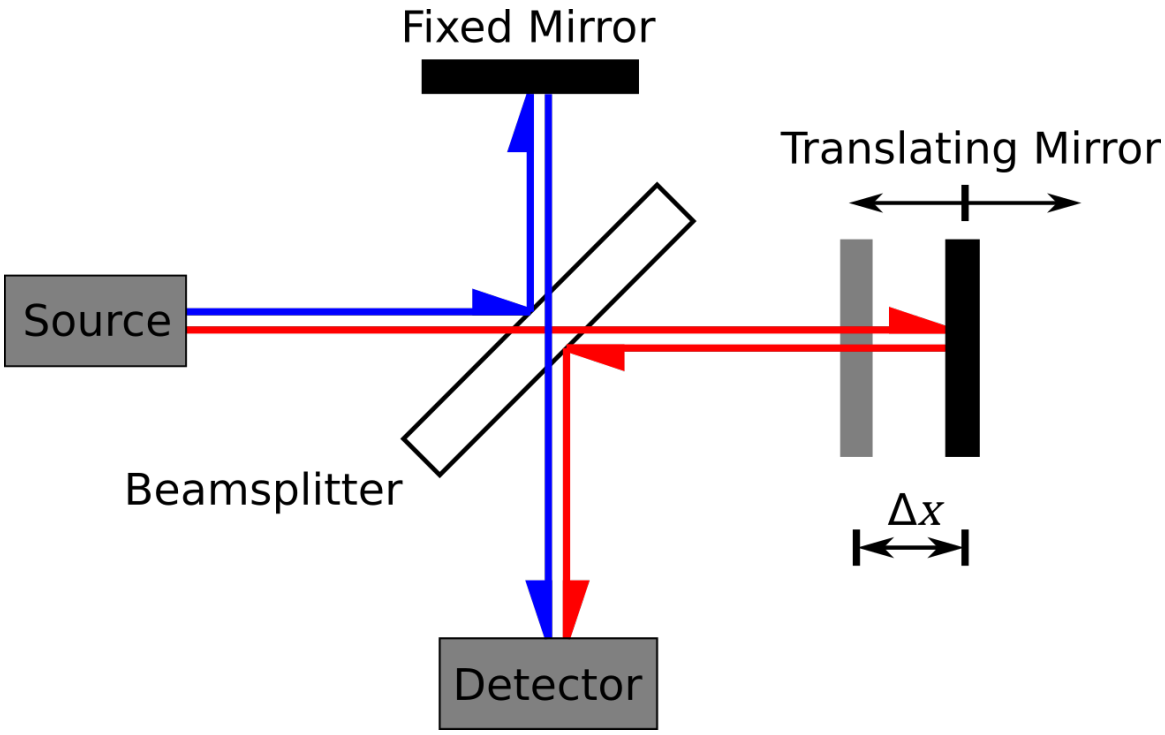

Figure 2.3: Simplified schematic of a Michelson interferometer. The OPD is twice the shift in position of the translating mirror, Δx. The difference in path length, adjusted by moving the translating stage, determines the degree of constructive or destructive interference incident on the detector.

The point of symmetry occurs when OPD = 0, known as *zero path difference* (ZPD). This position is of particular interest as it indicates that the mirrors are equidistant from the beamsplitter. Since the OPD is zero, each beam travels exactly the same distance, meaning that all wavelengths of light are in phase. Thus the two recombined beams are perfectly in phase regardless of wavelength. This gives rise to the peak intensity at ZPD [48].

In reality there is no ideal interferometer, thus the characteristics of the components must be considered. The beamsplitter must be explored as the properties of the beamsplitter may modify the OPD based on transmission and reflection of the beams, and therefore the output. Two types of output exist: balanced and unbalanced (See Figure 2.4). In the ideal case the system is balanced, implying each beam undergoes external reflection at the

beamsplitter once. The result is no difference in OPD when the mirrors are equidistant and constructive interference occurs. Dispersion, or the frequency-dependent nature of the refractive index of a substrate material, implies that a perfectly balanced system is not possible. The use of a compensating plate may be used to correct the effects of dispersion. However, even with a compensating it is extremely difficult to achieve a perfectly balanced system due to thickness variations and surface errors in the plates.

An unbalanced system, conversely, results when one beam undergoes an external reflection, while the other does not. The result is an overall shift in phase ideally equal to π on only one beam, a result of external reflection. In practice due to the complex nature of the index of refraction the true phase shift differs from π in a way that is difficult to predict. As will be shown later there are methods to compensate for phase correction in post processing, but for now the system is assumed to be balanced.

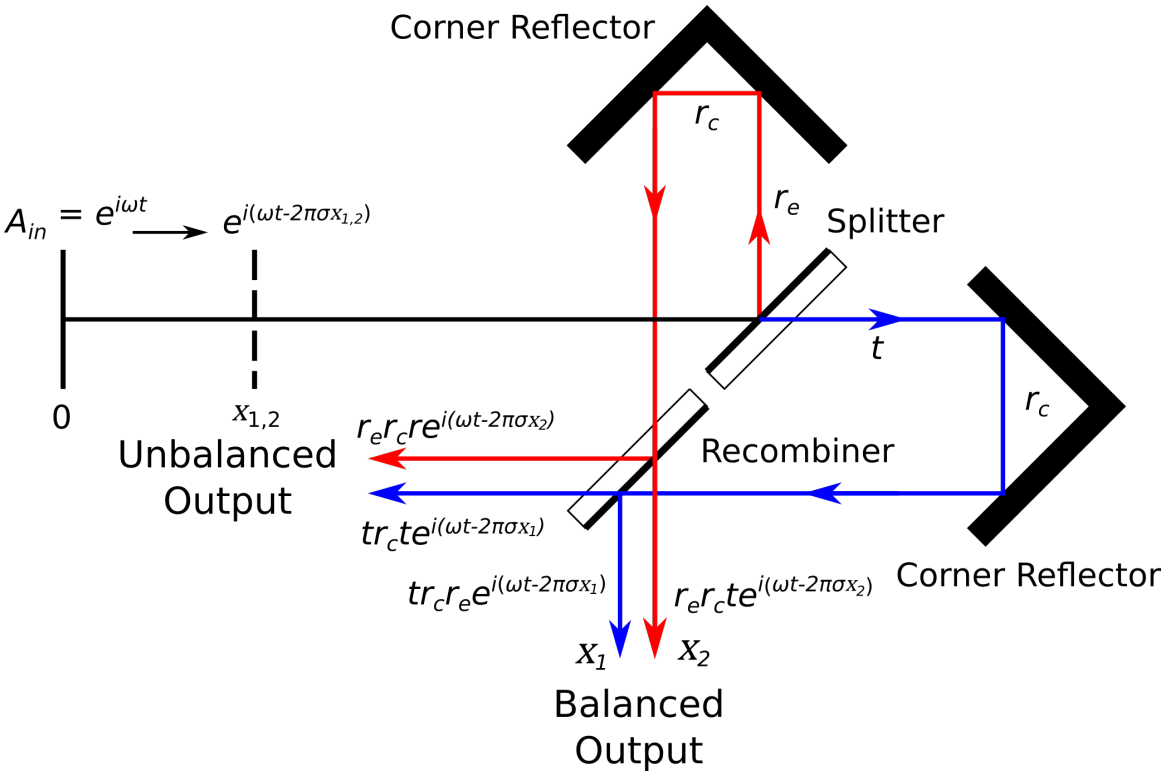

Figure 2.4: Configuration of a Michelson interferometer depicting both a balanced and unbalanced output. r_e is the external amplitude coefficient of the beamsplitter and recombiner, r_i is the internal amplitude coefficient of the recombiner, r_c is the reflection coefficient of the corner reflectors, and t is the transmission coefficient of the beamsplitter and recombiner.

The amplitude of the recombined wave, A, for a balanced output based on incident monochromatic light of unit amplitude is:

$$A \propto e^{i\omega t} r_e r_c t (e^{i2\pi\sigma x_1} + e^{i2\pi\sigma x_2}), \tag{2.11}$$

where r_e is the external amplitude coefficient of the beamsplitter and recombiner, r_c is the reflection coefficient of the corner reflectors, and t is the transmission coefficient of the beamsplitter and recombiner. The intensity, I, defined as the autocorrelation of the incident field, of the balanced output can be defined as

$$I = |A|^2 \propto 2R_e R_c T (1 + \cos[2\pi\sigma x]), \tag{2.12}$$

where $R_e = r_e^2$ and $R_c = r_c^2$ are intensity reflection coefficients, $T = t^2$ is the transmission coefficient, and the OPD (x) is equal to $x_1 - x_2$ [49]. These parameters may be further summarized into defining characteristics of an interferometer, the efficiency in particular. For simplicity, let $\eta_o = R_c$ be defined as the optical efficiency, and $\eta_b = 4R_eT$ as the beamsplitter efficiency. The overall efficiency is then $\eta = \eta_o \eta_b$ [27]. The result is given as

$$I(x) \propto \eta \left(\frac{1 + \cos(2\pi\sigma x)}{2} \right). \tag{2.13}$$

The ideal instrument has no losses to absorption or scattering. The implication is that $R_e + T = 1$ and therefore $\eta_b = 4R_e(1 - R_e)$. Intuitively, the maximum beamsplitter efficiency of 100% is achieved when exactly half the light is reflected and half is transmitted. Due to the hyperbolic relationship between reflection and transmission, the system is efficient even with relatively low reflection.

As an example, consider a beamsplitter with a reflection coefficient of 0.2. This value corresponds to a transmission coefficient of 0.8. The beamsplitter efficiency, or modulation efficiency, is given as $\eta_b = 4 \times 0.2(1 - 0.2) = 0.64$, or 64%. Thus, a relatively low reflection

coefficient is more than 50% efficient. However, the implication of a low efficiency beamsplitter implies that only 40% of the photons are modulated by the FTS. The actual energy falling on the detector includes both the modulated and unmodulated photons. In the era of photon counting detectors, the excess 60% of unmodulated photons produce unwanted photon noise (see Section 2.4.1). Since the signal of interest is contained in the modulated component of the interferogram, the goal is always to achieve maximum beamsplitter efficiency.

2.3.1 Polychromatic Light

Thus far the interferometer has assumed the input light was monochromatic with unit amplitude. In reality most sources emit more than one frequency of light. With no loss of generality Fourier analysis can be applied to a polychromatic source with varying amplitude. The analysis is based on the signal in a spectral interval, defined as $B(\sigma)\mathrm{d}\sigma$. While there is a DC term present in the measured signal, since the information sought by a FTS is contained in the AC term, it is common practice to neglect the DC term and express the only the frequency dependent term. This frequency dependent function corresponds to the detected AC signal, $\mathrm{d}I(x)$, for a given OPD value x [27]. The result is given as

$$\mathrm{d}I(x) = B(\sigma)\cos(2\pi\sigma x)\ \mathrm{d}\sigma, \qquad [\mathrm{W/m^2}] \quad (2.14)$$

which may be integrated to yield the signal detected as a function of OPD:

$$I(x) = \int_{-\infty}^{\infty} B(\sigma)\cos(2\pi\sigma x)\ \mathrm{d}\sigma. \qquad [\mathrm{W/m^2}] \quad (2.15)$$

To recover the spectral distribution $B(\sigma)$, the inverse transform of the interferogram is taken:

$$B(\sigma) = \int_{-\infty}^{\infty} I(x)\cos(2\pi\sigma x)\ \mathrm{d}x. \qquad [\mathrm{W/cm^{-1}}] \quad (2.16)$$

Since $\cos(2\pi\sigma x) = \cos(-2\pi\sigma x)$, therefore $B(\sigma) = B(-\sigma)$. The negative values produced

for the spectral distribution are non-physical, though the inclusion of these values provides the requisite symmetry for transforming between spatial and spectral domains, and also allowing for the examination of phase information. The transformation requires the integral to extend over all frequencies from $-\infty$ to ∞. For a spectrum comprised of the positive wavenumbers, an even valued spectrum can be obtained by modifying the definition of the spectral distribution to

$$B_e(\sigma) = \frac{1}{2}[B(\sigma) + B(-\sigma)]. \qquad [\mathrm{W/cm^{-1}}] \quad (2.17)$$

This modification can be applied to Equations 2.15 and 2.16 with the inclusion of all frequencies:

$$I(x) = \int_{-\infty}^{\infty} B_e(\sigma)\cos(2\pi\sigma x)\,\mathrm{d}\sigma, \qquad [\mathrm{W/m^2}] \quad (2.18)$$

$$B_e(\sigma) = \int_{-\infty}^{\infty} I(x)\cos(2\pi\sigma x)\,\mathrm{d}x. \qquad [\mathrm{W/cm^{-1}}] \quad (2.19)$$

The result is a set of symmetric functions that will produce spectra from measured interferograms, or vice versa [27]. Here the notation has been shifted from $f(x)$ to $I(x)$, and its transform pair $\widetilde{f}(\sigma)$ to $B(\sigma)$. This change reflects the notation common for FTS and will be used throughout the remainder of this work.

2.3.2 Multiplex Advantage

The multiplex advantage of the FTS, also known as the Fellgett advantage, is an improvement to the signal-to-noise ratio (SNR - see Section 2.4.1) from making multiplexed measurements rather than measuring individual frequencies. The multiplex advantage was first recorded by Fellgett in his PhD dissertation [50], which he later expanded upon [51]. The principles of the multiplex advantage may be explained as follows.

Consider a spectral interval between the wavenumbers σ_1 and σ_2 with a resolution of

$\delta\sigma$. The number of spectral elements, M is defined as

$$M = \frac{\sigma_2 - \sigma_1}{\delta\sigma} \equiv \frac{\Delta\sigma}{\delta\sigma}. \tag{2.20}$$

If a diffraction grating is used, then every element with a width of $\delta\sigma$ can be observed for a time T/M, where T is the total time required to scan the spectrum from σ_1 to σ_2. The integrated signal from these narrow bands are then proportional to T/M. If noise in the system is random and independent from the strength of the signal, then the noise level will be proportional to $(T/M)^{1/2}$. Thus the SNR for a diffraction grating will be [40]:

$$SNR_G \sim (T/M)^{1/2}. \tag{2.21}$$

On the other hand, for an FTS all the elements of width $\delta\sigma$ between σ_1 and σ_2 are measured simultaneously over the same span of time. In such a case the integrated signal strength will be proportional to T, and the noise will be proportional to $T^{1/2}$. Therefore, the SNR for an interferometer will be [40]:

$$SNR_I \sim T^{1/2}. \tag{2.22}$$

Assuming the coefficients of proportionality are identical from comparable throughput, these relations define the relation between the SNR of the interferometer and diffraction grating, given as

$$\frac{SNR_I}{SNR_G} = M^{1/2}. \tag{2.23}$$

From Equation 2.23 it is clear that the interferometer has a greater SNR than the diffraction grating. However, recall the assumption that the noise is random and independent of the signal.

When the field of spectroscopy first emerged, infrared detectors were not sensitive and therefore dominated the noise budget. Detector technology has advanced such that infrared

detectors are now approaching the quantum limit. When the noise in the signal is proportional to the square root of the source intensity, i.e., the photon noise, not only is the multiplex advantage lost, but it actually becomes a disadvantage [40, 27]. The multiplex disadvantage arises from the photon noise from each element of width $\delta\sigma$ being combined for the interferometer.

The spectral bandwidth could be reduced by using a bandpass filter. However, the width of such filters is typically limited to 10%. The bandwidth could be reduced further using a dispersion system, in which case bandwidths less than 1% are achievable. The path forward utilizes a hybrid of both a FTS to provide high spectral resolving power and grating spectrometer to reduce the bandwidth incident on a detector. As outlined in Chapter 3, such is the design of the PDPFTS used in this thesis. By incorporating an array of detectors, the multiplex advantage is restored.

2.4 Sampling an Interferogram

The measurement of intensity as a function of frequency or wavelength, is the basis of every type of spectrometer. For an interferometer the intensity distribution across all wavelengths may be measured simultaneously by a single detector. As shown above, the interferogram is related to the radiation field by Equation 2.15. The interferogram, $I(x)$, must be sampled at each position x. From Equation 2.16 the sampled interferogram encodes the spectral data and is decoded through the use of Fourier analysis.

The shifting in intensity from variations in light fringes produces an interferogram, which is a measurement of the signal intensity at a given OPD: a result of the interference of all wavelengths contained within the optical beam which reach the detector [27]. In a FTS the spectral data is encoded within the sampled interference pattern and is decoded though the use of Fourier analysis. As an example see Figure 2.1, which depicts a sample interferogram consisting of two wavelengths of equal intensity and the resulting spectrum of two lines.

Real-world application of an FTS is more complicated than the ideal system described in Section 2.3. This section explores the limitations of a non-ideal system.

2.4.1 Noise

In general, all scientific instruments produce noise. For an FTS, noise is superimposed on the true signal and can come from many sources such as noise in the source, noise in the motion, vibration, etc. The ratio of noise to the true signal gives the SNR. As derived by Davis *et al.* [27], the SNR for an interferogram, SNR_x, is defined as

$$SNR_x = \frac{I(0)}{\varepsilon_x} \tag{2.24}$$

for the interferogram with ε_x defined as the noise in the spatial domain. The SNR for a spectrum, SNR_σ, is calculated as

$$SNR_\sigma = \frac{B(\sigma)}{\varepsilon_\sigma} = \sqrt{\frac{2}{N}}\frac{B(\sigma)}{\overline{B_e}} \tag{2.25}$$

where ε_σ is the noise in the spectral domain, $\overline{B_e}$ is the mean signal in the spectral domain, and N is the total number of data points. For uniformly distributed noise independent on local signal strength, the relationship of the noise between the two domains is given as

$$\varepsilon_\sigma = \varepsilon_x\sqrt{\frac{L}{\sigma_{Ny}}}, \qquad [\mathrm{W/cm^{-1}}] \tag{2.26}$$

where L is the maximum OPD, σ_{Ny} is the Nyquist frequency, and ε_σ is considered for only the real part of the spectrum. This relation accounts for the fact that half the noise power is in the imaginary portion of the spectrum [27].

When the SNR is low, it is possible for a signal to be lost or misinterpreted. Consequently, the level of noise in a system determines how small a signal may be while providing useful information [52]. The SNR_σ may be predicted in detail looking at all the noise

contributions of the subsystems [53]. Though many types of noise exist in an FTS, such as environmental noise, OPD noise, and cosmic rays, the two types discussed in this work are *optical noise* and *electrical noise*.

Optical Noise

There are two dominant sources of optical noise: *photon noise* and *source noise*. Detectors are becoming so sensitive that photon noise is now a major issue which is why post-dispersing systems are being explored. Photon noise arises due to statistical fluctuations in the rate of arrival of photons. Thus for n photons collected, the resulting noise is $\varepsilon_x = \pm\sqrt{n}$. In state-of-the art FTS, photon noise dominates and the FTS is then photon noise limited. The result is an increase in the *noise equivalent power* (NEP), which is defined as the minimum optical input required for an SNR equal to 1. The NEP for photon noise is defined as [54]

$$NEP^2_{photon} = \frac{4A\Omega(kT_S)^5}{c^2h^3}\int_0^\infty \left[1+\frac{\eta\varepsilon}{e^x-1}\right]\mathrm{d}x, \qquad [\mathrm{W}^2] \quad (2.27)$$

where $A\Omega$ is the throughput, η is the optical efficiency of the detector, ε is the emissivity of the source, T_S is the temperature of the background radiation source, and $x = h\nu/kT_S$ where ν is the optical frequency.

As mentioned above, photon noise leads to an increase in NEP and a multiplex disadvantage. While it is possible to reduce the throughput or optical efficiency of the system, as shown in Equation 2.27 the only meaningful way to reduce the NEP is to reduce the bandwidth of radiation incident on the the detector, $\mathrm{d}\nu$ (or $\mathrm{d}x$). The solution for this thesis is to reduce the bandwidth incident on a single detector by means of a post-dispersing element, such as is used in the PDPFTS [55] (see Chapter 3).

The second source of optical noise, called source noise, arises from variations in intensity over time, which may be either periodic or random in nature [56, 27]. An FTS is sensitive to time variations in source power which cannot be differentiated from variations

in detected power arising from interference fringes produced by the interferometer. Generally these observed fringes vary as $1/f$ in the frequency domain. Thus source noise is often referred to as $1/f$ *noise* [40]. However, it is entirely possible for variations at higher frequencies.

Consider a *pulsar*, a magnetized, rotating, compact stars with short, precise rotational periods. Stabilities in the period of pulsars have been measured with errors as low as on the order of 10^{-17} s for rotational periods on the order of 10^{-3} s [57]. Thus the regularity of the pulsar emission would manifest as a highly stable monochromatic source.

To date, the best solution for dealing with source noise is the *rapid scan* technique. In the rapid scan technique the OPD is varied fast enough to bring all fringe frequencies above the source noise assuming $1/f$ noise. In rapid scan method the modulation frequencies of the infrared signal are proportional to the velocity of the translation mechanism. It is therefore possible to shift the modulation frequencies above the $1/f$ noise knee. The self modulation of the FTS efficiently suppresses the source noise to low wavenumbers where there is no observable signal [27].

Electrical Noise

Electrical noise sources in an FTS are generally categorized as *Johnson noise*, *phonon noise*, *shot noise*, and *flicker noise* [53]. Johnson noise, also called *thermal noise*, is approximately white, meaning that it has a flat spectral profile [52]. Johnson noise arises from the motion of charge carriers (typically considered to be electrons) in the detection circuitry which depends upon the temperature. The NEP of Johnson noise is defined as [54]

$$NEP^2_{Johnson} = 4kT_bP\left|\frac{Z+R}{Z-R}\right|^2(1+\omega^2\tau^2), \qquad [\mathrm{W}^2/\mathrm{Hz}] \quad (2.28)$$

where T_b is the bolometer temperature, P is the electrical power into the bolometer, R is the resistance, Z is the impedance, and τ is the physical time constant.

Similarly, phonon noise, also known as *thermal fluctuation noise*, arises from the ran-

dom exchange of energy between thermal masses in the form of vibrational energy known as phonons [58]. Phonon noise is typical in detectors, such as bolometers [59]. The NEP of phonon noise is given as

$$NEP^2_{phonon} = 4kGT_b^2 \frac{\int_{T_c}^{T_b} \left[\frac{Tk(T)}{T_b k(T_b)}\right] \mathrm{d}T}{\int_{T_c}^{T_b} \left[\frac{k(T)}{k(T_b)}\right] \mathrm{d}T}, \qquad [\mathrm{W}^2/\mathrm{Hz}] \quad (2.29)$$

where G is the dynamic thermal conductance, $k(T)$ is the thermal conductivity, T is the temperature, and T_c is the heat sink temperature. From Equations 2.28 and 2.29 one may appreciate that where possible every component of the detection circuitry be properly cooled.

Flicker noise is a type of pink noise similar to source noise, meaning that the spectral profile of flicker noise is proportional to $1/f$. Flicker noise arises from time-dependent fluctuations in electrical current, and has been observed in nearly all electronic materials and devices [60]. Such noise is likewise typical of low-frequency drifts in amplifiers and measurement systems [61]. In general, both flicker noise and Johnson noise are difficult to model and are generally measured as *excess noise* [61].

Other sources of noise arise from imperfections in an instrument or non-ideal component behaviour and may be reduced by careful instrument design. For example, consider a translating stage whose position is sampled in the time domain. Should the there be any variations in the velocity, or *velocity jitter*, there will also be jitter in the sampled positions. Ultimately, the effects of velocity jitter become negligible should the FTS employ a high precision translation stage for the moving mirror, such as those provided by Aerotech Inc. [62].

Shot noise arises from the discrete nature of a system, such as electrons in the case of electronic circuits [63]. The shot noise $\varepsilon \propto \sqrt{n}$ arises from the Poisson distribution, which is why shot noise may also be referred to as *Poisson noise*. In general, shot noise in electronics is the least significant source of noise.

Other forms of noise include load noise, amplifier noise and excess noise associated with the bolometer itself, which are not covered in this work. Since, in general, each noise source can be considered as being independent, the total NEP of the system is given as the quadrature sum:

$$NEP^2_{Total} = NEP^2_{photon} + NEP^2_{Johnson} + NEP^2_{phonon} + NEP^2_{load} + NEP^2_{amp} + NEP^2_{excess}. \quad [\mathrm{W}^2/\mathrm{Hz}] \quad (2.30)$$

For a comprehensive study on bolometer noise and bolometer theory, particularly for the bolometer used throughout this work, the reader is directed to Gom [64].

2.4.2 Discrete Sampling

In practice, the continuous sampling of an interferogram is costly and time consuming because of the vast amount of data which must be managed and processed. Consequently, an interferogram is generally sampled discretely. By application of the FFT algorithm described in Section 2.5.2, the interferogram can be converted into a spectrum. The assumption underlying discrete sampling is that the discrete data are an adequate representation of the theoretically smooth, continuous, analytic interferogram [27]. Mathematically, discrete sampling is the equivalent of multiplying the theoretical interferogram by the Dirac comb. One ramification of discrete sampling is measurement of the ZPD is not guaranteed [27]. The result is an asymmetric interferogram, which means the Fourier cosine transform cannot be used. Considerations involved with discrete sampling are discussed below.

2.4.3 Nyquist Sampling Theorem and Aliasing

With the conversion of a continuous signal to discrete sample points, the question arises as to how many samplings are required to faithfully reconstruct the signal from the collected data [65, Chapter 15]. The Nyquist criteria answers this stating that the OPD sampling interval for a spectrometer, Δx, must be less than or equal to the inverse of twice the bandwidth

of the spectrum:

$$\Delta x \leq \frac{1}{2(\sigma_N - \sigma_L)}, \qquad \text{[cm]} \quad (2.31)$$

where σ_N is the maximum wavenumber and σ_L is the minimum wavenumber of the spectrum, the difference between the two being the spectrum bandwidth in cm^{-1} [66]. The maximum wavenumber is also referred to as the Nyquist frequency σ_{Ny} [67].

Failure to meet the Nyquist criteria results in an aliased interferogram. The result is the folding of information beyond the Nyquist frequency onto the observed spectrum, causing an overlap of one portion of the spectrum with another. Aliasing is observed as the folding of information beyond the Nyquist frequency onto a lower frequency [40, 27]. As an example of aliasing, consider a spectrum with a component σ_o of an interferogram sampled at $\sigma_o < \sigma_N$. If there exists information beyond the Nyquist frequency, the features located at $\sigma = 2m\sigma_N \pm \sigma_o$, where m is an integer, are shifted to $\pm\sigma_o$ in the spectrum. Failure to properly account for aliasing can generate erroneous results. It should be noted that any high frequency noise is always folded to appear in the band of interest. Thus low pass filters are an important design consideration for FTS [27].

2.4.4 Instrumental Line Shape

In order to measure every frequency in a spectrum, the maximum OPD of an FTS must extend to infinity. However, the practical limitations of an FTS make such a measurement impossible for a real instrument as there is a finite path difference, which produces the instrumental line shape (ILS) of an FTS [40]. The ILS defines the spectral line for a monochromatic source within the FTS [27]. Since the interferogram is measured out to a finite OPD, a fixed maximum path length is the mathematical equivalent to multiplying the interferogram, $I(x)$, by a boxcar function where L is the maximum OPD. Consequently, the finite nature of a real-world interferogram is identical to the spectrum being convolved with a sinc function (Equation A.35).

2.5 Recovering a Spectrum

The FT is an analytical technique used for continuous systems. As seen in Section 2.4, however, real-world data are discrete and not continuous, finite not infinite, and in general asymmetric not symmetric. This section outlines basic techniques used to recover a spectrum from a non-ideal interferogram.

2.5.1 The Discrete Fourier Transform

The FT was derived assuming continuous functions. However, interferograms are in general sampled discretely and not continuously, meaning the FT cannot be applied to the system. Instead, the spectrum, $B(\sigma_j)$, must be calculated using the Discrete Fourier Transform (DFT) [35]. The DFT is given as:

$$B(\sigma_j) = \sum_{n=0}^{N-1} I(x_n) e^{-i2\pi\sigma_j x_n/N}, \qquad [\mathrm{W/cm^{-1}}] \quad (2.32)$$

where N is the number of elements in the interferogram, $I(x_j)$ is the interferogram at the discrete optical path difference (OPD) labelled as x_j. The discrete OPD corresponds through the transformation with a discrete wavenumber, σ_j.

The DFT is computationally dense, with N samples requiring N^2 computations. The immense computational requirements became the limiting factor for analysing spectra using an FTS until 1965 with the redevelopment of the Fast Fourier Transform (FFT) [68, 41]. The FFT drastically reduced the required number of operations required for the computation of a spectrum to $N \log N$, which ushered in the widespread use of the the FTS in spectral analysis.

2.5.2 The Fast Fourier Transform

Each Fourier integral represents computation of the successive summation over the entire dataset [67]. Even with the emergence of digital computers, the time taken to evaluate the DFT was prohibitive, especially for large data sets, until the discovery of the FFT al-

gorithm [41]. The application of the FFT pushed the viability of the FT in experimental practices.

From the basic formula of the DFT defined above, Equation 2.32 describes the relationship between the interferogram measured at discrete OPD values, x_j. For the discrete transformation, it is common practice for the discrete OPD values to be measured at regular intervals, Δx. The transform of the discrete interferogram introduces a regular spectral interval, or spectral resolution, which arises since each element in $B(\sigma_j)$ is linearly independent of all other elements [27]. The σ_j values are defined by first defining the spectral resolution,

$$\Delta\sigma = \frac{\sigma_N}{N}, \qquad [\text{cm}^{-1}] \quad (2.33)$$

where σ_N is the Nyquist frequency described in Section 2.4.3. This definition of the spectral resolution, coupled with the sampling interval $\Delta x = L/N$ allows the spectral resolution to be defined as

$$\Delta\sigma = \frac{1}{2L}, \qquad [\text{cm}^{-1}] \quad (2.34)$$

where L is the maximum OPD between the two interfering beams.

The instrumental line shape introduces an additional modification to the spectral resolution [40]. Recall from Section 2.4.4 that restricting an FTS to a finite path difference results in the convolution of the spectrum by a sinc function with a FWHM $\sim \frac{1.207}{2L}$ [27]. The result is that the minimum resolvable element is

$$\Delta\sigma = \frac{1.207}{2L}. \qquad [\text{cm}^{-1}] \quad (2.35)$$

This series of calculations was once limited in terms of computational time due to the numerous operations required until the rediscovery of the Cooley-Tukey algorithm, i.e., the FFT. The FFT algorithm exploits factorization to eliminate repetitive operations [68, 41]. The DFT can be accomplished far faster as the algorithm recursively breaks down components into smaller DFTs, the best known of which divides transforms in half at each

step [67]. By this method the algorithm is limited to data sets with 2^N samples. For data sets that fail to meet the 2^N samples criterion, zeroes may be added to the data, a process known as zero filling.

The FFT has so far been able to run as few as $N\log_2(N)$ operations as opposed to N^2 operations for the base DFT, making it far faster for large data sets. The result is that the time requirements to compute a FT are now less of a concern; a complex FT of 10^9, double precision, data points can be computed on a modern laptop in less than two minutes [69]. For full treatment of the FFT, refer to Brigham [67].

The process of zero filling artificially increases the maximum OPD without adding any information and serves as a technique of interpolation. From Section 2.3, an increase in the maximum OPD corresponds to a finer wavenumber grid [40]. The Nyquist frequency remains constant since the sampling interval of the interferogram, Δx, does not change [27]. The overall impact of zero filling is an interpolation of the spectrum for an increase in *plotting resolution*; the FWHM of the spectral lines remain constant.

2.6 Phase Correction

The previous sections describe the operation of an ideal FTS which yields an interferogram that is real and intrinsically symmetric about ZPD. However, in practice there are experimental and instrumental variables that introduce asymmetries into the measured interferogram. These asymmetries are represented in the spectral domain using the complex FT and result in what are called phase errors. Since the spectrum of an asymmetric interferogram is complex, the real component of the spectrum contains only a portion of the measured signal. Ignoring the imaginary component leads to errors in the frequency, amplitude, line shape, and the SNR of spectral features. Since by design the interferogram is intrinsically symmetrical, the measured phase information obtained from a short double sided scan around ZPD can be used to correct for instrumental effects that break the symmetry of an FTS, a process known as phase correction.

This section will explore sources of phase errors and the Forman method of phase correction. The work in this thesis applies the Forman method as it is considered best practice. Since the Forman method involves manipulation of complex arrays and convolution, a sound understanding of Fourier techniques is required.

2.6.1 Theory

As discussed above, an interferometer produces an interferogram which is a real quantity that measures the intensity of the interference pattern as a function of OPD. While ideally the interferogram should be symmetric, there are many factors that can break the symmetry. Asymmetries in the observed interferogram produce phase shifts in the calculated spectrum, producing both a real and imaginary component. The process of phase correction shifts the desired signal from the imaginary domain back into the real domain, leaving on average one half of the noise since it is usually considered random and thus incoherent.

Consider an interferogram, $I(x)$, with some measure of asymmetry. From Table A.2 it can be seen that the FT of an asymmetric function gives both a real and imaginary component:

$$\mathscr{F}[I(x)] = \int_{-\infty}^{\infty} I(x) e^{-i2\pi\sigma x}\,\mathrm{d}x = B(\sigma)e^{i\phi(\sigma)} = B_R(\sigma) + iB_I(\sigma), \qquad [\mathrm{W/cm^{-1}}] \quad (2.36)$$

where B_R and B_I are the real and imaginary components of the spectrum. As can be seen from Equation 2.36, the real and imaginary components are a product of a phase term and the real spectrum:

$$\begin{aligned} B_R(\sigma) &= B(\sigma)\cos(\phi(\sigma)) = \int_{-\infty}^{\infty} I(x)\cos(2\pi\sigma x)\,\mathrm{d}x \\ iB_I(\sigma) &= iB(\sigma)\sin(\phi(\sigma)) = -i\int_{-\infty}^{\infty} I(x)\sin(2\pi\sigma x)\,\mathrm{d}x \end{aligned} \qquad [\mathrm{W/cm^{-1}}] \quad (2.37)$$

In the absence of noise, the absolute value of the complex spectrum is in general equiv-

alent to the real spectrum. That is:

$$B(\sigma) = |B(\sigma)| = [(B_R)^2 + (B_I)^2]^{1/2}. \qquad [\mathrm{W/cm^{-1}}] \quad (2.38)$$

In practice obtaining the spectrum from the absolute value from its real and imaginary components cannot treat noise properly. If noise is included in the spectrum, then taking the absolute value of the spectrum pulls all the noise out of the imaginary domain into the real. The result is the shifting of the noise floor as the noise becomes positive definite and no longer averages to zero. A second consequence is an increase in the spectral noise level by a factor of $\sqrt{2}$ from the noise in the imaginary domain being introduced into the real domain [27]. The increase in the baseline of noise introduces problems when measuring low signal features, such as a fully absorbing line.

Thus phase correction is now widely accepted as a key step in analysing data produced by an FTS.

2.6.2 Sources of Phase Error

Phase errors arise from several sources. They are categorized as systematic and random. Systematic phase contributions may be calibrated and removed in processing. On the other hand, random phase contributions must be analysed on a case-by-case basis [27].

If we define an interferogram in a general form:

$$I(x_n) = \sum_{j=-N}^{N} B(\sigma_j) e^{i2\pi\sigma_j x_n/N}, \qquad [\mathrm{W/m^2}] \quad (2.39)$$

then we may define a phase shift such that the exponential in Equation 2.39 does not go to one when x goes to zero. The interferogram may be redefined to include the phase shift:

$$I(x_n) = \sum_{j=-N}^{N} B(\sigma_j) e^{i(2\pi\sigma_j x_n/N + \phi_j)}. \qquad [\mathrm{W/m^2}] \quad (2.40)$$

In general, the phase shift, ϕ_j, is wavenumber dependent and corresponds to the frequency σ_j. The phase shift can be generally expressed as polynomial dependent on σ.

The components of phase error may be classified as phase offset (ϕ_{DC}), linear phase errors (ϕ_{Lin}), nonlinear phase errors (ϕ_{NL}), and random phase errors (ϕ_R).

Phase Offset - ϕ_{DC}

A typical FTS will utilize both an electronic amplifier and filter in data collection. Electronic amplifiers and filters typically have a well-defined complex frequency response, and are commonly used in tandem. In a well designed spectrometer the examined waveband will generally coincide with the in-band phase and amplitude responses for the amplifier and filter. Matching the curves to the desired band can reduce the phase response in the spectrum to an offset. Ideally, the phase and frequency response is flat. Such is the case for Chebyshev type filters, though such filters introduce a quadratic amplitude response; Butterworth and Bessel type filters behave conversely with a flat amplitude response but a nonlinear phase response [63]. If filter and amplifier response is understood, the phase offset can be minimized or calibrated and removed in post processing.

Another example is the frequency and phase response of the detector, which vary with temperature. Since changes in loading can cause significant shifts in temperature, the response of the detector may vary between sources. While filter and detector responses are not the only possible source of phase offset errors in an interferogram, these represent common sources of phase offset errors since electronic amplifiers and filters are commonly used in spectrometers.

Linear Phase - ϕ_{Lin}

Linear phase errors are introduced by not precisely sampling the interferogram at ZPD [70]. The missampling of ZPD may be represented in Equation 2.39 as $x_n = n\delta x + \alpha$, where

α represents a shift in OPD. The resulting exponent is given as

$$2\pi\sigma_j(n\delta x+\alpha) = 2\pi\sigma_j n\delta x + 2\pi\sigma_j\alpha. \tag{2.41}$$

From Equation 2.41 it is clear that the phase shift is given as $\phi_j = 2\pi\sigma_j\alpha$, meaning the phase shift is proportional to the frequency. Thus an error in the assumed location of ZPD will result in the spectrum having a linear phase error with frequency. This result may be likewise derived for the shift in OPD using the properties of the FT (see Table A.1). Should ϕ_j vary linearly with wavenumber, then the interferogram is symmetric about $x = \alpha$, which is known as the point of stationary phase.

While it is possible to precisely measure ZPD, the practice is often unnecessary. Consequently, there will typically be a linear phase error which must be corrected to produce an accurate spectrum. The shift in ZPD may be determined as:

$$\delta ZPD = \frac{\delta x\phi_{Lin}(\sigma_{Ny})}{\pi}, \qquad \text{[cm]} \tag{2.42}$$

Where δZPD is the shift in ZPD, δx is the sample spacing for the OPD and $\phi_{Lin}(\sigma_{Ny})$ is the phase at the Nyquist frequency. From Equation 2.42 one can see that missing ZPD by a full sample introduces a phase shift of π at the Nyquist. Equation 2.42 may then be used to characterize the spectrometer; a well designed spectrometer generally has δZPD between $-\delta x$ and $+\delta x$, or less than one step in either the positive or negative direction, though this precision is not necessary.

Similar to phase offset, ϕ_{DC}, the system may be calibrated to account for the linear phase error. An example is the calibration required for a translation stage whose OPD is time sampled, but on a different time grid than each of the multiplexed detectors. An example is the differing time grid used for the *Herschel* SPIRE FTS [71], which sampled the detector at four times the rate of the translating stage using a single atomic clock. The correction for linear phase shifts is typically straightforward and effective.

Nonlinear Phase - ϕ_{NL}

There are several potential sources of nonlinear phase errors in FTS spectra. Of these, the most prevalent is unbalanced dispersion between the arms of the interferometer [27]. Working from Equation 2.39, unbalanced dispersion will cause a phase shift proportional to the thickness and refractive index of the dispersive element. In other words, Equation 2.41 may be rewritten as:

$$2\pi\sigma_j(x_n + \mu_j d) = 2\pi\sigma_j x_n + 2\pi\sigma_j \mu_j d, \tag{2.43}$$

where μ_j is the index of refraction of the unbalanced material at the frequency σ_j, and d is the thickness. If μ_j were to be constant across all measured frequencies then the phase shift would be linear rather than nonlinear. However, as shown in Equation 2.44, in a standard dispersive medium higher frequencies often appear to trail lower frequencies as the first order approximation of the index of refraction is proportional to the inverse square of the wavelength, resulting in a chirped interferogram [40]. The effects of unbalanced dispersion, and therefore ϕ_{NL}, may be reduced by use of a compensator plate for a well designed interferometer. The trade-off of compensation is reduced optical efficiency [40].

$$n(\lambda) = A + \frac{B}{\lambda^2} + \frac{C}{\lambda^4} + \cdots = A + B\sigma^2 + C\sigma^4 + \cdots \tag{2.44}$$

Cauchy's equation (Equation 2.44) is an empirical formula defining the wavelength dependence of the index of refraction. The coefficients A, B, C and so on are determined by fitting Cauchy's equation to measured indices of refraction. Usually two terms are a sufficient approximation [48].

Random Phase - ϕ_R

There are two components measured in a single interferogram: the signal (I) and the OPD (x). The signal can be affected by optical and electrical noise inherent in the spectrometer; noise can be reduced but never eliminated [27]. Similarly, the OPD measurements can have errors introduced by vibrations in the system, as well as the same electrical noise

impacting the signal. These sources of noise are carried through processing into the spectrum and, consequently, into the phase. Generally, uncertainty in the phase decreases with increasing SNR in a spectrum [40].

The random noise introduced by the spectrometer should equally affect both the real and imaginary components of the spectrum. As mentioned above, the phase uncertainty is reduced by increasing the SNR. For broadband measurements, the greatest SNR is achieved around ZPD [40], where there is also ample phase information. When the band is narrowed, such as is the case of the PDPFTS, there are techniques which may be used to extract the sparse phase information. Since noise is random there is no phase relationship, half the phase noise will remain in the imaginary domain with the rotation of the signal back into the real domain.

2.6.3 Methods of Phase Correction

The goal of phase correction is to restore the desired spectral information from the imaginary domain to the real domain. The shifting of the information from the imaginary domain to the real domain is essentially a rotation which is performed by multiplying the spectrum by the reciprocal of the phase function ($e^{-i\phi}$):

$$B(\sigma) = [B(\sigma)e^{i\phi}]e^{-i\phi}. \qquad [\mathrm{W/cm^{-1}}] \quad (2.45)$$

From the convolution theorem, multiplication in the spectral domain corresponds to a convolution in the spatial domain. Therefore, two main methods exist to correct phase: a multiplicative (Mertz) method [72], historically used when there was little computing power, and a convolution (Forman) method [73] that is considered the best practice for phase correction.

These methods are based around the assumptions that phase is smooth and slowly varying and the interferogram is double-sided. These assumptions allow the use of phase determined from only a low resolution interferogram. The implication is that only a small

portion of the interferogram need extend beyond ZPD rather than a large double-sided interferogram. As will be discussed below, the length of the double-sided portion is significant in determining the phase for a narrow band, such as that observed by the PDPFTS. Since the small double-sided interferogram includes the centerburst, it also should have a good SNR. A signal with a greater SNR allows for the low resolution phase information to be determined and applied to correct the high-resolution, one-sided spectrum.

The Forman Method

Also known as the convolution method, the Forman method of phase correction is based around the convolution theorem [73]. Using the low-resolution spectral information, the interferogram is convolved with a function known as the phase correction function (PCF). The PCF is calculated from the phase information as

$$PCF(x) = \mathscr{F}^{-1}[e^{-i\phi(\sigma)}] = \int_{-\infty}^{\infty} e^{-i\phi(\sigma)} e^{2\pi\sigma x}\, \mathrm{d}\sigma. \tag{2.46}$$

The PCF is convolved with the interferogram to symmetrize the double-sided portion of the interferogram:

$$I_{symm}(x) = I_{asymm}(x) * PCF(x). \qquad [\mathrm{W/m^2}] \tag{2.47}$$

Although the phase information is identical to that used in the Mertz method, the calculation and convolution of the PCF distinguishes the use of each method. As presented by Forman, this method allows for the inclusion of mathematical bandpass filtering with no added processing costs and may be reapplied to better improve the phase correction should the first attempt prove insufficient. Forman also introduced the idea of apodizing the PCF to minimize spectral artefacts caused by discontinuities at the boundaries being convolved with the interferogram.

It has been found that the Forman method performs better than the Mertz method for

both linear and quadratic phase correction. Thus the Forman method is used throughout the remainder of this work. For completeness, readers wishing to compare the two methods are directed to the works of Mertz [72] and Forman [73].

Other Methods

The concept of phase correction is found in other branches of science. As mentioned, the process of phase correction is complex and different approaches outside the Mertz and Forman methods have been adopted in different disciplines, though these are more limited in application [63, 74, 75, 76]. These are predominantly based around different means of phase error identification. The Forman method is widely accepted as the Best practice in the field of FTS is to use the Forman method [27].

2.6.4 Applying the Forman Method

This section discusses considerations that must be made in applying the Forman method. These considerations range from the design of the spectrometer up to the application of the phase fit. An example of a phase correction outlining the steps below is given in Figure 2.5.

The double-sided interferogram

The range of double-sidedness is an important consideration in the design of a spectrometer. Consider a primarily single-sided interferogram: the entire scanning mechanism contributes to enhancing the resolution of the instrument at the cost of using suboptimal phase correction. Conversely, a fully double-sided interferogram with the same scanning range has half the resolution of the one-sided interferogram but contains all the relevant phase information.

For a well designed spectrometer the phase should be smooth and slowly varying. The implication is that the relevant phase information may be obtained from a relatively low-resolution spectrum. Considerations must be made to include an appropriate resolution to determine the phase for a given narrow band; in the case of the PDPFTS, the bandwidth,

$\delta\sigma/\sigma$, is typically less than 1%, and requires a higher resolution to determine the phase. The balance between high resolution and phase information is found with the single-sided interferogram. The small double-sided portion provides adequate information about the phase, while the extended one-sided portion gives greater spectral resolution.

The necessary double-sidedness is dependent upon the spectrum under investigation. At least two phase measurements are required in-band for a linear phase correction: three are required for a quadratic phase correction. The required double-sidedness may be determined by the fraction of the Nyquist frequency in the band:

$$\gamma\sigma_{Ny} = n\delta\sigma, \qquad [\mathrm{cm}^{-1}] \quad (2.48)$$

where γ is the percentage of the Nyquist frequency in the band, $\delta\sigma$ is the spectral resolution, and n represents the number of points required for phase correction. For linear phase correction n should be a minimum of 2. Using the fact that $\sigma_{Ny} = \frac{1}{2\Delta x}$ and $\delta\sigma = \frac{1}{2L_{max}}$, and that $L_{Max} = N\Delta x/2$ for discrete measurements, Equation 2.48 may then be rearranged:

$$N = \frac{2n}{\gamma}. \quad (2.49)$$

The design of a spectrometer gives a specified range of motion for the system, L_{TOT}. The maximum range of an FTS may be defined as the sum of the length of both the double-sided portion (L_{DS}) and the single-sided portion (L_{SS}): $L_{TOT} = L_{DS} + L_{SS}$. It is therefore possible to adjust L_{DS} and L_{SS} while constraining L_{TOT} for a given spectrometer. The amount of double-sidedness is defined as the ratio of the two parts of the interferogram: $L_{DS}/L_{SS} \leq 1$. When the ratio is equal to one, the interferogram is fully double-sided, and when the ratio is equal to 0 the interferogram is one-sided. The double-sidedness relation describes the trade-off between phase information and spectral resolution.

As an example, assume a band that is 1% of the Nyquist frequency is being corrected, such as that for the PDPFTS. The minimum number of points required to correct linear

and quadratic phase errors is 400 and 600 points respectively. This relates to the minimum required double-sidedness by the measurement spacing between points, Δx, and ultimately determines the minimum required double-sidedness ratio of a given spectrometer. As will be shown, there are techniques to recover phase information when accessing multiple bands used in the PDPFTS.

The phase correction function

The phase correction function (PCF) is defined as the iFT of the inverse of the phase (See Equation 2.46). From Equation 2.47 it is clear that the application of the PCF requires a convolution. However, since both the interferogram and PCF are finite, the length of the PCF becomes an important consideration. These considerations will be discussed in depth in section 2.6.4. Suffice it to say that there is a trade-off between the length of the PCF and the final resolution of the spectrum due to the convolution process. Thus, it is prudent to ensure the PCF is not longer than necessary.

Convolution of the PCF with the interferogram serves to redistribute the energy to symmetrize the interferogram [27]. The range across which the distribution takes place is dependent upon the length of the PCF kernel. If the length of the PCF kernel is too small, the redistribution will be insufficient.

The result of the convolution is a one-sided interferogram with the energy redistributed to provide symmetry should the interferogram be mirrored across ZPD. Thus, if more length is given to L_{DS}, the resolution of the corrected spectrum is reduced. Should a fully double-sided interferogram be used, the resolution is reduced by at most a factor of two (See Section 2.6.4).

Phase

As has been discussed, phase is determined from the double-sided portion of the interferogram. However, due to noise it is standard practice to compute a fit for the phase. There are many types of fits that may be used, and many aspects, such as the degree of the

phase fit, are variable. Fitting the phase reduces noise contributions to phase corrections, especially when the fit is based about regions of high SNR within the band [40].

When applying a fit to the phase, there are several practices and techniques that contribute to PCF. In practice, it is possible to fit only a small portion of the phase to a polynomial and extend that fit across the entire range of phase. It is important to realize that the real component phase must be an even function, while the imaginary component must be odd.

When preparing a fit to generate the PCF, certain considerations must be made to ensure that the inverse of the phase fit meets the Dirichlet conditions (Section A.1). Thus sharp transitions and discontinuities should be avoided where possible in the phase fit. Consider the phase measured at 0 cm^{-1}. In order to accurately measure the spectrum at 0 cm^{-1}, the spectrometer must have infinite length. Since an infinitely long spectrometer is impossible, the phase measured at 0 cm^{-1} has no physical meaning and may be set to a value of 0. Likewise, the PCF requires that the input have proper periodicity without edge discontinuities where possible. For more information on the PCF, see Appendix B.

Resolution Loss

For a real spectrometer there are many means by which resolution may be lost. From Section 2.5.2 it was shown that for a finite scan length the minimum resolvable element due to the instrumental line shape becomes $\Delta\sigma = \frac{1.207}{2L_{MAX}}$. There are further considerations based in the phase correction of the interferogram. Consider a single-sided interferogram with a small double-sided portion of length L_{DS} and a longer one-sided portion of length L_{SS}. Assuming the total scanning length ($L_{TOT} = L_{DS} + L_{SS}$) is constrained, then L_{DS} must be sufficiently long to produce an adequate PCF. Consequently, increasing L_{DS} to accommodate a better phase fit and PCF requires a decrease in L_{SS}. Since $L_{MAX} = L_{SS}$ in the case of a single-sided interferogram, a decrease in L_{SS} results in a decrease in the minimum resolvable element and therefore the resolution. Thus there must be a balance between the

double-sidedness of the spectrometer and the resolution for a well designed application.

The use of the convolution introduces a more subtle reduction in resolution. When the PCF is convolved with the interferogram edge distortions are introduced. These distortions only impact the edges by an amount roughly equal to half the length of the PCF on each side of the interferogram. To remove the edge effects the interferogram must be truncated to exclude the data up to where the distortion begins. The result is a one-sided interferogram that has been phase corrected. The corrected spectrum will have a final truncated resolution given as

$$\Delta\sigma = \frac{1.207}{2(L_{SS} - L_{PCF}/2)}. \qquad [\text{cm}^{-1}] \quad (2.50)$$

The spectral resolution is reduced by an amount proportional to half the length of the PCF. Thus both the double-sidedness and the length of the PCF reduce the resolution of the system. The optimum configuration for a spectrometer would therefore match the double-sidedness with the required length of PCF to reduce the impact upon the resolution of the instrument.

2.7 Conclusions

Chapter 2 discussed the foundations of Fourier Transform Spectroscopy with a focus on derivations and techniques for optimization. Section 2.2 introduced Fourier theorems used throughout this work. The ideal Michelson interferometer was introduced in Section 2.3. In Sections 2.4 and 2.5 the principles of sampling real-world interferograms and recovering the corresponding spectra were explored.

Emphasis was given to the technique of phase correction. Section 2.6.1 introduced the theory behind phase correction. Common sources of phase error were explored (see Section 2.6.2) along with the Forman method of phase correction (see Section 2.6.3). Considerations in applying the Forman method were explored (see Section 2.6.4).

Phase errors may be categorized as linear, nonlinear, and random. Systematic phase errors should be minimized and may be calibrated to simplify post-processing. The most

common source of phase error, linear phase error, is easily corrected. The Forman method was explored as the most effective method of phase correction. The techniques associated with the Forman method help outline considerations for an optimum system.

With a background in Fourier Transform Spectroscopy, Chapter 3 explores the theory and design of a PDPFTS.

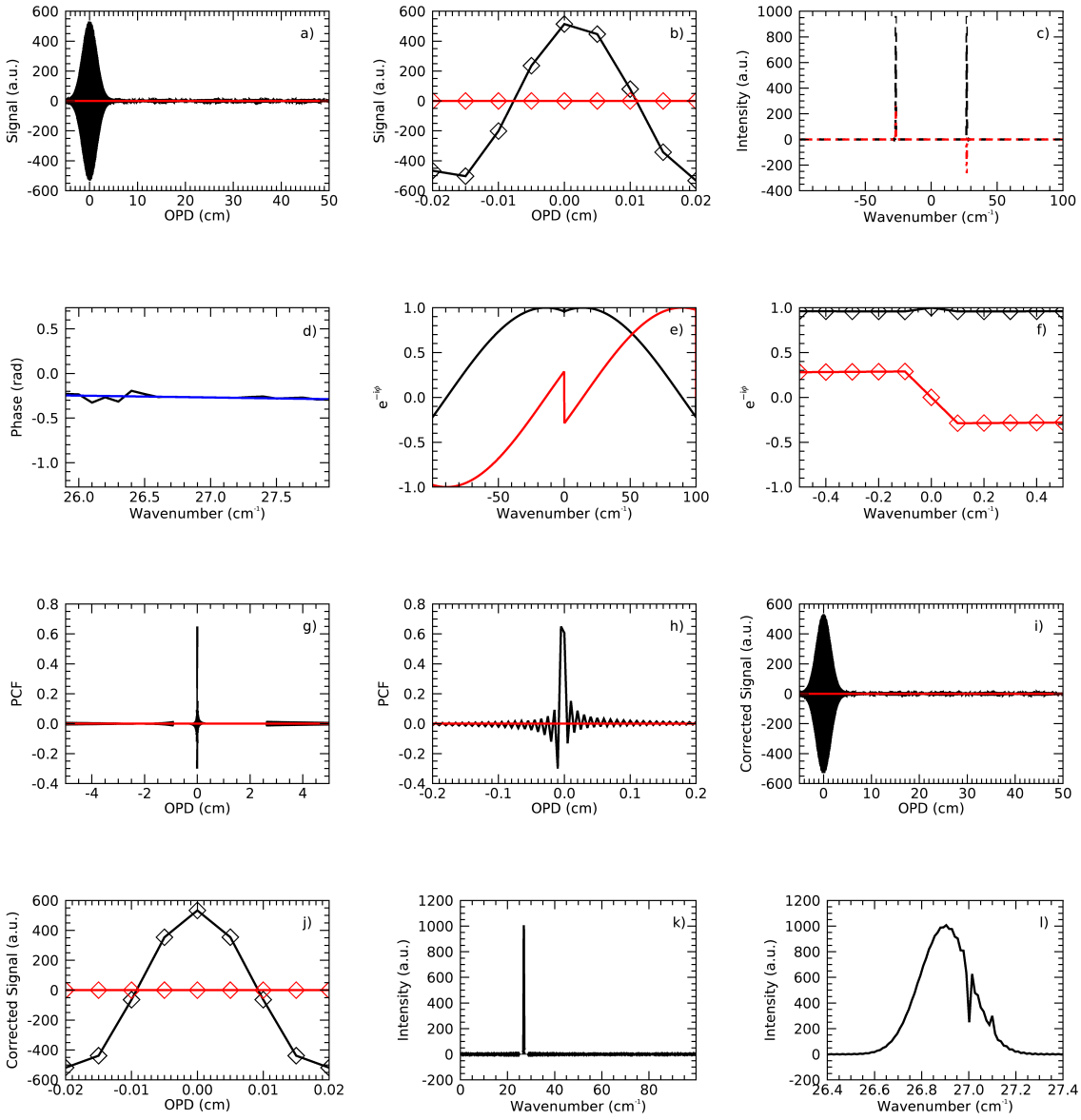

Figure 2.5: Phase correction of an interferogram from the simulation of a PDPFTS. Black denotes the real domain and red denotes the imaginary domain. Panels a) and b) show a single-sided interferogram that is asymmetric about ZPD. Panel c) shows the real and imaginary components for the computed spectrum. Panel d) shows the phase calculated from panel c) in black with a fit for phase over the narrow band of the PDPFTS shown in blue. Panels e) and f) show the reciprocal of the phase term. Panels g) and h) show the real and imaginary components of the PCF. Panels i) and j) show the corrected interferogram which is symmetric about ZPD. Panel k) shows the spectrum computed from the corrected interferogram. Panel l) is the final spectrum showing a continuum and an unresolved emission and absorption line.

Chapter 3

The Post-Dispersed Polarising FTS

> A scientist is happy, not in resting on his attainments but in the steady acquisition of fresh knowledge.
>
> MAX PLANCK

This chapter introduces the post-dispersed polarising Fourier transform spectrometer (PDPFTS) by virtue of its fundamental building blocks. Specifications of the instrumentation used in the design of the PDPFTS will be outlined. Emphasis will be given to the polarisation sensitivity of the PDPFTS, beginning with the polarizing Fourier transform spectrometer (FTS). The PDPFTS will be detailed as the integration of four modules: a source, polarising FTS, grating spectrometer, and detector system (see Figure 3.1). Finally, the test equipment used to characterize the PDPFTS will be explored. As will be shown below, the instrumental test equipment proved to rival the PDPFTS in complexity.

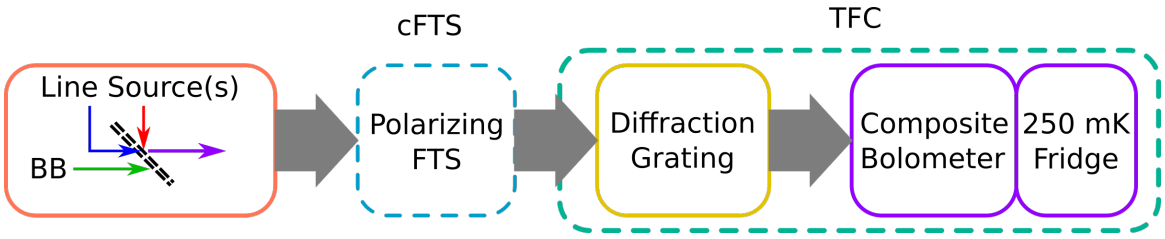

Figure 3.1: Overview of the PDPFTS configuration. The source module and polarising FTS operate at room temperature, while the diffraction grating and detector operate at cryogenic temperatures of 4 K and 250 mK respectively. The dashed lines indicate the system operates under vacuum.

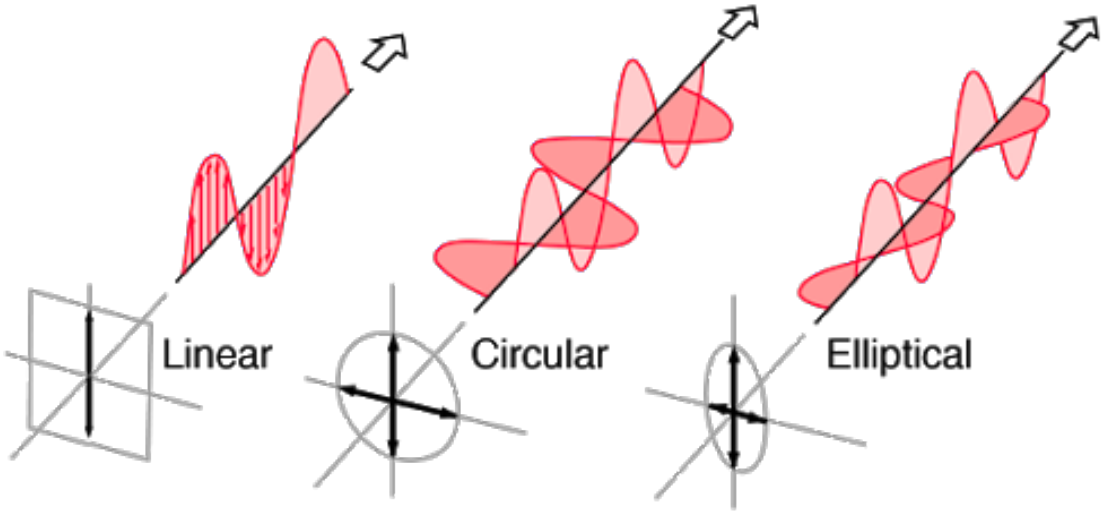

Figure 3.2: Classifications of polarised light: linear, circular, and elliptical [78].

3.1 A Polarising FTS

The polarising FTS used throughout this work is the calibration FTS (cFTS) provided by Blue Sky Spectroscopy Inc. [29]. The cFTS is designed as a THz broad-band, high throughput calibration facility for characterizing THz components, detectors, sources, and other devices. The cFTS is based on Martin-Puplett polarising FTS optics contained within a large aluminum housing to allow the calibration facility to hold a vacuum. A polarising FTS holds several distinct advantages over the FTS designed by Michelson that will be discussed in the following sections [77].

3.1.1 Polarisation

It is well established that light propagates as a transverse electromagnetic wave which requires no medium through which to propagate. The electric field is orthogonal to the direction of propagation and is contained within the *plane-of-vibration*, which is a fixed plane defined by the electric field vector and the propagation vector [48]. The *polarisation state* of lightwaves is defined by the plane-of-vibration. The plane may be fixed at a given angle, such as the case for *linearly polarised* or *plane-polarised* light, or it may rotate due to phase differences between constituent waves, as seen in *elliptically polarised* light. In

the special case that the constituent waves have equal amplitudes and the relative phase difference is equal to $-\pi/2 + 2m\pi$, where m is an integer, then *circularly polarised* light is produced. These polarisations are depicted in Figure 3.2.

The circular and elliptical polarisations are further defined by the rotation of the polarisation while propagating. In either form of polarisation, the direction of the electric field varies with time, resulting in rotation of the plane of polarisation. This can be shown by decomposing the electric field into (x) and (y) components, both orthogonal to the direction of propagation. Convention for the direction of the rotation is defined as seen by an observer looking back at the source; right-circularly polarised light rotates clockwise in this regard, and left-circularly polarised light rotates counterclockwise. By this convention, in right-circularly polarised light the y-component leads the x-component by phase $0 < \phi < \pi$, while left-circularly polarised light is produce by the phase $\pi < \phi < 2\pi$ [48].

As will be shown below, the Martin-Puplett interferometer exploits polarisation to modulate incident light. This is performed through the use of *polarising beamsplitters* to exploit the linear polarisation rather than the more common thin film dielectric beamsplitters used in Michelson interferometers [79].

Linear Polarisation

As described above, linear polarisation means that the electric field vibrates in a single plane. Consider a lightwave composed of two linearly polarised electric fields of identical frequency:

$$\begin{aligned} \mathbf{E_x}(z,t) &= \hat{\mathbf{x}} E_{0x} \cos(2\pi[\sigma z - \nu t]) \\ \mathbf{E_y}(z,t) &= \hat{\mathbf{y}} E_{0y} \cos(2\pi[\sigma z - \nu t + \phi]) \end{aligned} \qquad [\mathrm{V/m}] \quad (3.1)$$

where E_0 is the amplitude for each component, ν is the frequency of the lightwave, and ϕ is the relative phase between the two components. The terms in bold represent vectors, with

$\hat{x}$, $\hat{y}$, and $\hat{z}$ as unit vectors. The total electric field is then defined as the sum of the two:

$$\mathbf{E}(z,t) = \mathbf{E_x}(z,t) + \mathbf{E_y}(z,t). \tag{3.2}$$

Linearly polarised light is obtained when the constituent lightwaves have a relative phase given by a multiple of π. For lightwaves in phase, this condition means that $\phi = 2m\pi$, where m is an integer. Thus Equation 3.2 becomes

$$\mathbf{E}(z,t) = (\hat{\mathbf{x}}E_{0x} + \hat{\mathbf{y}}E_{0y})\cos(2\pi[\sigma z - \nu t]). \tag{3.3}$$

If the two are out of phase ($\phi = m\pi$), the result is

$$\mathbf{E}(z,t) = (\hat{\mathbf{x}}E_{0x} - \hat{\mathbf{y}}E_{0y})\cos(2\pi[\sigma z - \nu t]). \tag{3.4}$$

In either case it can be seen that the resultant field has an amplitude of either $\hat{\mathbf{x}}E_{0x} + \hat{\mathbf{y}}E_{0y}$ or $\hat{\mathbf{x}}E_{0x} - \hat{\mathbf{y}}E_{0y}$. This fact highlights a key feature of linearly polarised light: a plane-polarised wave may be defined in terms of two orthogonal components. Similarly, the angle of the plane-of-vibration is determined from the amplitudes of these orthogonal components:

$$\theta = \tan^{-1}\left(\frac{E_{0y}}{E_{0x}}\right). \tag{3.5}$$

Polarisers

A polariser is an optical device designed to filter a single polarization out of a source, be it *natural* (unpolarised) or polarised light. Filtering is achieved by restricting electric field oscillation to generate or manipulate polarised light. From Section 3.1.1 recall that any polarised wave can be decomposed into orthogonal components, a fact that can be proven using polarisers. The light which is not transmitted may be either absorbed or reflected by the polariser.

Consider a lightwave with a polarization of θ_0 and amplitude E_0. Upon passing through

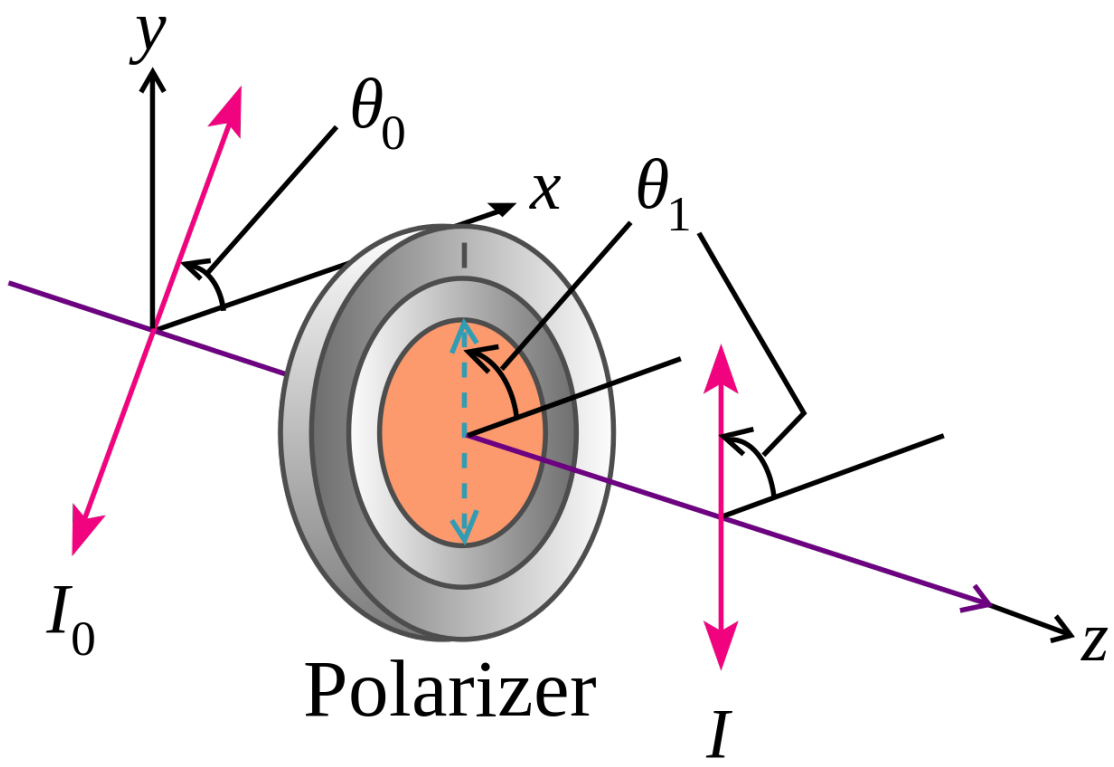

Figure 3.3: Transmission of polarised light through a polariser tilted with respect to the polarisation of the incident light [80].

a polariser, as shown in Figure 3.3, a portion of the electric field is transmitted, specifically the component $E_0\cos(\theta)$, where $\theta = \theta_1 - \theta_0$ is the *relative angle*. Since the radiant flux, or *irradiance*, of the system is proportional to the square of the amplitude of the electric field [48], the irradiance after passing through the polariser is given as

$$\begin{aligned} I(\theta) &= \frac{c\varepsilon_0}{2} E_0^2 \cos^2\theta \\ &= I_0 \cos^2\theta. \end{aligned} \qquad [\mathrm{W/m^2}] \quad (3.6)$$

From Equation 3.6, the maximum irradiance occurs when the relative angle is zero, and complete nulling occurs when the relative angle is $\pi/2$, or the two polarizations are orthogonal. Equation 3.6 is known as Malus' Law [48]. As a special example, consider natural light. One can assume that natural light is unpolarised, meaning the phase is random and may therefore be decomposed equally into orthogonal components. One then finds that

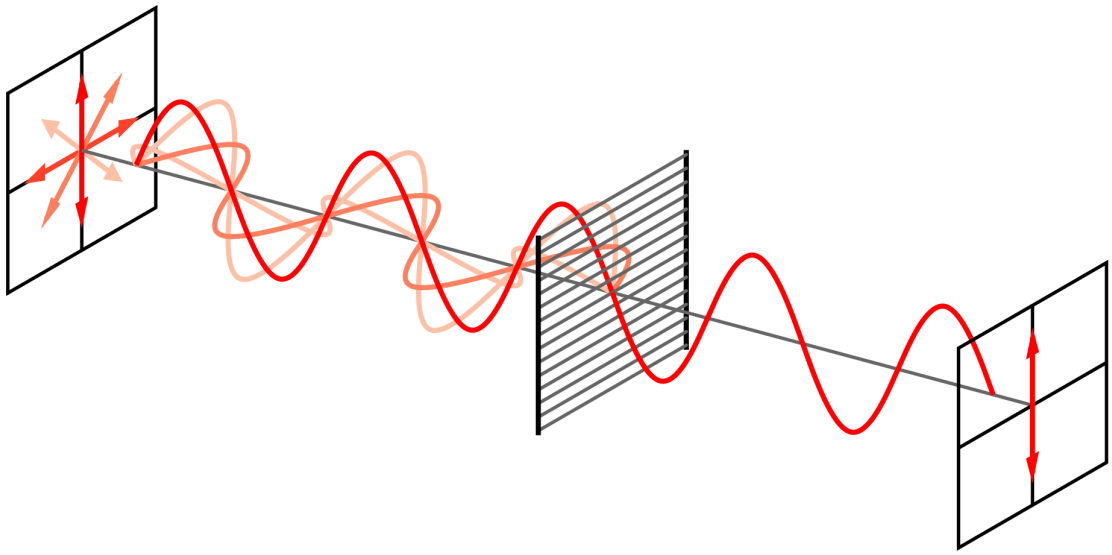

Figure 3.4: Transmission of natural light through a wire grid polariser. The polarisation of the transmitted wave is perpendicular to the wire grid array of the polariser [80].

the radiant flux upon passing through a polariser is half the initial irradiance of the natural light.

There are many types of polarisers based on different mechanisms. Throughout this thesis wire grid polarisers were used to generate linear polarisation. Wire grid polarisers are the simplest form of dichroic polarisers, or polarisers that are transparent to one polarisation but not the orthogonal polarisation [48]. As shown in Figure 3.4, a wire grid polariser is made of an array of thin parallel conducting wire. Incident radiation polarised parallel to the wire grid is reflected, while the wire grid is transparent to radiation polarised orthogonal to the wires. For this process to work, the grid spacing must be less than the wavelength of the incident radiation; more specifically, given a polariser of grid spacing d, the incident radiation must have a wavelength greater than $4d$ [77].

The portion of the electric field which is polarised parallel to the wires of the grid interacts with electrons in the thin wires of the grid, driving conduction electrons to oscillate. This oscillation results in collisions with atoms in the lattice, which passes energy to the atoms. The lightwave is re-radiated out of the polariser, resulting in reflection, and small

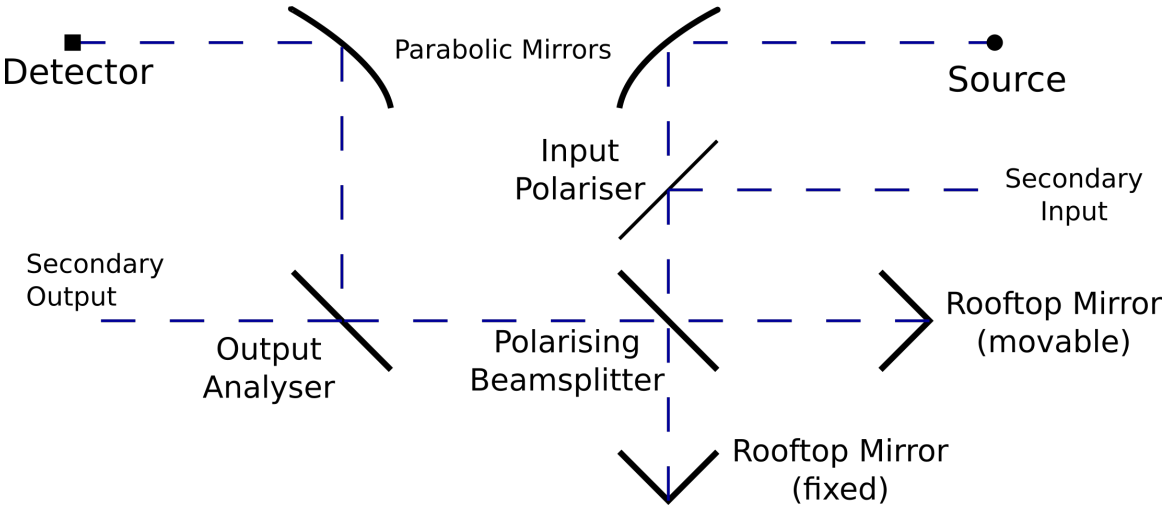

Figure 3.5: Schematic of a Martin-Puplett interferometer. The polarising beamsplitter and output analyser are configured to be oriented 45° and 90° to the grid of the input polariser respectively. Due to the configuration of polarisers the two input and output ports are spatially separated.

remainder of the energy is dissipated into the wires through joule heating [48]. The absorption in a wire grid polariser can be reduced by fabricating the wires using materials with more free electrons, such as copper, to reduce the number of collisions in the lattice. On the other hand, the perpendicular component may only interact along the diameter of the wires in the grid. As these wires are relatively thin, the electric field is unable to cause conduction electrons to flow, allowing for the radiation to be transmitted by the grid.

3.1.2 Martin-Puplett Interferometer

The Martin-Puplett interferometer (MPI) is a modified form of Michelson's interferometer which allows for interferometric spectroscopy using polarising beamsplitters rather than thin film beamsplitters [79]. Similarly, these instruments differ in the use of rooftop mirrors rather than flat mirrors, which are necessary to exploit the polarisation of incident light. As shown in Figure 3.5, incorporating polarisers into the design makes the MPI more complex, but also introduces distinct advantages over other interferometers.

The first advantage is due to the modulation efficiency of the grid beamsplitters being both high and uniform across a wide spectral range [79]. As mentioned above, the spec-

tral range of a polariser extends from 0 to $\sim \frac{1}{4d}$ cm^{-1}, with reflection and transmission coefficients close to 100% [77]. With such a wide spectral range available, a spectral bandpass may be selected using appropriate filters that may be easily reconfigured for a given detector.

Unlike in a Michelson interferometer, in which the output and input ports overlap, a MPI spatially separates these two ports, a feature which is shared in common with the Mach-Zehnder configuration of an FTS [81, 82]. The spatial separation of the input and output ports greatly simplifies calibration. As with every interferometer, the output measures the difference between the input ports, but since the input ports in the MPI are separated, one input may be used with a dedicated calibration source similar to the spectrometer calibrator (SCAL) used in the Herschel-SPIRE instrument [83]. The differential nature of the MPI results in common mode rejection in signals, as the residual output eliminates the signal common to the two inputs. Based on the configuration of the inputs, the result is the rejection of common-mode signals from the instrument itself, the atmosphere, and the field of view [84]. This simplifies the calibration process and may be used to eliminate components of a signal, such as noise due to background emission. Similarly, techniques that use detectors at both outputs can essentially double the modulated component of the interferogram while eliminating the unmodulated component since the two beams are complimentary [77]. Consequently, the MPI is insensitive to seeing its own environment, though it is not immune to effects such as beamsplitter emission.

As shown in Figure 3.5, the fundamental components of the MPI are three polarisers and rooftop mirrors to replace the plane mirrors in the Michelson interferometer. Each of the input polariser, polarising beamsplitter, and output analyser are wire grid polarisers. The polariser selects the input polarisation of the source, be it unpolarized or polarized (see the description of the source module below). For an unpolarized source, this means half the power is rejected, as detailed in Section 3.1.1.

Once the input polarization has been selected, radiation then passes to the polarising

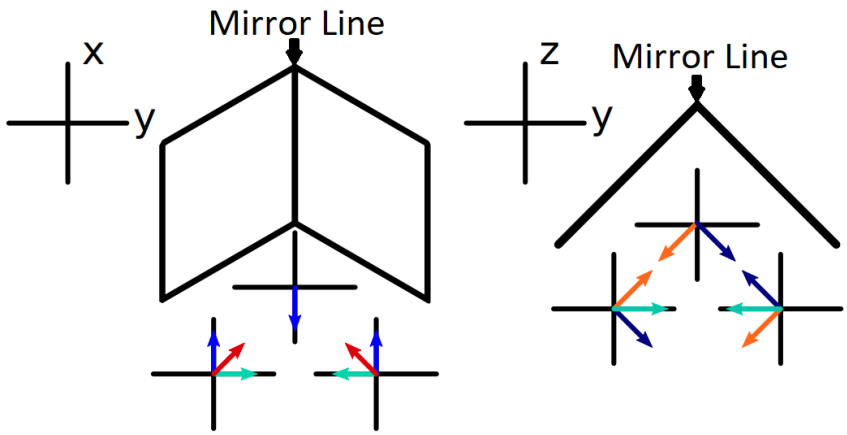

Figure 3.6: The effect of a rooftop mirror on an arbitrary polarization (red). The component parallel to the mirror line (blue) is unaffected, while the perpendicular component (teal) undergoes a rotation of π [85].

beamsplitter, which is oriented such that the projected angle of the transmission axis is at an angle 45° relative to the polarisation axis of the input polariser. From Malus' law (Equation 3.6), this orientation of the polarising beamsplitter transmits half the incident light; by using wire grid polarisers, the remaining radiation is reflected since losses due to absorption are typically less than 1%. Using a wire grid polariser ensures the system is efficient due to the excellent transmission and reflection characteristics of such polarisers across the THz band [77]. Each beam then passes to a rooftop mirror.

The inclusion of rooftop mirrors in place of plane mirrors is vital for the operation of the MPI due to the phase shift introduced by rooftop mirrors. As shown in Figure 3.6, polarised light incident to a rooftop mirror (red) may be decomposed into polarization parallel (blue) and perpendicular (teal) to the *mirror line*, or the line where the two mirrors comprising the rooftop mirror converge. The parallel component reflects twice, with each reflection introducing a phase shift of approximately π. Thus, the polarisation of the parallel component remains unchanged by the rooftop mirror.

The perpendicular component also experiences two reflections, but is a bit more complex and requires the polarisation to be further decomposed to components normal (navy) and parallel (orange) to the mirror. As with the previous case, the component parallel to the

surface of the mirror is reversed while the normal component is unchanged. However, at the second mirror the normal and parallel components are interchanged, and the new parallel component is reversed. The result is a reversal of the perpendicular component of the initial polarisation (teal).

The overall impact of a rooftop mirror on polarised light can be summarised as follows: for incident light polarised at an angle θ relative to the mirror line, the polarisation vector will rotate a factor of 2θ about the mirror line. By carefully aligning the polarising beamsplitter to pass light (either by transmission or reflection) to the rooftop mirrors with a polarisation angle of 45° relative to the mirror line, upon reflection each beam polarisation will be rotated by 90°. Thus, upon passing back to the polarising beamsplitter, the beam which was previously transmitted through the polarising beamsplitter will be reflected, and vice versa. The recombined orthogonal beams then pass to the analyser, which then maps the two signals to the same polarisation angle, producing interference. The output analyser then passes half the signal to either port.

3.1.3 Technical Specifications of the cFTS

The cFTS, developed by Blue Sky Spectroscopy [29], is a calibration facility incorporating MPI optics designed to maximize the available spectral band and overall throughput of the system in the THz regime (Figure 3.7). Since the cFTS was designed to operate in the THz, the calibration facility was designed to be evacuated to prevent atmospheric absorption features within the instrument. The sensitivity and accuracy of the cFTS allows for the precise characterization and calibration of THz components. The technical specifications of the cFTS are given in Table 3.1.

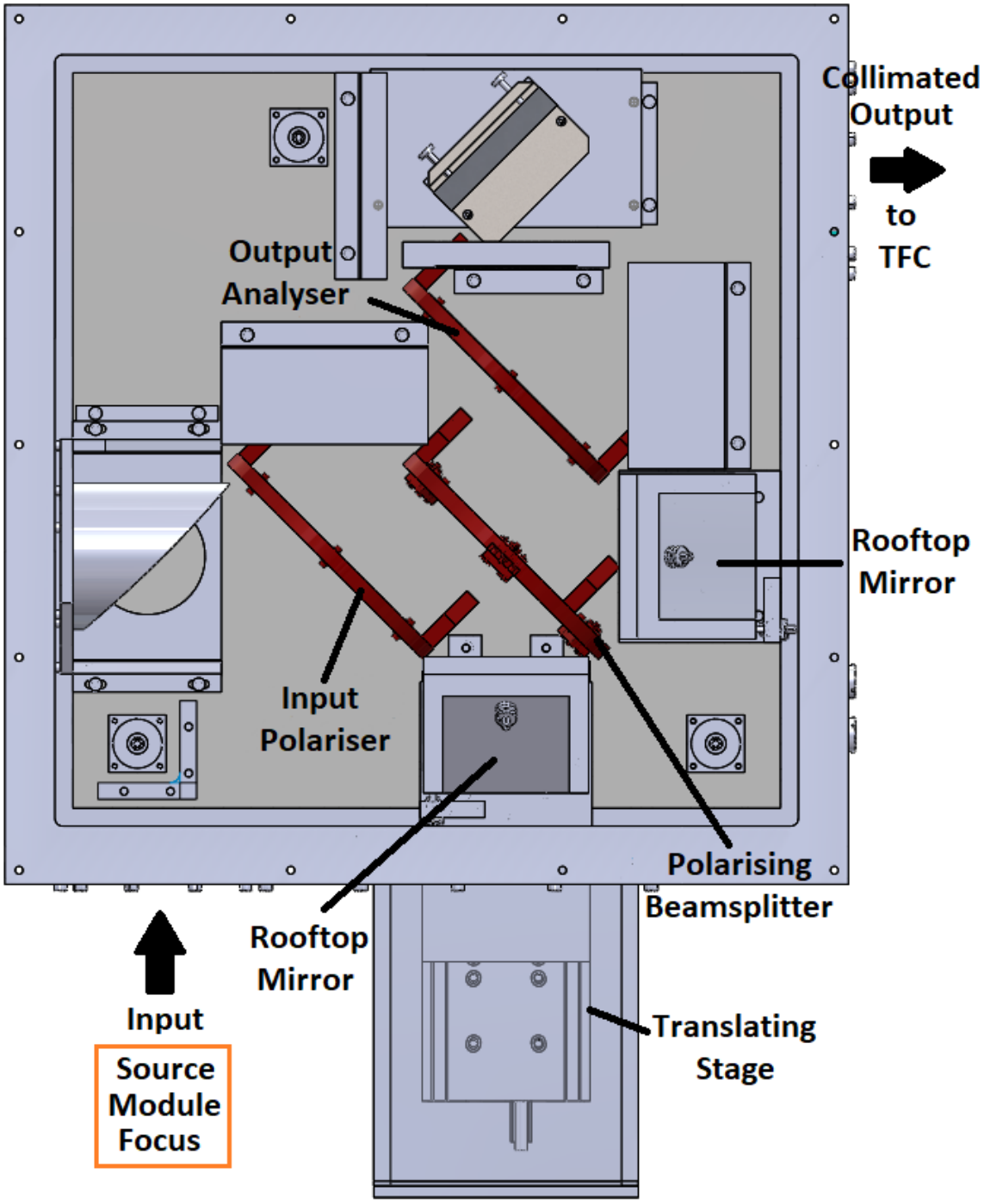

Figure 3.7: Top down view of the cFTS. The focus of the input (bottom left) is ∼75 mm from the the outer wall of the vacuum chamber. The cFTS was modified such that the output (top right) feeds a collimated beam to the input of the Test Facility Cryostat.

Table 3.1: Technical specifications of the cFTS.

Parameter	Value
Spectral Coverage	10 - 333 cm^{-1} (0.3 - 10 THz)
Spectral Resolution	0.01 cm^{-1} (300 MHz)
Resolving Power	1000 - 333000
Spectrometer Throughput	0.14 cm^2Sr
Translation Stage	Precision magnetic linear drive
Metrology	Linear encoder
Grid Polariser Beam Splitter	2 μm metal grid on polypropylene substrate
Body	Aluminum housing; vacuum $<$10 mTorr

While the cFTS doesn't operate at cryogenic temperatures, it does operate under vacuum and provides a flexible interface with the cryostat housing and the grating module, allowing for the exploration of the PDPFTS. Ultimately, the PDPFTS prototype must be completely cryogenic. Future work will utilize a fully cryogenic polarising FTS currently being developed by an industrial partner, ABB [86].

3.2 A Cryogenic Grating Spectrometer

The cryogenic grating spectrometer used in this thesis was originally developed by Veenendaal [87], and later expanded upon by Anderson [28]. This spectrometer incorporates a reflection grating with fixed rulings. The theory of grating spectrometers as they apply to this thesis will be reviewed below, followed by the specifications of the grating spectrometer.

3.2.1 Grating Theory

The review of grating theory assumes that the dispersion element relies on reflection rather than transmission. However, the fundamentals of grating theory apply to both types of gratings. The principles of dispersion and resolution in a grating spectrometer are highlighted as they apply to the simulations given in Chapter 4.

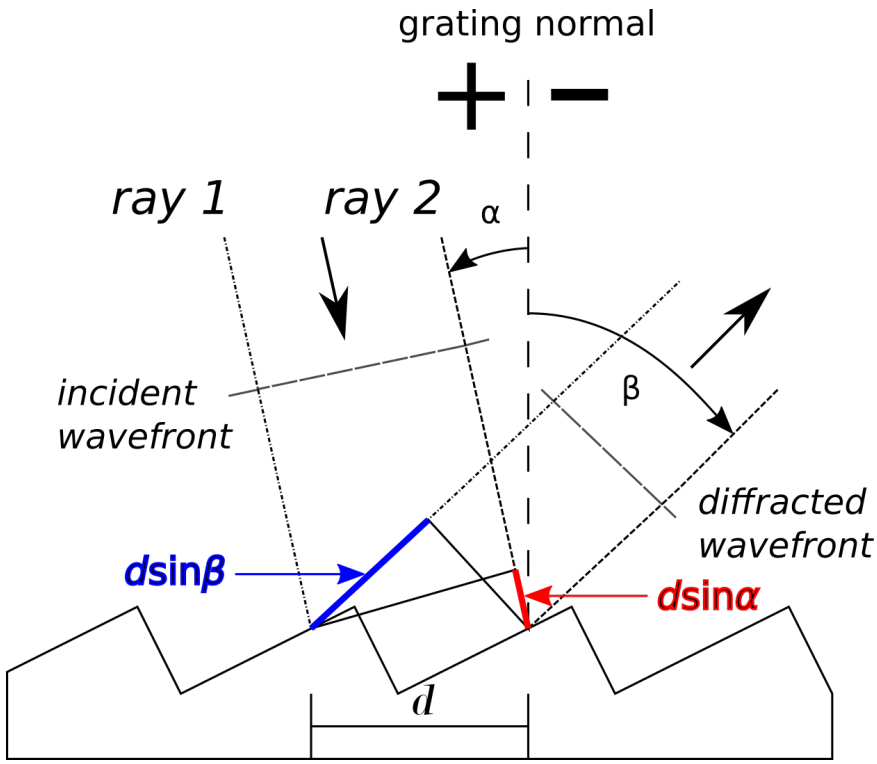

Figure 3.8: Diffraction of parallel rays from a reflection grating. The angle of incidence is give by α, and the diffracted angle is given by β. d is the slit or groove spacing. Note the sign convention for the diffraction modes. The grating equation is derived from the conditions for maximum constructive interference [88].

The Grating Equation

Light incident upon a grating will be diffracted by the grooves into a series of secondary wavelets. The *groove spacing*, d, or *pitch*, determines both the waveband and resolution of light to be examined by the grating. The result is constructive interference for a given wavelength of light, but only at particular angles. Convention dictates the angles of incidence and diffraction be given relative to the normal of the grating [88]. The sign of these angles depends on whether or not the ray is diffracted on the same side of the incident ray, as is shown in Figure 3.8. The incident angle, α, is always positive, while the angle of the diffracted wavefront, β, is measured clockwise from the grating normal. Thus, the incident rays and diffracted rays may lie on the same side of the grating.

From Figure 3.8, the path difference from adjacent grooves is given as $d\sin\alpha + d\sin\beta$. Constructive interference occurs when the path difference is equal to an integer multiple of

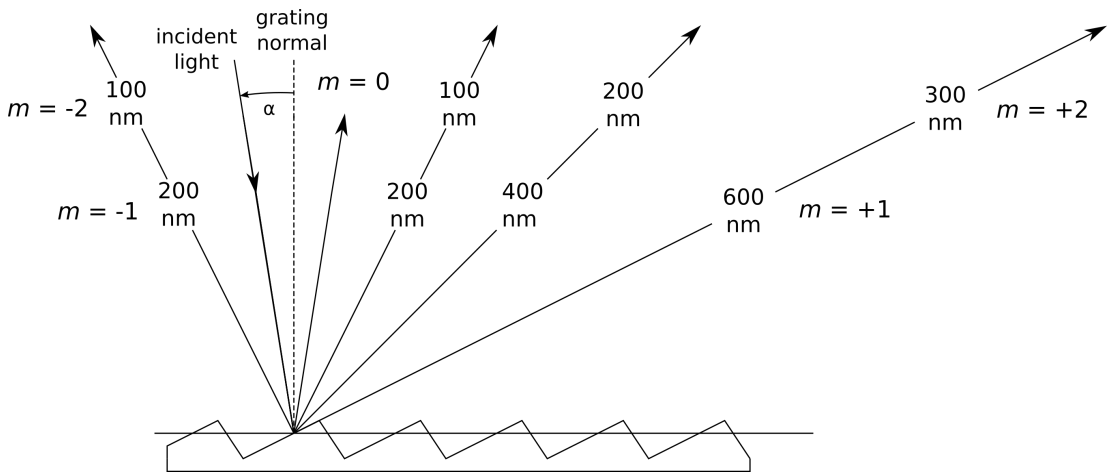

Figure 3.9: Wavelength overlap from diffraction modes. Overlapping wavelengths must be eliminated using order sorting mechanisms, such as filters [88].

the wavelength of the incident light λ. This relationship gives the *grating equation*, which is defined as

$$m\lambda = d(\sin\alpha + \sin\beta), \qquad [\mu\text{m}] \quad (3.7)$$

where m, an integer, is the *diffraction order* or *spectral order*.

From the grating equation it is clear that α and β may be satisfied for more than one wavelength, as shown in Figure 3.9. Several discrete wavelengths meet the conditions for constructive interference at the same angle. From the constraint that $|\sin\alpha + \sin\beta| \leq 2$, the grating equation sets the limit to the number of possible diffraction orders to $|m\lambda/d| < 2$. This limit means an incident ray may not be diffracted an infinite number of orders [88]. Written explicitly, the orders of diffraction that exist are given as

$$-2d < m\lambda < 2d. \qquad [\mu\text{m}] \quad (3.8)$$

There is a problem posed by multiple orders: the risk of overlapping spectra. The superposition of spectra from multiple orders is ambiguous without any form of filtering, or *order sorting*, since there is in general no means to determine wavelength using a detector.

Czerny-Turner Monochromator

From the work of Veenendaal, the grating spectrometer is configured as a Czerny-Turner monochromator [87]. The Czerny-Turner monochromator is a special type of grating spectrometer configuration which allows for the grating to transmit a narrow band of light chosen from a wide range of wavelengths. This configuration uses fixed mirrors and a rotating diffraction grating to select a desired wavelength from a polychromatic input [89]. For full details on the design of the Czerny-Turner monochromator, the reader is directed to either Anderson or Veenendaal [28, 87].

For the Czerny-Turner configuration, light incident to and diffracted by the grating is collimated. The collimation means that the incident and diffracted angles are constant. Thus the grating equation may be redefined from the difference and bisector between the two angles, called the *deviation angle* ($2\phi = \alpha - \beta$) and *scan angle* (θ, where $2\theta = \alpha + \beta$) respectively. The grating equation is defined in terms of the scan angle and *half deviation angle* ϕ [88]:

$$m\lambda = 2d\cos\phi\sin\theta. \qquad [\mu\text{m}] \quad (3.9)$$

In general m, d, and ϕ are fixed values for a given Czerny-Turner monochromator. Thus, the scanning capabilities of such a system are defined by the relationship between the wavelength and scan angle; the diffracted wavelength is directly proportional to the sine of the angle through which the grating rotates.

Dispersion

The phenomenon of dispersion is defined as the bending of a ray of light based on the frequency of incident light [90]. The *angular dispersion* is defined as the angular spread of a spectrum for a given order. The angular dispersion describes the change in diffraction angle with wavelength, D, as

$$D = \frac{\partial\beta}{\partial\lambda} = \frac{m}{d\cos\beta}, \qquad [\text{rad}/\mu\text{m}] \quad (3.10)$$

where β is derived from the grating equation.

It is clear that decreasing the groove spacing has the effect of increasing the angular dispersion. When the grating equation is substituted into Equation 3.10, the angular dispersion may be considered as a function of only the incident and diffracted angles:

$$D = \frac{\partial \beta}{\partial \lambda} = \frac{\sin\alpha + \sin\beta}{\lambda \cos\beta}. \qquad [\text{rad}/\mu\text{m}] \quad (3.11)$$

However, it is common practice to define dispersion as linear rather than angular. The *linear dispersion* is defined as the product of angular dispersion and the exit focal length of a given system, r':

$$L = r' \frac{\partial \beta}{\partial \lambda} = \frac{m r'}{d \cos\beta}. \qquad [\text{mm}/\mu\text{m}] \quad (3.12)$$

The *bandpass*, B, of a diffraction system is the interval of wavelengths that may be isolated and examined. For a monochromator, the bandpass is the quotient of the exit slit width, w'', and the linear dispersion:

$$B = \frac{w''}{L}. \qquad [\mu\text{m}] \quad (3.13)$$

Resolution

The *chromatic resolving power*, R, of an instrument is defined as [48]

$$R = \frac{\lambda}{\Delta\lambda}, \quad (3.14)$$

where $\Delta\lambda$ is the *limit of resolution*, or simply the *resolution*. The limit of resolution defines the minimum difference in wavelength between two lines of equal intensity that can distinguished.

As derived in Hecht, the theoretical resolving power for a diffraction grating is [48]:

$$R = \frac{\lambda}{\Delta\lambda} = mN, \quad (3.15)$$

which, from the grating equation is equal to

$$R = \frac{Nd(\sin\alpha + \sin\beta)}{\lambda} = \frac{W(\sin\alpha + \sin\beta)}{\lambda}, \tag{3.16}$$

where Nd is equal to the grating width W. Thus, the theoretical resolving power of a grating spectrometer is proportional to the width of the grating, the angle of incidence, and the wavelength of the incident light [48]. Since $|\sin\alpha + \sin\beta| < 2$, the maximum resolving power is twice the grating width over the wavelength being examined ($2W/\lambda$).

The above derivation assumes the resolution is limited solely by the grating, or is *grating limited*. Resolution may also be diminished by diffraction in the system, in which case the grating is *diffraction limited*. Similarly, should the slits used in the grating assembly not match desired wavelength, the resolving power may be defined in terms of the bandpass. This is referred to as being *slit limited*. For such a case the bandpass is redefined in terms of the *linespread function*:

$$B = \frac{\sup(w', w'')}{L}, \qquad [\mu m] \tag{3.17}$$

where $\sup(w', w'')$ is the limit superior of the entrance and exit slits. Note that when $w' = w''$, the original definition of bandpass is restored. The bandpass defines the full-width at half-maximum (FWHM) of a spectroscopic system. The result gives the resolving power as

$$R = \frac{\lambda}{B}. \tag{3.18}$$

As has been demonstrated by both Veenendaal and Anderson, the spectral response of a grating spectrometer can be approximated by a Gaussian to extract the true resolution of the grating in situ [28, 87].

Polarisation Sensitivity

The efficiency of a grating spectrometer is dependent on many factors, such as angles of incidence and diffraction, groove spacing, diffraction order (m), and grating material.

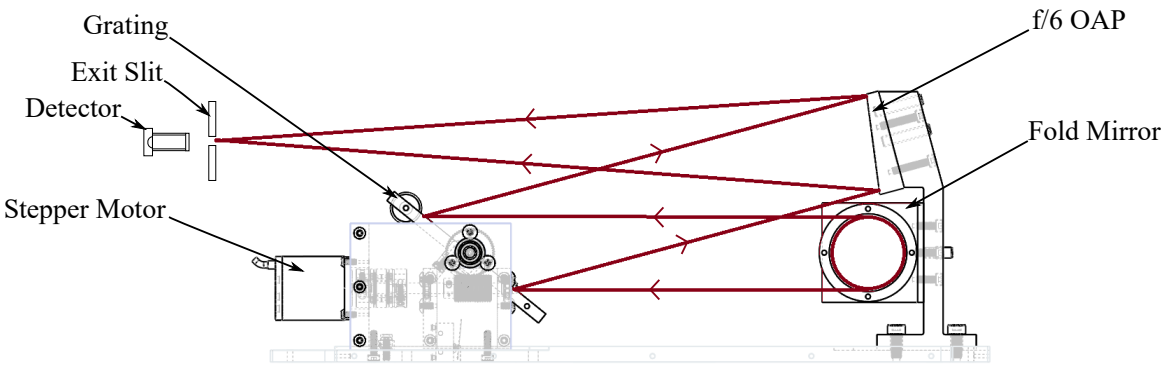

Figure 3.10: Side view schematic of the grating assembly designed by Veenendaal. Shown are the focussing optics, grating and stepper motor system, and the optical path to the detector system [87].

Another major factor in the efficiency is the polarisation of light incident to the grating spectrometer. In general, these factors do not directly impact the shape of the efficiency response curve of the grating, which is given at a peak wavelength. However, the diffracted power is sensitive to the polarisation of the incident beam and may result in anomalies, such as the well known Wood's anomalies, which manifests as sharp peaks and troughs in the efficiency curve [88]. Such anomalies can be limited by ensuring incident light is polarised parallel to the grooves of the grating, called *P-Plane* or TE-Polarised light.

3.2.2 Grating Properties

Preliminary designs of the grating assembly were produced by Veenendaal as part of a dispersion system for a Fabry-Perot interferometer [87]. The grating spectrometer was a Czerny-Turner monochromator designed to operate within a range of 220 μm to 300 μm. A system consisting of the grating, focussing optics, and a stepper motor gear train was built to minimize the working volume and optimize the resolving power of the instrument. A side view of the grating assembly is shown in Figure 3.10.

However, the cryogenic grating spectrometer designed by Veenendaal explored wavelengths outside the range of the source modules available for the PDPFTS. Therefore, with funding from Blue Sky Spectroscopy Inc., another grating module was designed and tested

by Anderson [28] to operate in the range of 285 μm to 500 μm. The final cryogenic grating spectrometer incorporated both the optical design from Veenendaal and the grating parameters of Anderson. The final specifications of the grating module used for the PDPFTS are given in Table 3.2, and details on the implementation and operation of the module can be found in Anderson [28]. Likewise, preliminary work into the verification of the cryogenic grating spectrometer can be found in Anderson *et al.* [91].

Table 3.2: Design specifications for the grating spectrometer designed to operate in the $285 - 500$ μm region [28].

Parameter	Value
Grating width, W	105 mm
Grating height/Beam diameter, D	50 mm
Diffraction order	1
Slit Spacing, d	312 μm
Deviation angle, 2ϕ	15°
Entrance focal length, r	310 mm
Exit focal length, r'	310 mm
Entrance slit width, w	5.0 mm
Exit slit width, w''	4.0 mm
Blaze angle, θ_B	39.4°

3.3 Instrumental Test Equipment

It should be clear to the reader that the PDPFTS represents a complex system. However, as will be shown, the complexity of the PDPFTS is rivalled by the complexity of the test equipment required to characterize the system itself. The test equipment may be described in terms of two modules: the source and the detector systems. This section also explores the data acquisition systems used to analyse the results.

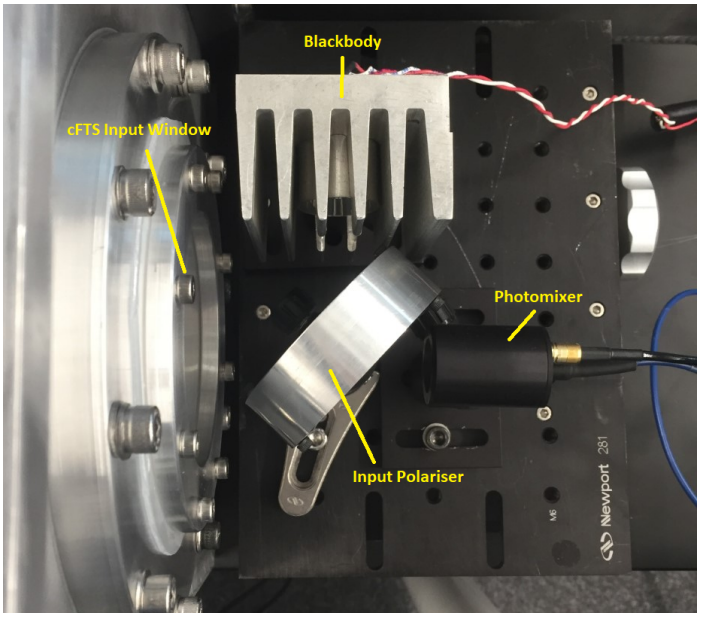

Figure 3.11: Source module of the PDPFTS configured to produce both a line and continuum. Above is a Scitec IR-12 wire-wound filament blackbody which is enclosed in a heat sink element with a parabolic reflector [92]. To the right is the output from a Toptica photomixer with a hyper hemispherical lens at the focus [93]. The outputs of the two sources are combined using an input polariser, which separates the two input ports of the cFTS, before passing into the PDPFTS.

3.3.1 THz Photomixer

The source module is capable of multiple configurations of photomixers and blackbodies. Through the inclusion of a polariser on the input, it is possible to simulate either an absorption or emission feature using the complementary input ports as shown in Figure 3.11. The blackbody source is unpolarised and incoherent, while the photomixer source is polarised and coherent. Figure 3.11 depicts the source module configured to produce both a line and continuum input.

Photomixer Theory

A THz photomixer consists of two independent tunable lasers with different frequencies such that the frequency difference (or *heterodyne frequency*) matches the desired output radiation [94]. These tunable lasers are both incident on a single photomixer element - generally a photodiode. From the superposition theorem, when two lasers of differing frequen-

cies are incident on the photomixer element, the time-dependent electric field amplitude on the photomixer is the linear sum of the individual fields. These fields are defined as $E_1 = E_{01}\cos(2\pi\nu_1 t)$ and $E_2 = E_{02}\cos(2\pi\nu_2 t)$. Recall that the power is proportional to the time-average square of the electric field. Thus the time-dependent optical power incident on the photomixer element is

$$P(\nu,t) = |E_1|^2 + |E_2|^2 + \sqrt{m}E_{01}E_{02}[\cos 2\pi(\nu_2-\nu_1)t + \cos 2\pi(\nu_2+\nu_1)t], \quad [\mathrm{W}] \quad (3.19)$$

where $\nu_2 - \nu_1$ represents the heterodyne frequency, and the *mixing efficiency*, m, is a value between 0 and 1, representing the degree of overlap; $m = 1$ with perfect overlap, and $m = 0$ with no overlap. In the system used in this thesis, the laser outputs were transmitted through 2 m of single mode fibre, with the two outputs sharing a beam over a significant distance. Consequently, the photomixers were assumed to have a perfect overlap.

Whether the photomixer element is a photoconductor or photodiode, Equation 3.19 clearly indicates there will be an induced current at both the sum and heterodyne frequency. Thus, to produce a THz signal, two conditions must be met. Firstly, $h\nu_1$ and $h\nu_2$ must both be greater than the bandgap of the photoconductive material used. Secondly, $\nu_1 \approx \nu_2$ such that the heterodyne frequency falls in the proper band. Under these conditions, the first cosine term in Equation 3.19 represents the modulation of the photoconductance at the heterodyne frequency. The second term varies at approximately twice the heterodyne frequency which by nature has a much shorter time scale than the electron-hole recombination time, τ, and therefore does not contribute significantly to the photoconductance. The instantaneous power on the photomixer element can be approximated as

$$P(\omega,t) = P_0 + \sqrt{mP_1P_2}\cos\omega t, \quad [\mathrm{W}] \quad (3.20)$$

where $P_0 = P_1 + P_2$ represents the total incident power averaged over time, and $\omega = 2\pi(\nu_2 - \nu_1)$ represents the heterodyne angular frequency.

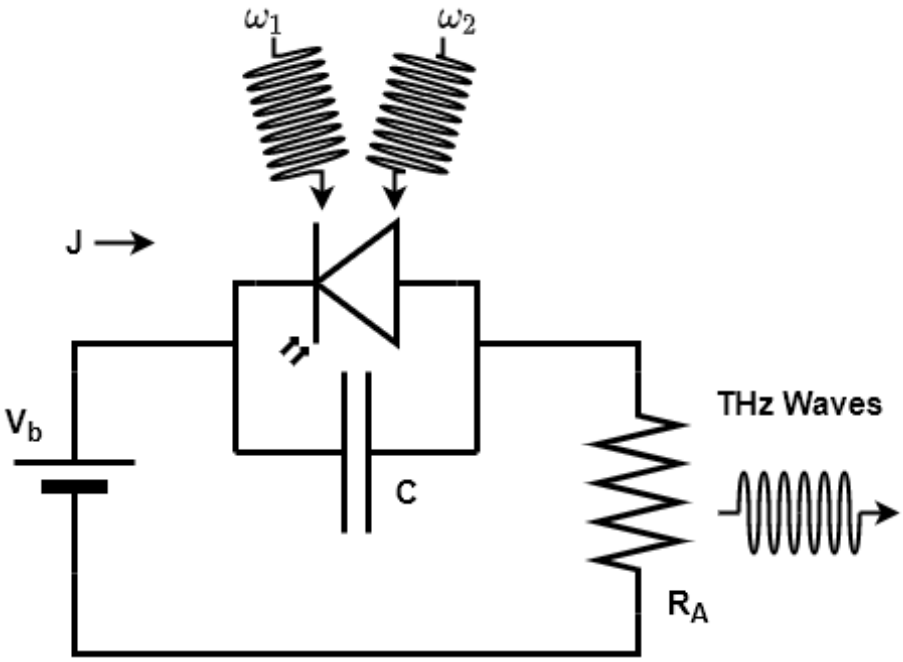

Figure 3.12: Basic equivalence circuit diagram for a biased photomixer and antenna.

With both beams incident on the photomixer element, there are then two mechanisms for emitting THz radiation: the Large Area Emitters (LAE) and the Antenna Emitter (AE). The AE represents the more common system due to its higher efficiency, though there is a restriction to the input power to the photomixer. On the other hand, the LAE can be used with more powerful lasers and is less demanding to fabricate. The photomixer system used throughout this thesis is based on the AE mechanism, and therefore the LAE will not be discussed. For a comparison of the AE and LAE, the reader is directed to Preu [95].

Radiation incident on the photomixer element produces electron-hole pairs, which constitute the photocurrent of the system. The effectiveness of a photomixer is based on high carrier mobility, leading to a short time response, τ. To emit THz radiation, the photocurrent produced by the photomixer element is directed to an antenna, which couples the electric field with free space. In essence, the antenna converts the induced AC current into THz radiation. Several types of antennae exist, such as log-spiral, log-periodic, bow-tie, and dipole. The differing structures have differing effects: log-spiral and log-periodic antennae produce circular polarised light while bow-tie and dipole antennae produce linear polarised

light. An equivalent circuit diagram of a photomixer and antenna is shown in Figure 3.12.

The incident power on the photomixer element produces a photocurrent in the antenna, defined as

$$J(t) = C\frac{\mathrm{d}V(t)}{\mathrm{d}t} + G(t)V(t) = \frac{V_b - V(t)}{R_A}, \qquad \text{[A]} \quad (3.21)$$

where C is the capacitance of the photoconductive gap, V is the potential at the gap, $G(t)$ is the photoconductance of the antenna, V_b is the bias voltage, and R_A is the radiation resistance of the antenna. It can be shown that the THz power output, $P_{THz}(\omega)$, can be approximated as [96]

$$P_{THz} = \frac{J_0^2 R_A}{2[1+(\omega\tau)^2][1+(\omega R_A C)^2]}, \qquad \text{[W]} \quad (3.22)$$

where $J_0 = G_0 V_b$ is the DC photocurrent, and G_0 is the is the time-averaged photoconductance of the incident power. Note that the power output of the photomixer is proportional to the square of the bias current. This relation was exploited to increase the signal of the photomixer to boost the measured signal-to-noise ratio (SNR) of the line source.

The original development of the photomixer was done by Makiwa [97]. The design was further modified to change the frequency range and increase the output power of the system as outlined by Veenendaal [87]. A major overhaul was performed on the photomixer system to increase both the temperature stability of the input lasers and the output power of the photomixer. Additional lasers were purchased to increase the available range of the photomixer, and a second photomixer system was developed.

Technical Specifications

The photomixer used throughout this work was a TOPTICA Photonics InGaAs photodiode with an excitation wavelength of 1.5 μm [93]. The photomixer utilizes a bow-tie antenna, which produces linearly polarised light. The polarisation state of the radiation emitted by the photomixer allows for the system to be oriented such that the coupling of the photomixer to the input polariser is 100% efficient. Additionally, the InGaAs module is capable of much higher powers compared against other commercially available models and

offer consistent output power over wide band of frequencies.

The lasers available for the PDPFTS are Distributed FeedBack (DFB) lasers produced by Fitel with nominal 25°C frequencies of 193.00 THz, 193.38 THz, 193.75 THz, and 194.50 THz, where each diode has a linewidth of 5 MHz [98]. Therefore the uncertainty in the difference frequency is roughly 7 MHz, which is far below the resolution of the cFTS, which is roughly 1 GHz. Thus, for all intents and purposes the difference frequencies generated by the two photomixers are monochromatic and unresolved.

Table 3.3 shows the expected nominal beat frequency achieved with the combination of these lasers. Previous work has shown that DFB lasers exhibit a temperature dependence of -0.012 THz/°C. Since the temperature may range from 15°C to 35°C, a single DFB laser varies in frequency by $\pm$0.12 THz, and therefore the range of the photomixer may vary by twice this value from the nominal 25°C beat frequencies. The calibration of the temperature dependence for each of the photodiodes used in this thesis is given in Appendix C.

Table 3.3: Beat frequencies produced by the available DFB lasers at their nominal 25°C frequency for the photomixer.

	193.00 THz	193.38 THz	193.75 THz	194.50 THz
193.00 THz	–	0.38 THz	0.75 THz	1.50 THz
193.38 THz	0.38 THz	–	0.37 THz	1.12 THz
193.75 THz	0.75 THz	0.37 THz	–	0.75 Thz
194.50 THz	1.50 THz	1.12 THz	0.75 THz	–

3.3.2 Test Facility Cryostat

As shown in Figure 3.1, both the grating and detector operate at cryogenic temperatures and are mounted in a large-scale cryogenic facility. The Test Facility Cryostat (TFC) is a closed-system cryogenic facility with an internal volume of $\sim$70 L (see Figure 3.13). The TFC is cooled to a temperature of 4 K using two Cryomech PT415 pulse tube coolers operating in parallel [99]. Also included in the TFC is a Chase Research Cryogenics He-10 cooler that can maintain temperatures of around 250 mK for $\sim$48 hours, which is suitable

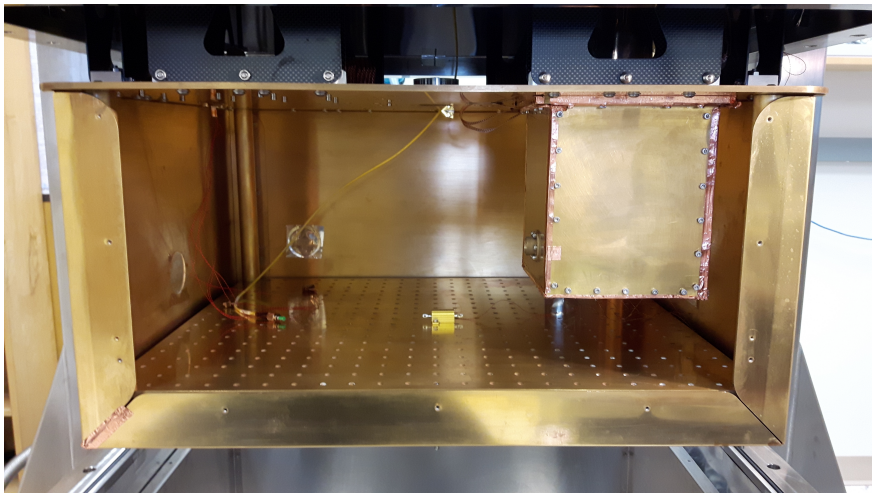

Figure 3.13: 4 K working volume of the TFC with the He-10 cooler. The TFC offers a wide selection of viewpoints within the ∼70 L volume. CFRP support plates and flexible thermal straps reduced vibrational noise from the pulse tube coolers.

for cryogenic detectors [100]. Polypropylene windows and a combination of thermal infrared and band limiting filters allow a selected band of infrared light to be passed into the cryostat from an external source. For a complete description of the design and construction of the TFC, refer to Veenendaal [101].

3.3.3 Cryogenic Detector

The cryogenic detector used throughout this work was developed by Gom [64] as a Ge:Ga composite bolometer with a NEP of $\sim 10^{-16}$ W$/\sqrt{\text{Hz}}$ [53]. The bolometer element is a nuclear transmutation doped (NTD) small rectangle mounted on a thin sapphire disc. To enhance the absorption efficiency of the bolometer, a thin bismuth film was used to coat the back side of the bolometer. As shown in Figure 3.14, the detector system includes an integrating cavity and f/3 Winston horn, both of which are gold-plated [64]. These components both serve to collect and concentrate incident radiation onto the bolometer element, further enhancing the overall absorption efficiency. A low-pass 35 cm^{-1} edge filter was included to limit stray radiation from reaching the bolometer. For full details of the design and characterization of the cryogenic bolometer the reader is directed to Gom [64] and Naylor *et al.* [53].

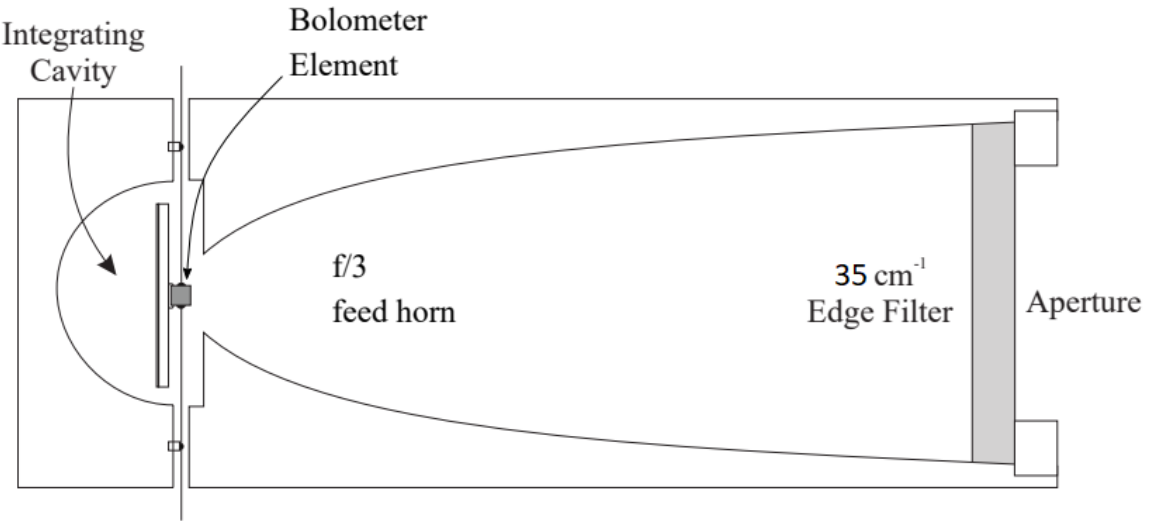

Figure 3.14: Schematic of the cryogenic bolometer detector system indicating the feed horn, integrating sphere, and edge filter [64].

The bolometer was mounted to the Chase Research Cryogenics He-10 refrigerator (uses two ^{3}He stages and one ^{4}He stage) in the TFC and enclosed within radiation shields cooled to 4 K. With this configuration the bolometer reached temperatures of $<$300 mK, thereby increasing the sensitivity of the detector. However, since the detector system was repurposed from the another project [53], the f/3 feed horn did not match the f/6 camera optics from the grating module. The exit slit of the spectrometer was placed on the entrance of the feedhorn. This exit slit had a width of 4 mm, which was determined by the camera optics.

3.3.4 System Overview

The high-level system overview, shown in Figure 3.1, depicts the four main modules: the source, FTS, grating, and detector. In order to properly characterize the PDPFTS, rigorous metadata collection and analysis must be performed. Additional considerations were required to ensure the system operated in a repeatable manner. Consequently, the complexity of the instrumental test equipment exceeds that of the instrument itself. This is clear from Figure 3.15, which provides an in-depth system engineering view and outlines key metadata collected to characterize the PDPFTS.

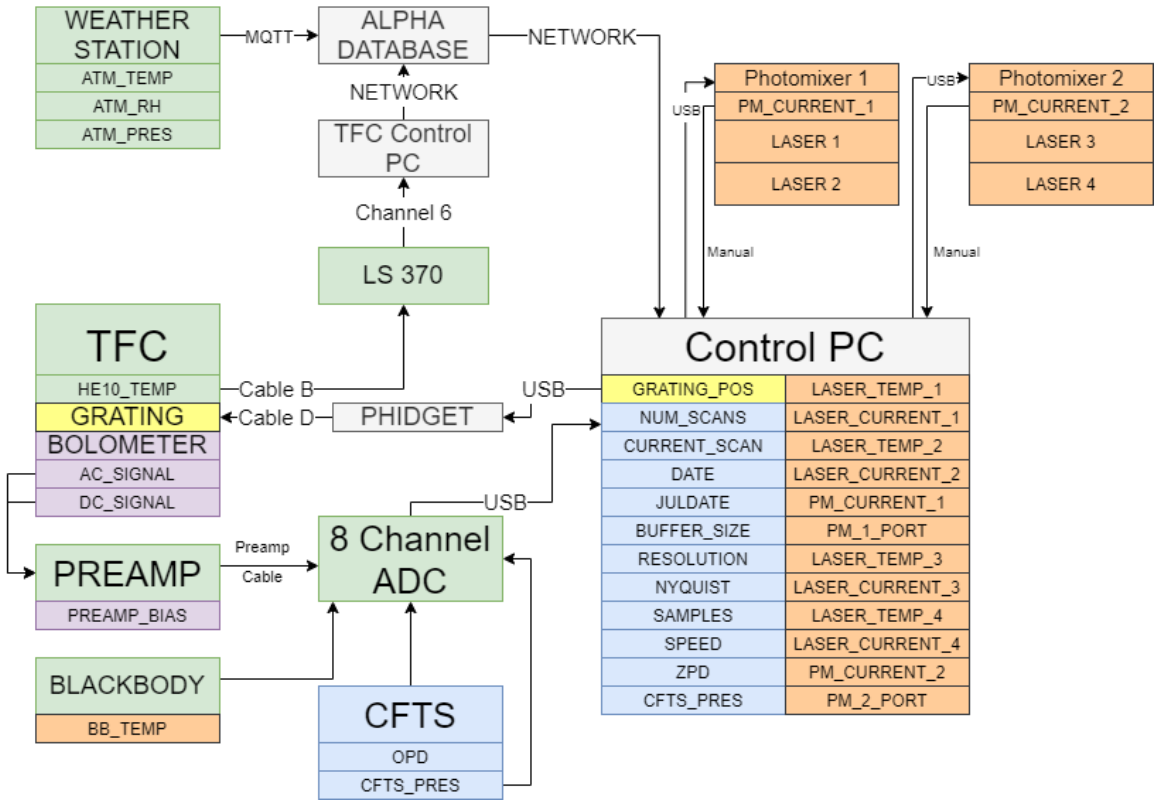

Figure 3.15: High-level diagram of the metadata gathered to characterize the PDPFTS, with items colour-coded based on module. Orange represents the source module, blue represents the cFTS, yellow represents the grating module, and purple represents the detector. Additionally, items in green represent additional test equipment, and grey represents control hardware. In the case of the TFC, this includes a plethora of thermometers which monitor the health of the cryostat.

The overview provided in Figure 3.15 demonstrates that the PDPFTS incorporates a complex test equipment to evaluate the instrument under test. Each of these components requires a myriad of control and data acquisition elements. Crucial metadata must be meticulously measured and swiftly stored. Thus, a framework was established to ensure these parameters are met efficiently, and errors in any stage of data collection and system control are properly flagged. This framework forms the basis of ongoing work to establish a robust database for the PDPFTS system.

Control of the grating module was incorporated into legacy code developed for the cFTS. The control software is designed to track the steps of the grating stepper motor to

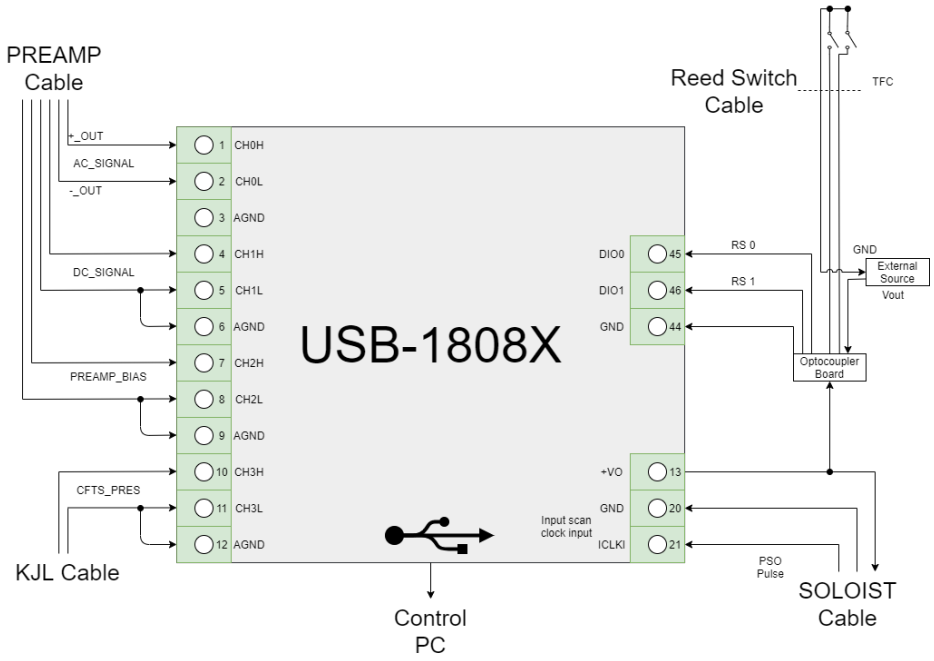

Figure 3.16: Schematic of the DAQ configuration, increasing the available metadata for the characterization of the PDPFTS. The preamp cable returns the expanded metadata of the detector system, the KJL cable reports the internal pressure of the cFTS, the Reed Switch Cable returns the signal for homing the grating module, and the SOLOIST Cable monitors the PSO pulses of the cFTS stage.

monitor the grating angle. Without a position encoder, this requires homing the system to a known position. Code for this purpose was originally developed by Veenendaal [87] and incorporated into the updated software with minimal changes. However, preliminary attempts to calibrate the grating angle were erroneous, which was further compounded by issues such as missed steps and hysteresis. Ultimately, these complications proved insignificant as the position of the grating could be readily determined from spectroscopic measurements of a known source.

The grating housing designed by Veenendaal used one reed switch which acted as a fiducial. However, the homing procedure was increasingly susceptible to noise in the reed switch, and the repeatability of the homing procedure was called into question. To reduce the noise, a H11A1 optocoupler board was integrated into the reed switch system [102]. To introduce repeatability into the homing procedure, a new mechanism was proposed to use two reed switches connected to an optocouple system. The full design included two boards

with the intention of being incorporated into a future grating module housing with multiple homing positions. However, due to issues arising from the grating mechanism missing steps a fibre optics based rotary optical encoder was proposed as a means to both track steps in the motor assembly and provide a homing mechanism for the grating. The optical encoder is currently being implemented by the Astronomical Instrumentation Group (AIG).

Much of the metadata was collected through a Measurement Computing USB-1808X data acquisition device [103]. A high-level schematic of the configuration of the system is shown in Figure 3.16. One enhancement to the system is the inclusion of metadata for the cryogenic bolometer. Previous projects which utilized the detector module relied solely upon the AC signal received from the bolometer. By expanding the existing framework to include measurements of both the DC signal and bias of the detector system, the bolometer may be optimally biased for both the sensitivity and responsivity based on the V-I curve of the detector.

3.4 PDPFTS Optical Layout

As discussed above, the source module can exploit polarisation using complimentary inputs to mimic absorption and emission features (Figure 3.11). Radiation incident to the cFTS is then encoded, modulated, and decoded as it passes through to the output. From the cFTS, radiation then passes through the TFC window through two low-pass filters, first a 100 cm^{-1} filter cooled to 40 K and then a 50 cm^{-1} filter cooled to 4 K. Before entering the grating module, radiation passes through yet another low-pass filter with a cut-off of 50 cm^{-1}. From here the radiation is reflected by a 45° fold mirror onto the cryogenic grating where a band of light is directed to a second mirror which focusses the beam onto the exit slit placed directly in front of the detector. The optical configuration of the PDPFTS is shown in Figure 3.17.

At present, neither the source module nor the cFTS may be cryogenically cooled, while the grating module is cooled to 4 K and the detector is cooled to 0.3 K. Consequently, this

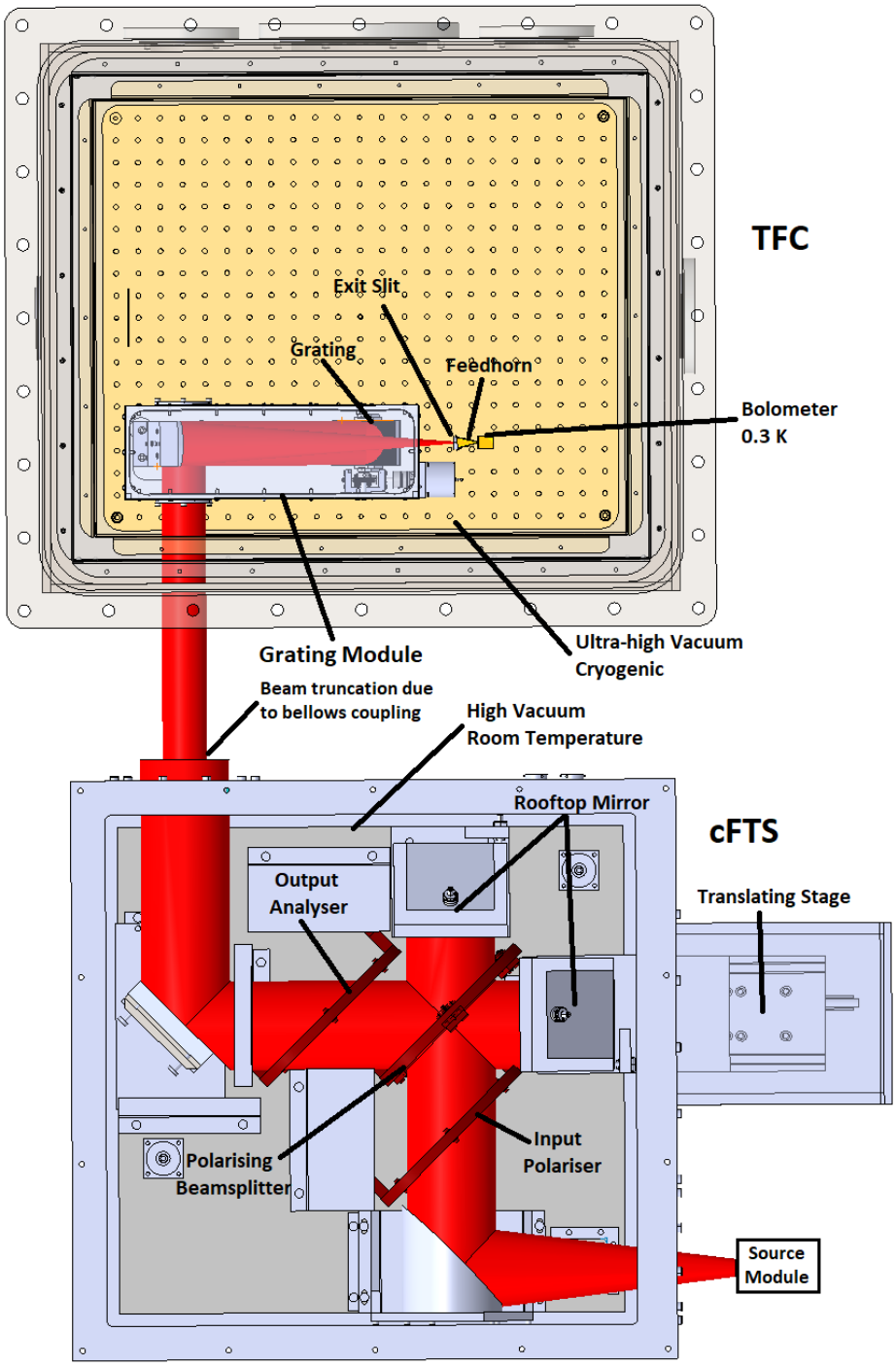

Figure 3.17: Optical layout of the PDPFTS. Light incident from the source module passes through the cFTS into the grating spectrometer. Light within the bandpass selected using the grating module is then focussed onto the cryogenic detector. Note the truncation of the collimated output of the FTS due to a vacuum bellows assembly (not shown) joining the cFTS to the TFC, reducing the overall efficiency of the PDPFTS by a factor of $\sim$12.5.

leads to difficulties in achieving slit-to-slit alignment with the grating spectrometer as its focus is hidden deep within the TFC ($\sim$2 m from the entrance slit). In order to more easily align the PDPFTS system, the cFTS was modified to have a plane mirror rather than an off-axis parabola mirror to have a collimated output pass through the TFC window into the grating module. The cFTS and TFC are coupled using a bellows system that also maintains a vacuum from the cFTS-side of the coupling. The bellows assembly serves to maintain the alignment of the system and reduce atmospheric absorption features.

Due to the hybrid nature of the PDPFTS and the legacy design of each component, each system was designed independently to accommodate beams of differing diameter. The beam internal to the cFTS is elliptical with a minor diameter of $\sim$110 mm and major diameter of $\sim$180 mm, the window of the TFC and bellows have a diameter of 70 mm, the grating module input has a diameter of 40 mm, and the grating has a width of 50 mm. Thus, there is a truncation in the beam and photons are lost in the coupling, the result of which is a reduction of the overall efficiency of the PDPFTS by a factor of $\sim$12.5 (see Chapter 6). The system is currently being optimized to focus the output beam of the cFTS in conjunction with a cryogenically cooled entrance slit to not only eliminate the truncated power input into the TFC, but also maximize the resolution of the grating module. The experimental configuration of the PDPFTS is presented in Table 3.4.

Table 3.4: Experimental configuration of the PDPFTS.

Configuration			
Units	cm^{-1}	μm	GHz
Blackbody Temperature (K)		$\sim$1200	
Tunable Photomixer Frequency	18 - 37	270-555	540 - 1000
Spectral Coverage	20 - 35	285-500	600 - 1050
Spectral Resolving Power	580 - 1020	580 - 1020	580 - 1020
Grating Wavelength Range	20 - 35	285-500	600 - 1050
Grating Resolving Power	70-210	70-210	70-210
Detector Temperature (mK)		$\sim$300	

3.5 Conclusions

Chapter 3 outlined the theory and design of a hybrid PDPFTS system and its accompanying test suite. Section 3.2 introduced the theory of diffraction gratings, in particular the concept of the Czerny-Turner monochromator, and outlined the parameters of the grating module used throughout this work. Section 3.1 outlined the theory and advantages of the Martin-Puplett interferometer and introduces the cFTS. The instrumental test equipment, which includes the source module, cryostat, detector module, and control system, are discussed in Section 3.3. Finally, the configuration of the PDPFTS is presented in Section 3.4.

As has been highlighted throughout this chapter, integration of the PDPFTS proved to be chimeric. Not only is the PDPFTS an amalgamation of several different modules, the notation between these modules differ drastically. This is highlighted in Table 3.4, where three different units are used to represent the spectral range and resolution as per convention for the differing modules: GHz for the photomixer source, μm for the grating module, and cm^{-1} for the FTS.

Similarly, not all of the modules are cryogenic in nature, nor are they all capable of being under vacuum. The backbone of the system, the cFTS, is too large to be held within the TFC and lacks the capability to be cryogenically cooled on its own. The source module as well is unable to be held under vacuum, introducing a small volume of atmosphere through which incident radiation must travel before entering the cFTS. Improvements will be discussed in Chapter 6.

Chapter 3 emphasizes that the PDPFTS is a solution to the fact that in order to achieve the highest possible SNR, an FTS must operate in a limited band. With the theory underlying the PDPFTS and parameters of the system defined, Chapter 4 explores the simulations of the PDPFTS.

Chapter 4

Simulating the Spectral Performance of a PDPFTS

Без муки нет науки. (Without suffering there is no learning.)

RUSSIAN PROVERB

4.1 Introduction

As discussed in Chapter 3, the goal of obtaining the highest sensitivity, high resolution FTS measurements with state-of-the-art infrared detectors demands that the bandpass be restricted. The goal of this thesis is to develop the world's first far-infrared post-dispersed polarising FTS (PDPFTS) and to examine some of the challenges associated with the data obtained using it. A theoretical simulator was designed to generate expected interferograms to guide the development of a processing pipeline to address the challenges posed by analysing data produced by a PDPFTS and to provide a comparison for experimental results (Chapter 5). Of particular interest is the impact of the limited bandpass on spectral features and the difficulties faced in processing, specifically in phase correction. By examining the predicted models for the PDPFTS, it is possible to simulate the data retrieved through such an instrument and ultimately inform the design of the cryogenic PDPFTS, as well as identify the required calibration products and key considerations of processing pipelines.

In this chapter I present the simulator I developed to produce PDPFTS data for comparison with experimental results. This simulation is based on a mathematical model that

is implemented in the Interactive Data Language (IDL) programming language, which is an object-oriented visualization software popular in the fields of astronomy, atmospheric physics, and medical imaging since its inception in the 1970s [104]. IDL is a fourth-generation language which includes a suite of mathematics and statistics packages, as well as a host of graphics, image-processing, mapping, and data-manipulation features. IDL is well equipped to efficiently manipulate arrays and to handle and visualise large datasets, making it highly suited to the simulation process.

In preparation for the experimental results, a processing pipeline was developed for the PDPFTS. The simulated data provided the input for the development of a processing pipeline, and simulations pushed through the pipeline provided theoretical results which could be compared with experimental data. When I compared the simulated results I found there were corrections required to improve the pipeline. In particular, an issue was discovered in the implementation of phase correction as the extraction of a linear phase from a narrow band proved to be more complex than previously expected (see Chapter 5). The initial design of the PDPFTS processing pipeline, including a description of the relevant metadata, is discussed below.

4.2 Parameters

The PDPFTS simulator incorporated the specifications of both the calibration FTS (cFTS) and cryogenic grating spectrometer, as outlined in Chapter 3, which determined both the bandpass and resolution of the simulated spectra. These specifications were used so that the simulator would provide spectra which are directly comparable to data taken using the PDPFTS. Starting from a generic source, which consists of a blackbody continuum with a combination of emission and absorption lines, I superimpose the restriction of the band by the grating and instrumental line shape (ILS) of the FTS. From these spectra I then generate realistic interferograms onto which I can further introduce phase errors and add noise, all with the goal of generated simulated data which can be compared with experi-

mental results. Initially the spectral response of the PDPFTS was explored without phase error or noise. These components were added to the simulator later to bring more realism into the simulations.

As part of the pipeline development, the simulations produced 10,000 separate interferograms. These simulations allowed for the exploration of processing issues, such as accuracy and efficiency. Thus, the simulations allowed for an analysis of the tradespace between integration time and the signal-to-noise ratio (SNR). The findings of these simulations were used as a means of evaluating how data should be analysed, leading to the development of a series of metrics which would be indicative of some issue in the data, such as a cosmic ray event or a large phase error (see Section 4.4.2). With these defined metrics a triage system was integrated into the processing pipeline (see Section 4.4.3).

A simple outline of the experiment is given in Figure 3.1. However, as highlighted throughout Chapter 3, there are numerous parameters in both the instrumental test equipment and the instrument under test. To evaluate the performance of the PDPFTS, the system must be able to monitor the broad range of parameters shown in Figure 3.15. The first task was to identify the many parameters which must be monitored while testing the PDPFTS (see Figure 4.1). These parameters form the basis for deciding whether the data are good, fair or poor. Data are considered good if they pass assessment criteria (discussed in Section 4.4 below) indicating they require no further attention and may be processed as is; fair if they pass a specific subset of the assessment criteria but require additional user interaction (ie. the failed criteria are not critical to processing, such as higher noise); poor if they fail to meet the baseline assessment criteria, such as if a portion of the interferogram is missing. Once categorized, the good data is processed without any further effort, the fair data is analysed with user intervention depending on the failed criteria, and the poor data are probed for troubleshooting but ultimately rejected. This triage approach is necessary to accommodate the large data volumes that are produced by the PDPFTS ($\sim$48 kB/min).

In regards to the method of triage, simulations serve as a means of looking forward:

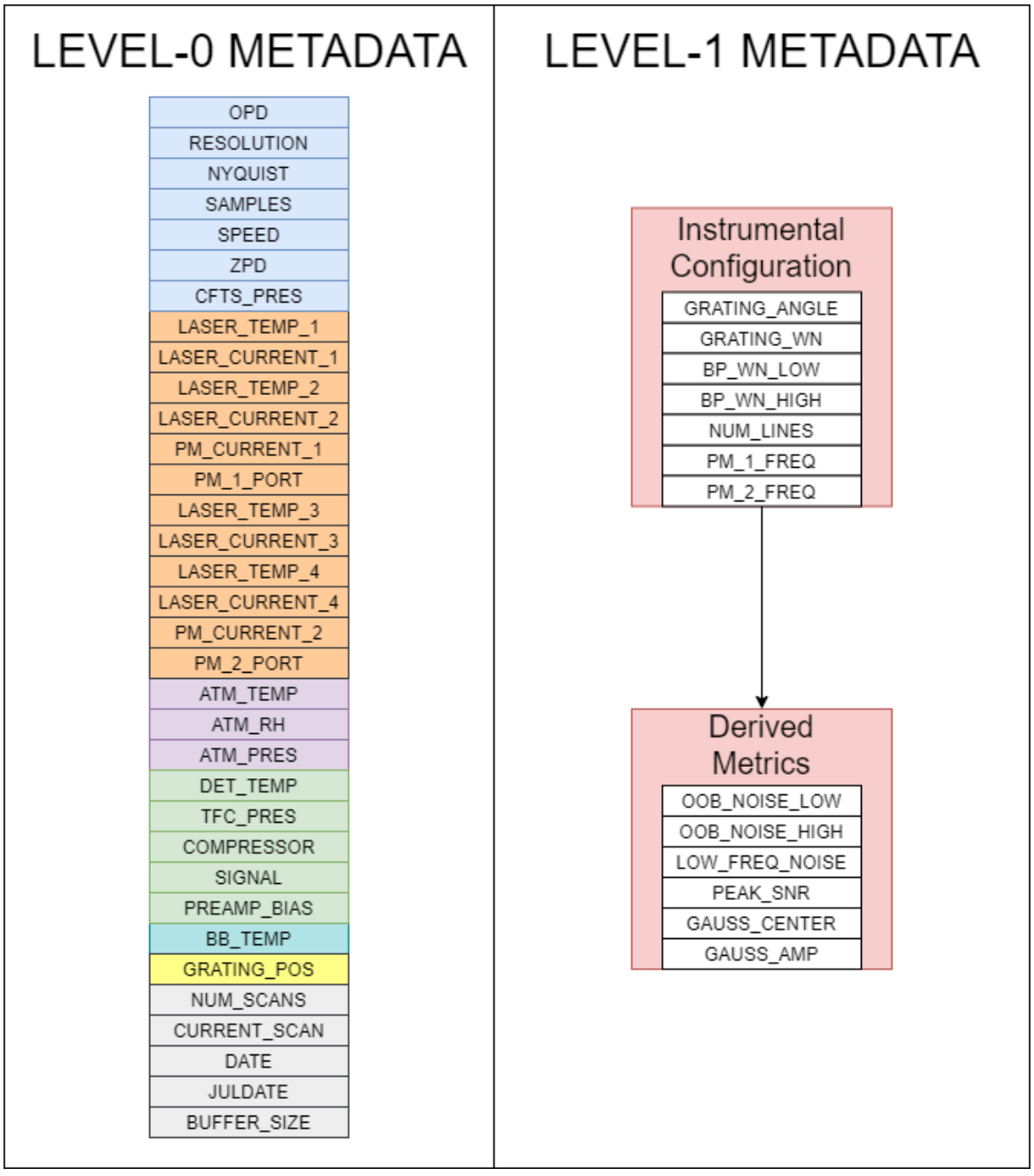

Figure 4.1: Categorization of the metadata obtained from the PDPFTS and instrumental test equipment. Level-0 consists of metadata directly measured from the instrumental suite, while level-1 is information processed from the level-0 data. Metadata is colour-coded based on modules. Blue represents the FTS module, orange represents the source module, green represents the detector and cryogenic system, purple represents the atmospheric conditions, teal represents the blackbody source, yellow represents the grating module, and grey represents housekeeping information.

a thorough understanding of expected results guides the troubleshooting process and data analysis. Simulating extremes such as large phase errors determines the limit between fair and poor data. Other situations may arise where part of the test equipment stops operating part way through a scan. Regardless of the potential causes, each of the simulations aided in deriving a set of metrics against which all interferograms will be compared. The simulations serve to improve our understanding of the PDPFTS, but are also key to establishing a data processing pipeline and metrics for identifying issues in the data. The simulator provides theoretical results which can be compared against experiment.

4.2.1 Simulating the Profiles

In simulating the performance of the PDPFTS and its test equipment, one is faced with a variety of spectroscopic conventions: the photomixer is given in frequency, ν (THz), the grating is defined in wavelength, λ (μm), and the polarising FTS operates in wavenumber, σ (cm^{-1}). As these conventions differ, one is frequently required to convert between them. Since the FTS defines the resolution of the instrument, the spectral response of both the photomixer and grating are converted to wavenumber to match the currency of the FTS. The conversion factors are $\sigma = \nu/c$ for the photomixer, where c is the speed of light, and $\sigma = 1/\lambda$ for the grating spectrometer. One interesting aspect of this hybrid instrument is that while the resolving power of the FTS increases with wavenumber, the resolving power of the grating decreases.

The native spectral resolution of the simulator was set to be 1×10^{-5} cm^{-1}, which implies a maximum optical path difference (OPD) of 100,000 cm. However, in practice the cFTS only has a resolution of 0.028 cm^{-1}, corresponding to a maximum OPD of $\sim$17.5 cm. While the simulated resolution may seem extreme, it was chosen not only because it allows one to resample the generated spectrum to match the resolution of any FTS, but also, as will be shown below, it is sufficiently high to explore the linewidths of the narrow linewidth lasers which drive the photomixer. Thus, the simulated sources are generated with a spec-

tral resolution capable of resolving features unresolvable to the cFTS. An algorithm is then used to resample the spectrum to match the resolution of the cFTS.

Since the grating profile is generated in the wavelength domain, the central wavenumber in the FTS spectrum must be converted to wavelength. Recall from Section 3.2.1 that the full-width at half-maximum (FWHM) of the approximated Gaussian profile is equal to the bandpass, B, of the grating system. From this relation, the width of the Gaussian may be determined from $\Delta = B/(2\sqrt{\ln(2)})$. An algorithm was written to determine the width of the Gaussian by first calculating the linear dispersion of the grating. Recall that for the Czerny-Turner monochromator the diffracted angle may be written in terms of the deviation angle, ϕ, and scan angle, θ, as $\beta = \theta - \phi$, meaning that the angular dispersion can be rewritten as

$$D = \frac{m}{d\cos(\theta - \phi)}. \qquad [\text{rad}/\mu\text{m}] \quad (4.1)$$

The linear dispersion is defined in Equation 3.12 as $L = r'D$, where r' is the exit focal length. The bandpass is then calculated as the quotient of the exit slit width, w'', and the linear dispersion (Equation 3.13). Thus, Equation 4.1 emphasizes the fact that the bandpass of a Czerny-Turner monochromator varies nonlinearly with the angular position of the grating, meaning the width of the Gaussian profile also varies nonlinearly across the 20 - 35 cm^{-1} band. Likewise, since the width of the exit slit is fixed, the monochromator becomes slit limited after the grating is rotated past a certain angle, further modifying the resolution across the band (see Section 3.2.1). Furthermore, Equation 3.12 shows that the bandpass, and therefore the resolving power, is a function of wavelength through the grating equation (Equation 3.12).

With the determined resolution, the Gaussian approximation of the grating profile was calculated as

$$g(\lambda) = a\exp\left(-\frac{(\lambda - \lambda_c)^2}{2\Delta^2}\right), \qquad [\mu\text{m}] \quad (4.2)$$

where a is the amplitude of the Gaussian and λ_c is the central wavelength. The entire profile

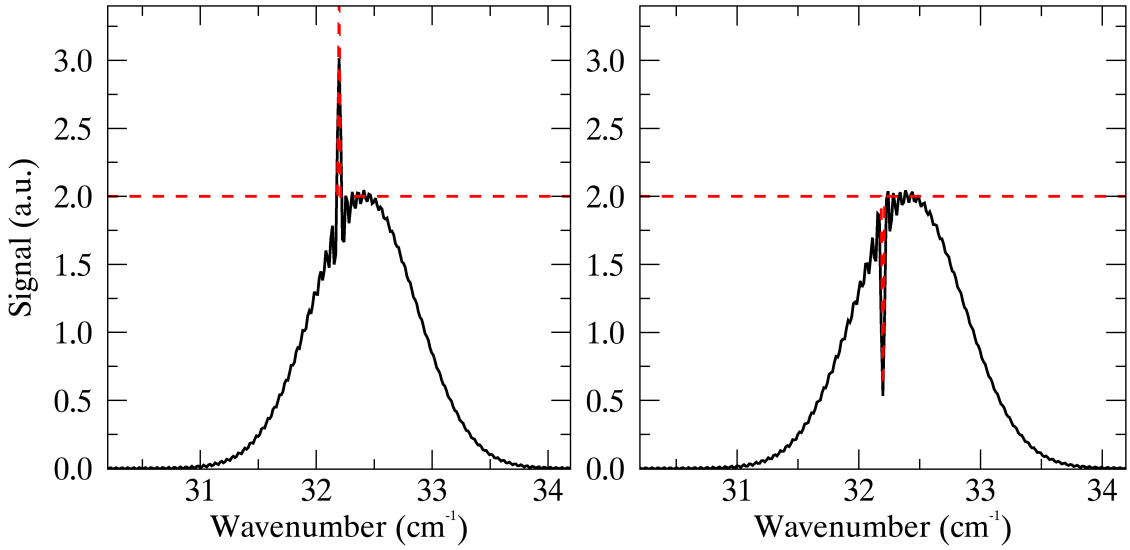

Figure 4.2: Preliminary simulations of a PDPFTS spectrum including an unresolved line source superimposed on a blackbody continuum. The left panel depicts the system with an unresolved line source in emission, and the right image depicts the unresolved line source in absorption. The total signal ignoring the bandpass of the grating is shown in red.

is then converted back to wavenumber.

The same method was used to simulate the response of the PDPFTS to an unresolved line source produced by the photomixer. Based on the specifications of the lasers used in the photomixer (see Appendix C), the line source was generated as a Gaussian with a width of $\sim$7 MHz ($\sim$0.0002 cm^{-1}), which is narrower than the cFTS is capable of resolving. The resulting line source profile was then superimposed onto the grating profile. Figure 4.2 depicts simulations of such a superposition with the unresolved line source in either emission or absorption superimposed onto a blackbody emission continuum as resolved by the PDPFTS.

While the majority of the experiment operated under vacuum, transmission of radiation through a short atmospheric path could not be avoided due to the fact that the photomixer could not be operated under vacuum. Absorption features were incorporated into the simulations to account for a short path through atmosphere by taking the product of the Gaussian profile and a normalized absorption simulation using the Blue Sky Spectroscopy Transmis-

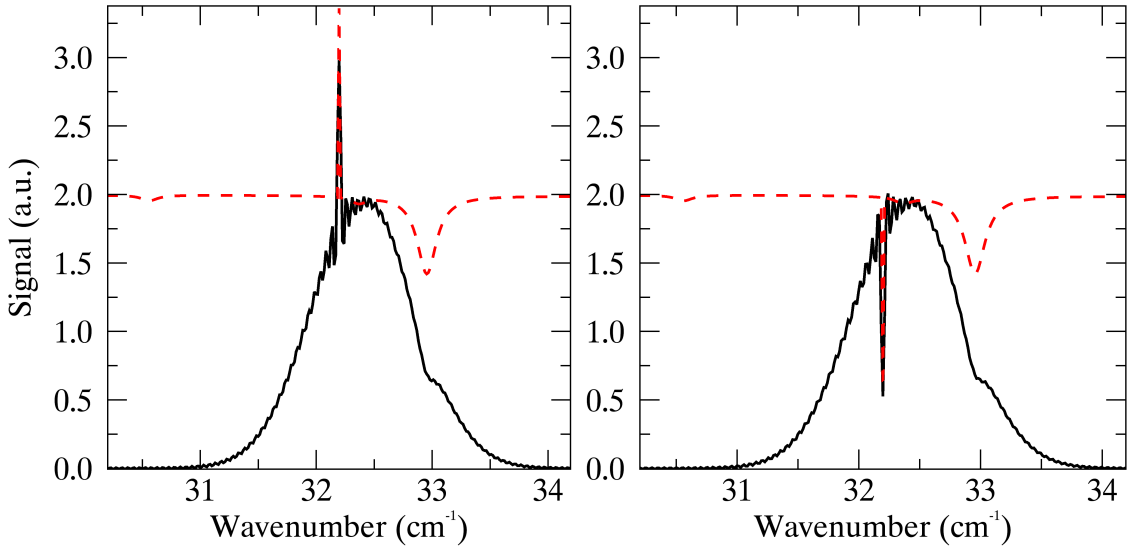

Figure 4.3: PDPFTS simulations including an unresolved line source and blackbody continuum profiles with atmospheric absorption. The simulation incorporates models based on radiative transfer through 0.3 m of atmosphere and a relative humidity of 10%. The total signal ignoring the bandpass of the grating is shown in red.

sion and Atmospheric Model (BTRAM) [29]. BTRAM was used to model the radiative transfer through 0.3 m of atmosphere, which was approximately the path length of the coupling between the source module, cFTS, and Test Facility Cryostat (TFC). Values for the relative humidity were set between 10% and 15% based on measurements of the laboratory.

Simulated PDPFTS spectra including both the grating and line profiles with atmospheric absorption is shown in Figure 4.3. The photomixer line is seen to be unresolved, whereas the atmospheric line is broadened by atmospheric pressure. The atmospheric absorption feature centred at approximately 32.95 cm^{-1} corresponds to transitions in the rotational energy level of the isotopologue $H_2^{16}O$ [105]. A spectrum such as this is verified in Chapter 5.

4.2.2 Linear Phase and Noise

Linear Phase

The simulations detailed above provide theoretical results which may be compared with experimental data obtained from a PDPFTS. In order to test the capabilities of extracting phase error from experimental spectra, linear phase errors were introduced into the system.

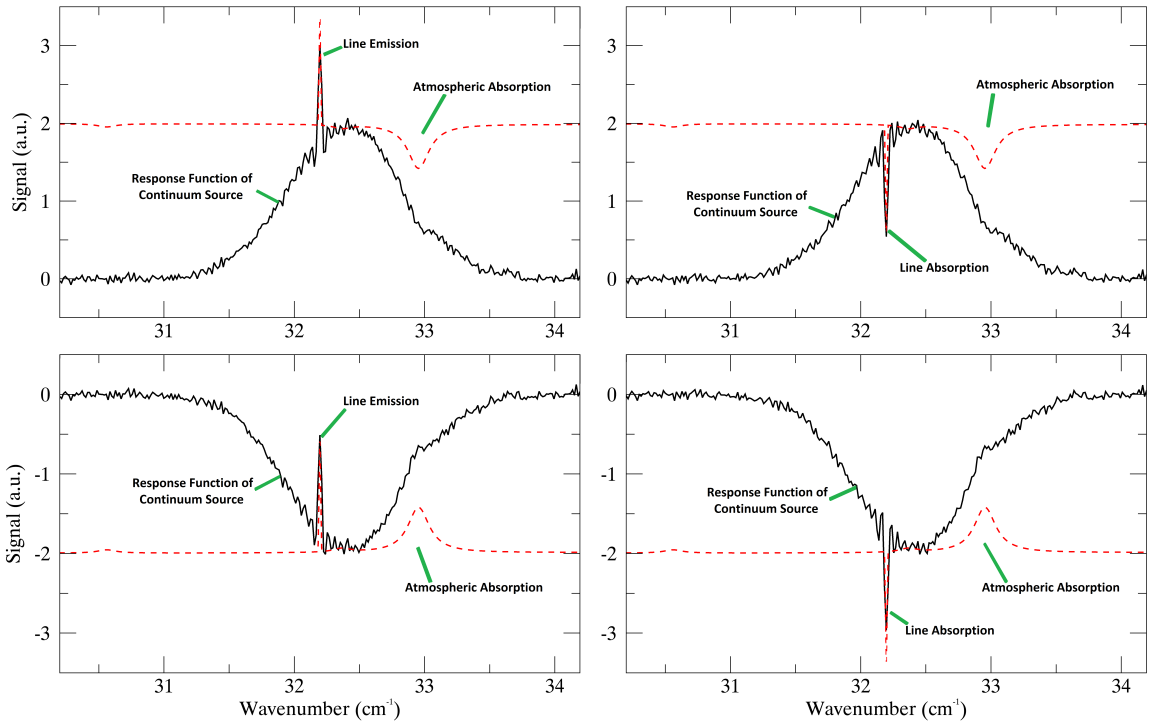

Figure 4.4: Simulated PDPFTS spectra of an unresolved emission/absorption line superimposed on an emission/absorption continuum incorporating atmospheric absorption. Panels a) and b) depict an emission continuum, while panels c) and d) depict an absorption continuum. Similarly, the unresolved line is in emission for panels a) and c), and absorption for panels b) and d). The total signal ignoring the bandpass of the grating is shown in red. These simulations include an SNR of $\sim$50 at the peak of the response function.

Due to the band-limiting nature of the grating module, the amount of relevant phase information available is also reduced. However, Equation 2.42 shows that the slope of the phase across the band will be relatively low depending upon the location of the band relative to the Nyquist frequency. Using these facts, the phase correction procedure was developed from techniques used in processing the simulations.

With the base spectrum calculated, linear phase error was incorporated into the simulated spectrum by introducing a phase via Equation 2.36. Preliminary results from the simulations showed that a phase error could be extracted separately for each interferogram so long as the phase was slowly varying. As shown in Equation 2.42, the maximum slope of the phase across the band can be reduced by increasing the Nyquist frequency (oversampling). Consequently, the methodology used to phase correct the simulated interferograms

should also be applicable for the experimental data. However, as will be shown in Chapter 5, the initial method of phase correction was flawed, and a new approach was needed.

Noise

Inclusion of noise allowed for the exploration of the SNR across multiple measurements and determine what signal could be reasonably processed. The noise for the simulations were based on two assumptions: first, the band under examination was unaffected by 1/f noise, and second, the system was free of any external noise, such as that from mains power or stray thermal radiation. The first assumption is reasonable since the band explored lies between 20 cm^{-1} and 33 cm^{-1}. The second assumption is based on the findings of Anderson [28] and the calibration of the diffraction grating. Consequently, only white noise was introduced into the simulated interferograms (see Figure 4.4).

Based on preliminary experimental measurements and the calibration of the grating assembly, the SNR of the PDPFTS was estimated to be $\sim$50 for a continuum emission produced by a blackbody [28]. Parseval's theorem was applied to determine the magnitude of the noise in the interferograms. This theorem, referenced in Equation 2.4, refers to the unitary property of the Fourier transform and essentially serves as a conservation law [47].

Through Parseval's theorem the magnitude of the noise in the interferogram is proportional to the magnitude of the noise in the spectrum. To determine the magnitude of the simulated noise, the total energy of the grating profile was calculated from the simulated spectrum. A scaling factor was then applied to the energy based on the desired SNR. This product represented the total energy of the white noise which was then applied to the interferogram to reproduce realistic data. For example, a scaling factor of 2% would be applied to the energy when the SNR is 50.

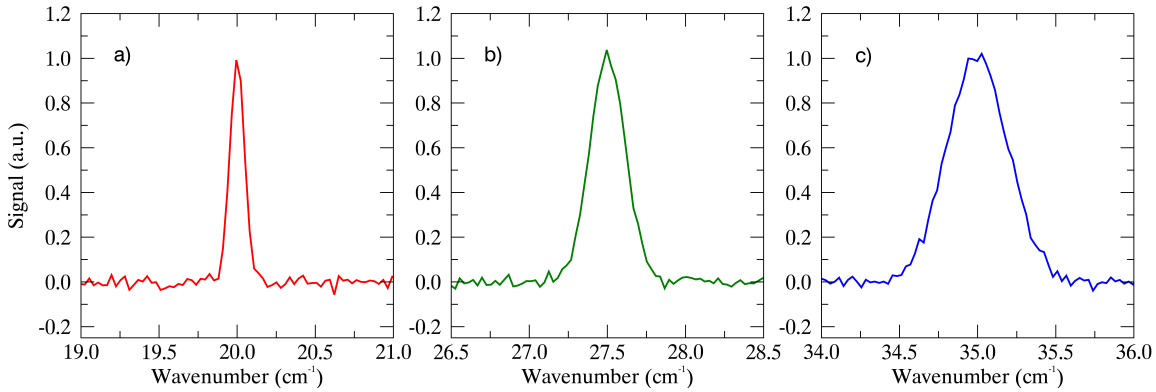

Figure 4.5: Simulated continuum spectra depicting the expected grating profile across the available band of the PDPFTS. The grating is centred at 20 cm^{-1}, 27.5 cm^{-1}, and 35 cm^{-1} in panels a), b), and c) respectively. For consistency, the amplitude of the source is kept constant. These simulations include noise with a SNR of $\sim$50 relative to the peak of the continuum.

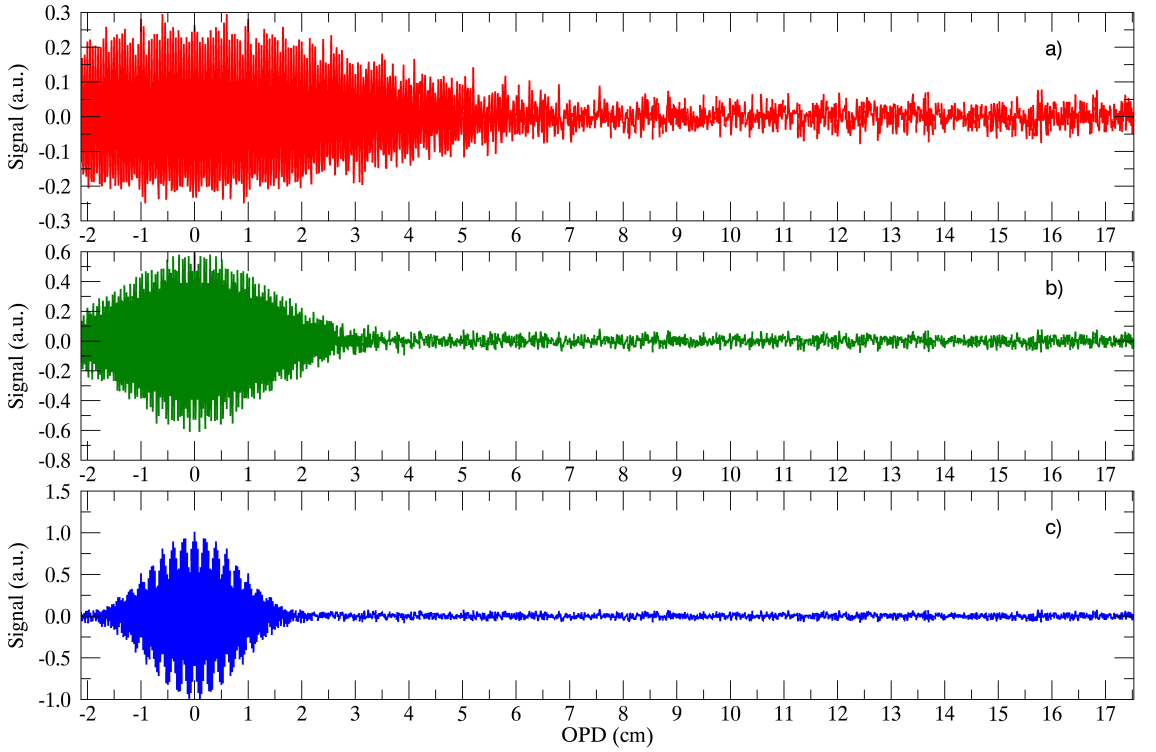

Figure 4.6: Simulated interferograms depicting the expected source coherence across the available band of the PDPFTS. The grating is centered at 20 cm^{-1}, 27.5 cm^{-1}, and 35 cm^{-1} in panels a), b), and c) respectively.

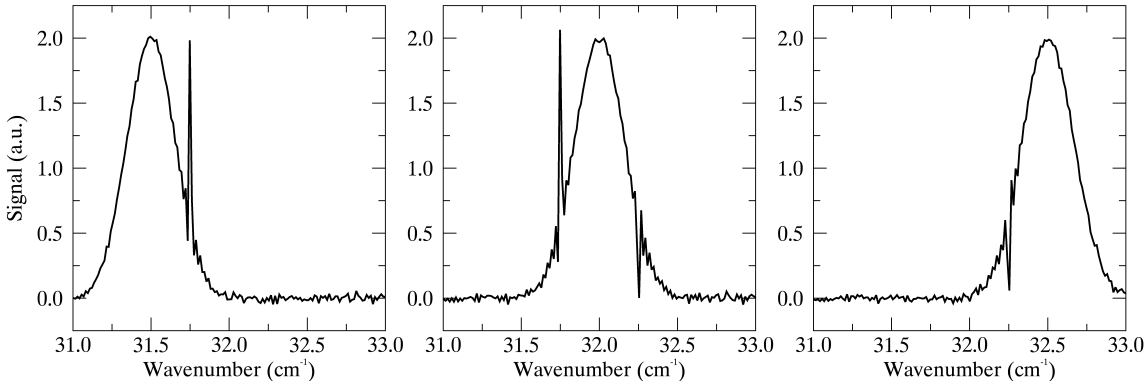

Figure 4.7: Simulated PDPFTS scan across three angles of two lines, one in emission (31.75 cm^{-1}) and one in absorption (32.25 cm^{-1}), superimposed on a blackbody emission continuum. It is clear that scans should be spaced no more than the equivalent of one FWHM centre-to-centre to eliminate the possibility of missing weaker unresolved lines.

4.3 Scan Simulation

In preparation for the processing and verification of the prototype PDPFTS, simulations were performed for series of FTS scans with the grating assuming different angular positions. The results from these simulations formed the basis for the development and testing of the data processing pipeline and a metadata collection system used to analyse the experimental data. This section explores the simulations of the scans as well as the predicted characteristics of PDPFTS data.

The PDPFTS was designed such that the cryogenic grating module is stepped between continuous scans performed by the cFTS, with each step representing a different passband for the PDPFTS system. As mentioned above, the resolving power of the grating module decreases with wavenumber. This fact can be observed in the width of the grating profile across the band as shown in Figure 4.5, and in the coherence length of the interferograms shown in Figure 4.6.

In this hybrid instrument, it is important to carefully choose the resolution of the FTS as well as the passband of the grating. If the passband is too narrow, there is insufficient data for phase correction, while if the passband is too wide, too much light passes through, increasing the photon noise. Likewise, in the case of a narrow passband, it is entirely

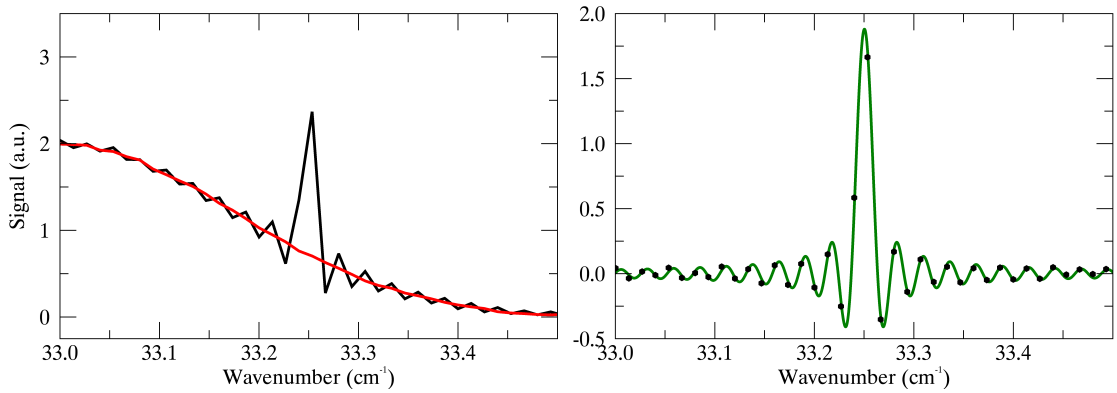

Figure 4.8: Analysis of an unresolved line source from a simulated PDPFTS spectrum. Left: A PDPFTS simulation of a blackbody continuum (red) onto which has been superimposed an unresolved line (black). Right: The difference between the two simulated spectra (black symbols) and the predicted line profile fit (green). This simulation includes an SNR of ∼55 at the peak of the response function.

possible to miss an unresolved line source. An example is given in Figure 4.7 where two line sources, one in absorption and one in emission, can be easily missed by the grating module. As a rule of thumb, the ratio of the resolving power of the FTS over the grating module should be roughly a factor of 10 while keeping in mind the resolution of the grating module changes even over a relatively small range of wavenumbers.

4.3.1 Simulating the Instrumental Line Shape

With the scans simulated, the data were analysed to compare the predicted instrumental line shape (ILS) of the PDPFTS system. The analysis was performed by removing the blackbody emission profile via a simulated background scan to isolate the unresolved line source. By extracting the line, it was shown that it exhibited the characteristic *sinc* function, as shown in Figure 4.8. Even with noise introduced in the simulations, the results reproduced the expected FWHM for the *sinc* function from the resolution of the cFTS. Thus, the simulation confirms that the post-dispersing element of the PDPFTS attenuates the signal by virtue of where it falls within the passband without any impact to the ILS of the cFTS. The manner of the attenuation is known such that with a calibration product the line position, amplitude, and FWHM can be restored with integrity.

4.4 Designing a Processing Pipeline

The PDPFTS is a complex system rivalled only by the complexity of the instrumental test suite (see Figure 3.15). In order to efficiently prepare and sort the data, a processing pipeline was developed to sort the extensive metadata of the PDPFTS and accompanying test equipment. The metadata was defined in two groups, Level-0 and Level-1, as shown in Figure 4.1. Level-0 metadata is collected directly from the instrumental suite - the analogue of housekeeping data for a space observatory, while the Level-1 metadata is derived from the first level of processing. The Level-1 metadata is divided further into the instrumental configuration (characteristics of the setup derived from the level-0 metadata), and the derived metrics (the instrumental configuration to determine the parameters for sorting and triaging the results).

The structure of the processing pipeline and derivation of Level-1 metadata that are used to assess data quality lends itself well to future implementation of machine learning and artificial intelligence techniques, especially given the immense volume of data expected from a PDPFTS. It is worth reiterating that the PDPFTS used in this thesis uses one detector and has a data rate of $\sim$48 kB/min; however, if an array of detectors is used, such as proposed for the SPICA SAFARI instrument, the data rate could have a thousand fold increase ($\sim$48 MB/min) or more. Additionally, each detector in the array requires its own calibration product. An automated system could ensure that the results represent the best possible data based on a series of metrics. These metrics may be user-defined, but the concept of a machine redefining the metrics of typical results is appealing for efficiently assessing the experimental data. A system could be configured where a machine can identify patterns and make decisions, such as how to process fair data such that they may be flagged as good, and identifying issues that may have resulted in poor data. An example is the development of a system to deglitch data subject to cosmic rays. However, the design and application of machine learning in the processing pipeline is beyond my present skill set and represents future work within the AIG.

Considerations in the pipeline design are subcategorized into *phase correction*, *derived metrics*, *error and noise analysis*, and *triage*. Data which has been categorized as good or fair are passed through the pipeline, and at the users discretion poor data may also be passed through for the purpose of troubleshooting. The phase correction process used throughout this work is based on the procedure outlined in Chapter 2, though modifications were made to the system as will be shown in Chapter 5. Similarly, the derived metrics, with the exception of the noise parameters, are calculated based on the equations governing grating theory given in Chapter 3.

4.4.1 Phase Correction

The preliminary simulations incorporated a linear phase typical of missampling ZPD. The amount of double-sidedness was selected such that the number of points in the band was sufficient to measure a linear phase, which requires careful consideration of the resolution of both the FTS and grating module. Recall from Chapter 2 that a linear fit to the phase requires at least two data points in the band. The phase can then be readily extracted from a given spectrum. Once the phase is determined, the Forman method can be applied to the interferogram as outlined in Section 2.6.4. Given the relative ease of determining the phase in the simulations, the pipeline was designed to find the phase, correct the interferograms, and average the corresponding spectra.

The conclusion from the simulations was that the initial pipeline proved to readily reproduce the simulated spectra. However, as will be shown in Chapter 5, in practice, determining the phase proved to be more challenging.

4.4.2 Noise Analysis

With copious amounts of data being generated by numerous PDPFTS tests, a means of assessing data quality was necessary. In its most general sense this incorporates the derived metrics, which inform the experimental setup during the scan. As part of the derived metrics, rudimentary noise measurements were included in the triage system as part of the

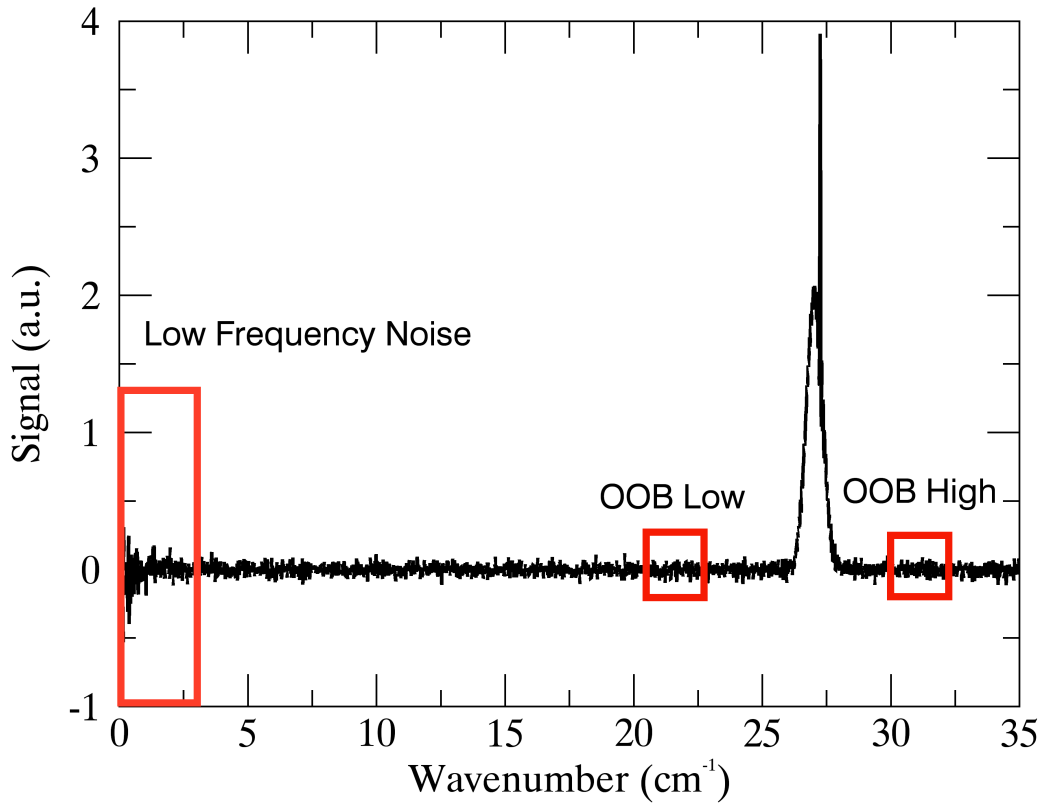

Figure 4.9: Derived noise metrics outlining the out-of-band (OOB) and low frequency noise bands on a PDPFTS spectrum. The OOB regions are defined relative to the peak of the grating profile and are located above and below the centre at a distance of three times the FWHM of the profile.

metrics used to categorize the quality of the data (see Figure 4.1).

The parameters of the signal noise used throughout this work are the out-of-band (OOB) noise at wavenumbers greater (high) and less than (low) the Gaussian centre, as well as the low frequency noise chosen to be from 0 - 3 cm^{-1} which corresponds to a range of 0 - 1.8 Hz given the translating stage's velocity of 0.6 cm/s. The OOB noise is determined from the standard deviation of a band with a bandpass equal the the FWHM of the Gaussian profile. The centre of the OOB regions were chosen after inspection of a series of good, fair, and poor scans to be located at a wavenumber three times the FWHM above and below the centre of the Gaussian for the high and low band, respectively. These positions were

chosen such that there was no overlap between the inband signal and the OOB regions. These noise parameters are used to identify the SNR at the peak of the profile by taking the ratio of the peak amplitude over the average of the OOB noise signals.

I defined the low frequency noise to be the sum of the absolute value of the spectrum in the 0 - 3 cm^{-1} range, which at the nominal OPD velocity of the translating stage covers a frequency range of 0 - 1.8 Hz. The low frequency noise parameter identifies issues with $1/f$ noise in a scan and serves as an indicator of flicker and source noise in the system, as well as environmental noise such as the pulse tube coolers of the TFC, which pulse at a frequency of $\sim$1 Hz. A graphical description of the low frequency noise, as well as the high and low OOB noise bands is given in Figure 4.9.

The inclusion of noise analysis in the pipeline serves to flag particularly noisy scans in the PDPFTS data. Flagging of noisy data is important as scans are taken as a series and then averaged to reduce the noise. By eliminating excessively noisy interferograms, such as those subject to external vibrations or cosmic rays, the resulting average represents the best possible SNR.

4.4.3 Triage

Once the data have been processed, the results must be presented in a legible and convenient method for ease of analysis. The present method incorporates a flat file database for each series of tests presenting the derived metrics and noise analysis. The database allows for the results to be readily distributed and interpreted. However, the simplicity of such a database does not allow for flexibility should values need to be changed.

An upgraded triage system based on an XML database is proposed, most likely based on a SQL server since it is compatible with the IDL language and legacy code. Although more overhead programming is required, the advantages of a flexible system that can be updated and kept secure outweigh these costs. XML files also suffer from a complex updating procedure as a file must be read, stored into memory, updated, and rewritten into the

database.

Since XML databases are common, many products exist that can interpret XML files. The availability of such products allows for results to be easily accessible to collaborators without relying on specially designed code. However, the main advantage of XML databases is the ability to quickly sort and access results based on the metadata, allowing for a database which is far easier to query and examine metadata compared to the flat file database [106]. Thus, the PDPFTS results may be quickly analysed, triaged, and exported globally using a wide array of products.

4.5 Conclusions

Chapter 4 described the process of simulating PDPFTS data and the resulting processing pipeline. Section 4.2 outlined the considerations taken in producing accurate simulations. The simulations are expanded in Section 4.3 to reproduce scanning sequences representative of how the PDPFTS is utilized. These simulations confirm that the ILS of the cFTS is conserved when combined with the dispersion system. Based on these simulations, the groundwork for a data analysis pipeline was designed for metadata collection and retrieval (Section 4.4).

The simulations shown above have been used to inform the design of a processing pipeline and address the challenges of analysing data from a PDPFTS. The simulator produced theoretical spectra to provide a comparison for experimental results. These simulated spectra are compared and contrasted with results from a novel FIR hybrid PDPFTS prototype in Chapter 5.

Chapter 5

Experimental Results from a PDPFTS

But lo! What light thru yonder window breaks?

Romeo in Romeo and Juliet

WILLIAM SHAKESPEARE

5.1 Introduction

This chapter presents experimental results from a far-infrared (FIR) post-dispersed polarising Fourier transform spectrometer (PDPFTS) consisting of an evacuated, room temperature Fourier transform spectrometer (FTS) and a grating spectrometer operating at 4 K. This is a first step to a fully cryogenic PDPFTS demonstrator. A technique to derive phase error for phase correction in a PDPFTS is explored. Astronomical spectra are simulated using a novel calibration source module combining line emission from tunable THz photomixer sources with continuum emission from a variable blackbody source. The results from the PDPFTS prototype are compared with the theoretical simulations presented in Chapter 4. Through these simulations we are able to explore the challenges and sensitivity of this novel instrument. Additionally, the narrow band afforded by the grating allows intentional aliasing to be studied. Results from the prototype PDPFTS show excellent agreement with theory.

Tests were performed with both the Test Facility Cryostat (TFC) and calibration FTS (cFTS) under vacuum. The two systems were connected via an evacuated bellows. Radiation from the tunable photomixer and blackbody sources were transmitted through only a

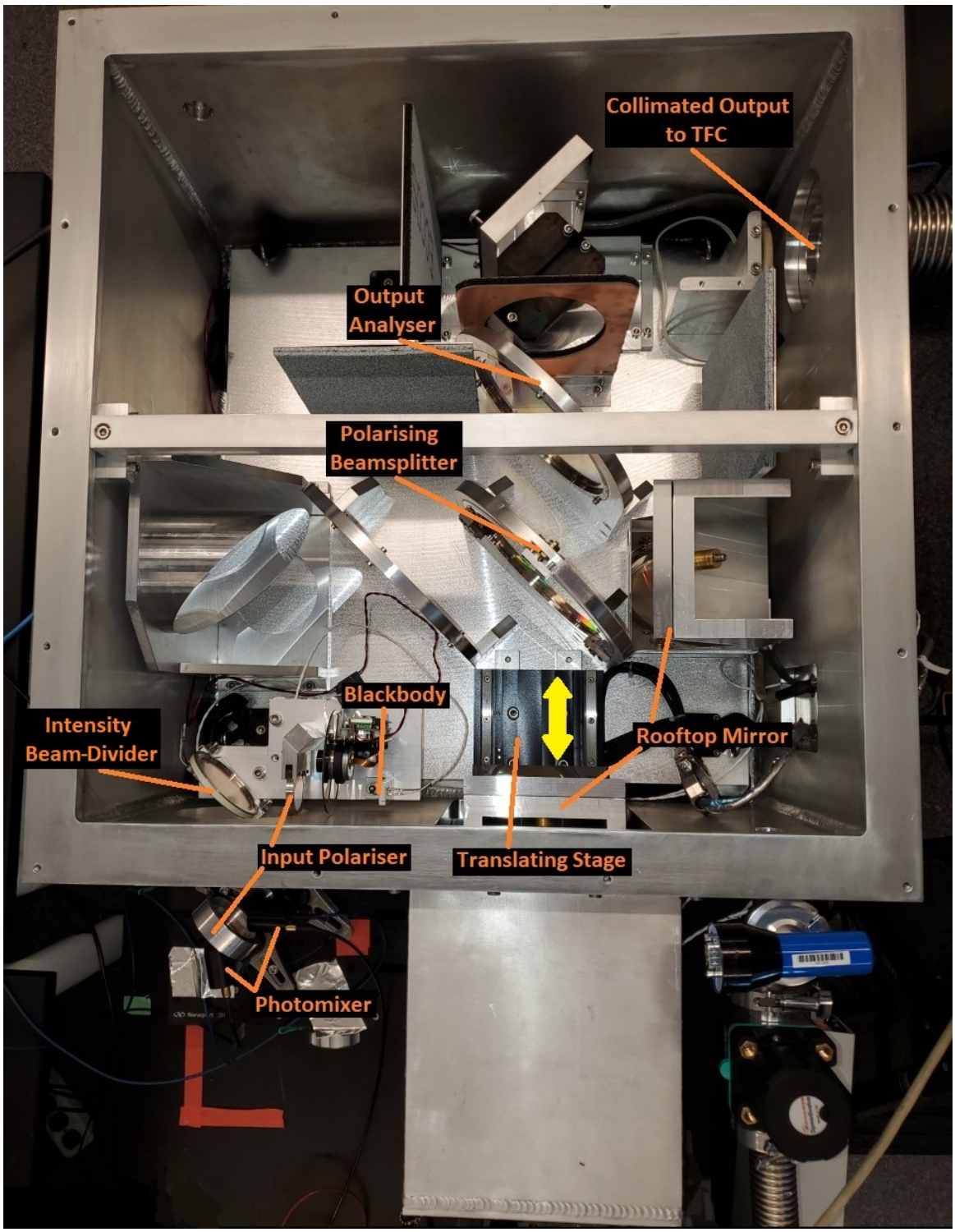

Figure 5.1: Configuration of the source module and calibration FTS (cFTS). In order to accommodate a second polariser, the blackbody was integrated into the body of the cFTS. The two halves of the source module were combined using a dielectric beamsplitter.

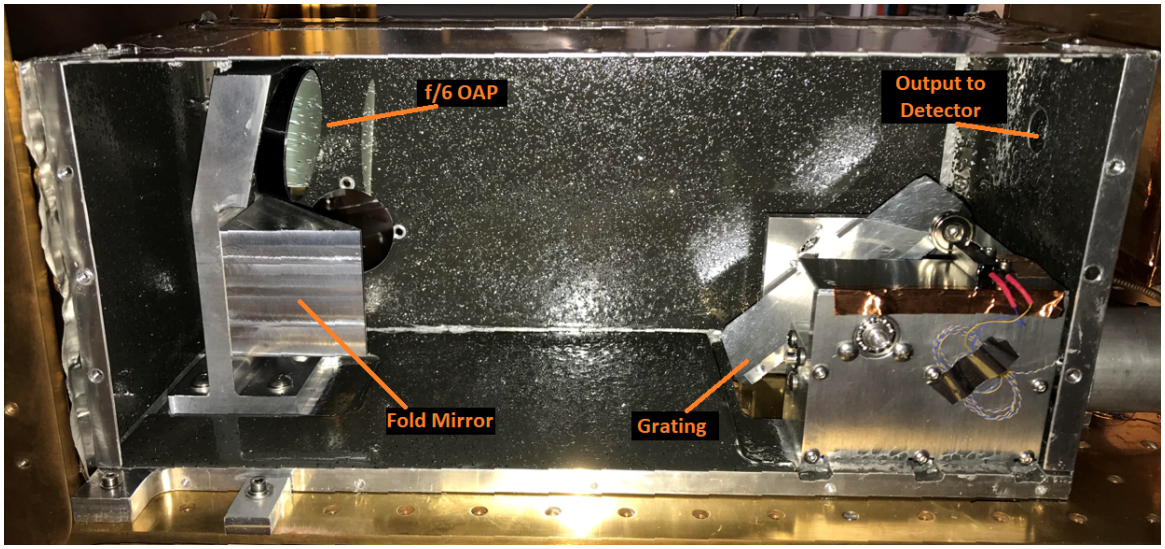

Figure 5.2: Cryogenic grating spectrometer mounted in the Test Facility Cryostat (TFC). The housing and optical configuration were designed by Veenendaal [87], and the grating was designed by Anderson [28].

short path of atmosphere (∼10 cm) into the cFTS (Figure 5.1). Modifications to the input of the cFTS were made in order to integrate the second photomixer (see Section 5.4.1). Light incident from the cFTS enters the cryogenic grating spectrometer housed within the TFC (Figure 5.2), which then diffracts a selectable passband of light that is collected by the off-axis parabola (OAP) mirror and focused onto the bolometer.

PDPFTS observations were made by obtaining interferograms using the cFTS. The passband of the system was adjusted by incrementally rotating the grating spectrometer between each series of scans to select a new narrow spectral band. Thus, a complete scan of the spectral range of the PDPFTS requires a series of scans obtained by the cFTS for each angle of the grating spectrometer. The experimental test equipment allowed for the laboratory conditions, source module, detector state and temperature, and the cFTS to be monitored during each scan. Metadata were collected before and after each scan and the average of these two measurements was recorded.

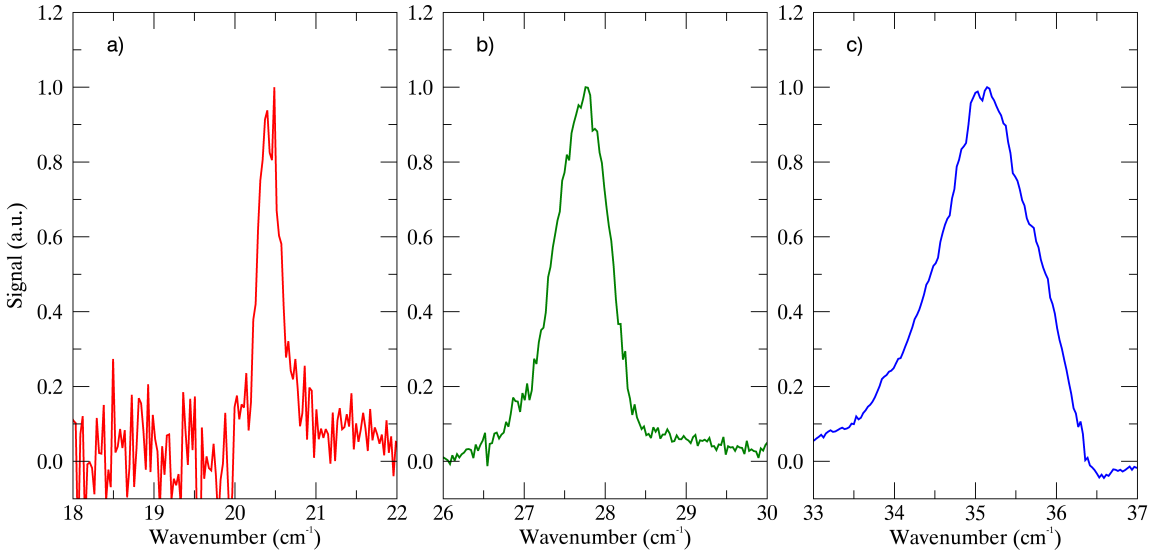

Figure 5.3: Normalized continuum spectra depicting the width of the grating profile across the available band of the PDPFTS. In these examples the grating is centred at 20.4 cm^{-1}, 27.8 cm^{-1}, and 35.1 cm^{-1} in panels a), b), and c) respectively. Compare with Figure 4.5

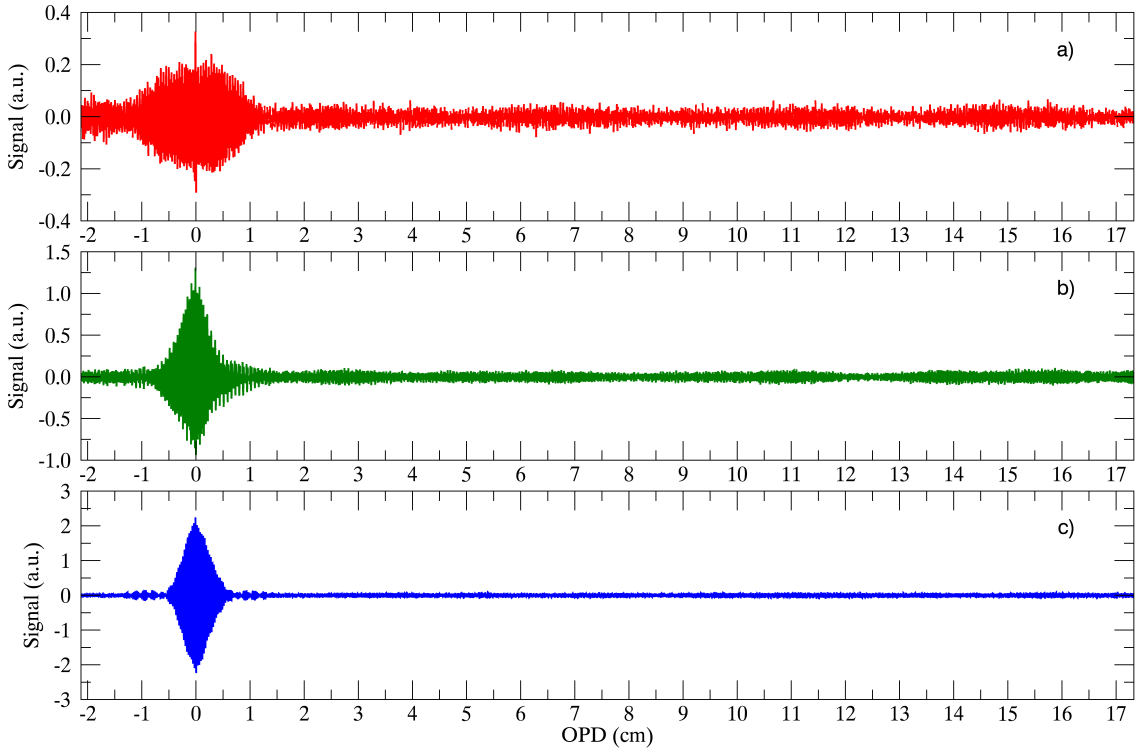

Figure 5.4: Interferograms depicting the change in the effective coherence length across the available band of the PDPFTS. In these examples the grating is centred at 20.4 cm^{-1}, 27.8 cm^{-1}, and 35.1 cm^{-1} in panels a), b), and c) respectively. Compare with Figure 4.6

5.2 Integration of the Grating Spectrometer

Characterisation of the cryogenic grating spectrometer was performed by Anderson as a prelude to its integration into the PDPFTS [28]. The cryogenic grating spectrometer serves as the post-dispersing element of the PDPFTS, defining the adjustable passband of the system. Initial tests were performed to confirm that the grating spectrometer worked as a post-dispersive system by measuring the bandpass of the system as a function of the wavenumber. These tests were performed using the blackbody source and stepping the grating across the spectral band of the PDPFTS to generate a series of spectra from which the bandpass was determined. From these results, it was observed that loading on the cryogenic bolometer were far greater than expected. Since excess thermal energy introduced into the bolometer increases its noise-equivalent power (NEP), this issue had to be addressed [54].

Preliminary tests explored the spectral response of the PDPFTS using a blackbody emission continuum. As shown in Figure 5.3 and the simulations in Figure 4.5, the passband of the PDPFTS increases with wavenumber. Each of the bands in Figure 5.3 were normalized to allow easy comparison of the width of the Gaussian profiles; the significant difference in signal strength across the band is highlighted in Figure 5.4. The shift in signal strength arises from the σ^2 dependence of the spectral radiance of the blackbody at low frequencies and the changing bandpass of the grating as a function of angle. While the first observations show a significant difference between the expected resolution of the grating module and the simulations, these were traced to a suboptimal entrance slit and subsequently corrected. With this correction, the observed passband more closely matched the expected resolving power across the band, confirming the results of Anderson [107].

While the observed passband of the grating matched those obtained by Anderson, the increased radiant loading on the detector persisted despite the refinement of the grating module's resolution. Exploration across the band revealed that the second order of the grating module was able to enter the observable band of the PDPFTS while scanning bands at lower wavenumbers, as shown in Figure 5.5. Recall from Figure 3.9 and Equation 3.7

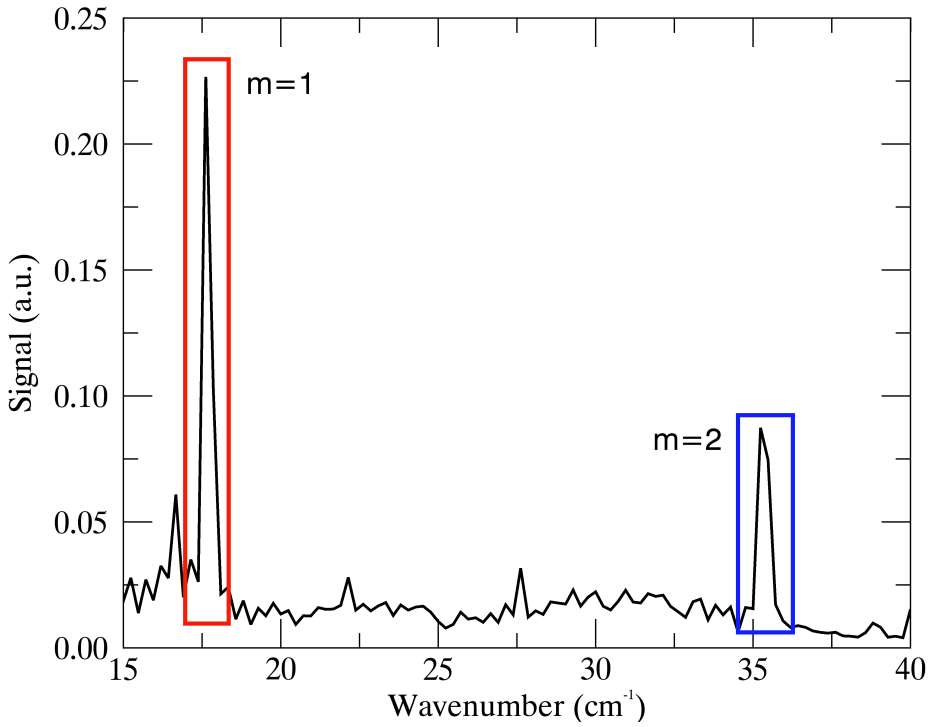

Figure 5.5: Two observed orders measured in a single scan using the PDPFTS. The second order (m=2) corresponds to twice the wavenumber or half the wavelength of the first order (m=1). Measuring multiple orders led to greater thermal loading in the detector.

that half the wavelength (twice the wavenumber) is diffracted at the same grating angle, which is why grating spectrometers required order sorting. The discovery and diagnosis of the observable second order was only possible through the use of the cFTS, as a grating spectrometer is unable to differentiate between orders. The problem was traced to the final filter placed directly in front of the feedhorn, which was sufficiently broad to allow not only the first order but also a portion of the spectral range of the second order to be detected. Once the cause was identified, it was a simple matter to replace this low pass filter, after which the issue of the radiant loading was resolved.

5.3 Phase Correction

As discussed in Chapter 2, phase correction is an essential processing step necessary to maximize the value of PDPFTS data. From the simulations outlined in Chapter 4, it was

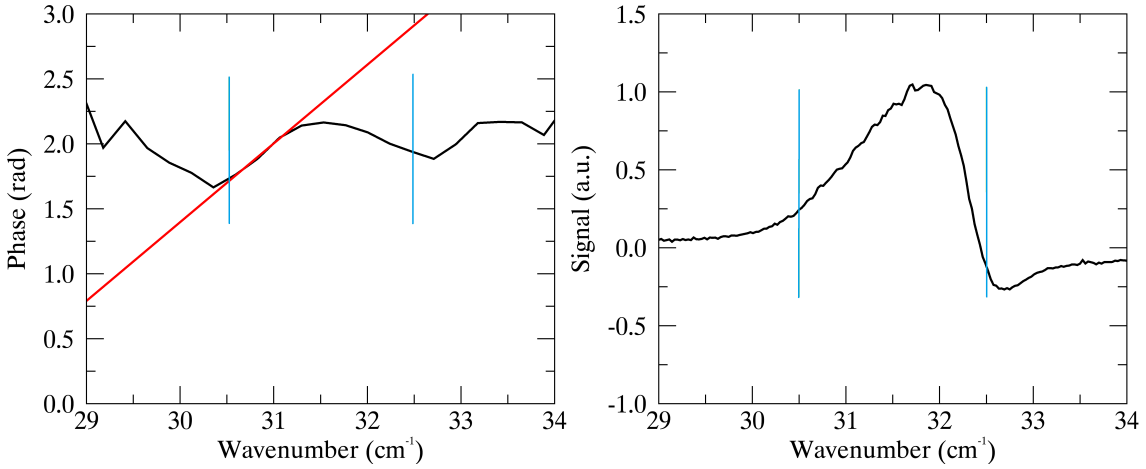

Figure 5.6: Problems determining phase error in the narrow band of the PDPFTS. The blue lines indicate the edges of the passband defined by the grating module. Left: A linear phase error (red) fit generated from weighting the phase based on the SNR. Right: An anomalous spectrum produced from phase correction using a bad fit.

found that the phase error for a single scan could be readily extracted for phase correction. However, preliminary results from the PDPFTS concluded that a simple linear fit could not be extracted due to both noise and the narrowness of the band. The analysis of this issue and the exploration of a technique to reliably extract a linear phase are described below.

5.3.1 Issues in Determining Phase Error

As outlined in Chapter 2, phase error is determined by examining the smaller double-sided portion of an interferogram. The correction is then applied to the single-sided portion of the interferogram. A linear phase is relatively simple to derive and correct, and only requires a small number (> 2) of points. However, white noise across the passband introduces random fluctuations in the measured phase, particularly when the signal-to-noise ratio (SNR) is relatively low. Thus, a phase fit is made easier and is more robust when a wide band with high SNR is used to derive the phase.

Due to the narrow passband of the PDPFTS, fewer points are available for determining the phase in a given measurement. Within the band of the PDPFTS, the grating module imposes further attenuation due to its Gaussian spectral response. Consequently, in the PDPFTS the number of datapoints available with peak SNR to determine the phase is re-

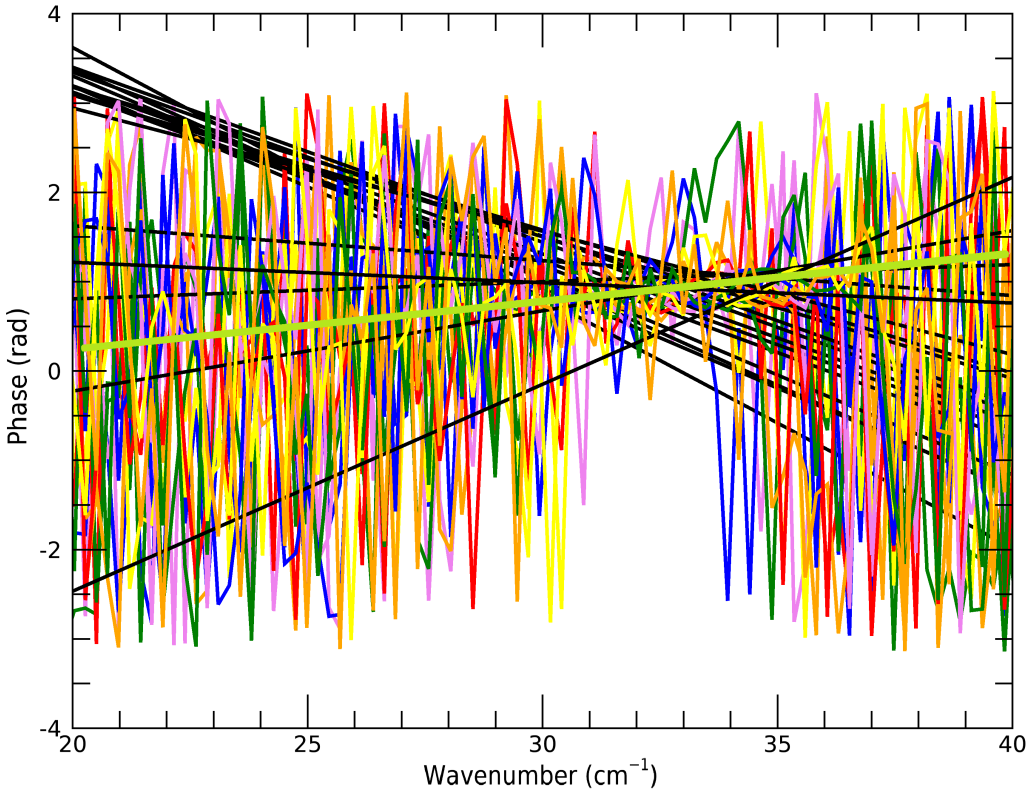

Figure 5.7: Phase error across multiple measurements (coloured lines) for a small range of the PDPFTS band. The expected linear phase is shown in lime green. Due to the combination of the narrowness of the band and noise, a consistent fit to the phase error (black lines) is difficult.

stricted, especially at low wavenumbers when the grating module is operating with the greatest resolving power and the cFTS is operating at its lowest. As shown in Figure 5.6, a linear phase can still be extracted, though using an improper fit introduces anomalies into the spectrum.

Figure 5.7 highlights the difficulty in determining phase: the measured phase across a series of scans can differ greatly. Each of the phases shown were calculated from a sequential series of scans taken across a small portion of the PDPFTS's spectral range. From examining the interferograms, it was found that the true position of zero path difference (ZPD) was shifted by $\sim$0.005 cm. The linear phase is defined as $\phi = 2\pi\sigma\alpha$, meaning the expected slope of the phase is approximately 0.0314 rad/cm^{-1}, which would correspond to a change in phase of 0.63 rad across the wavenumber range shown in Figure 5.7. By

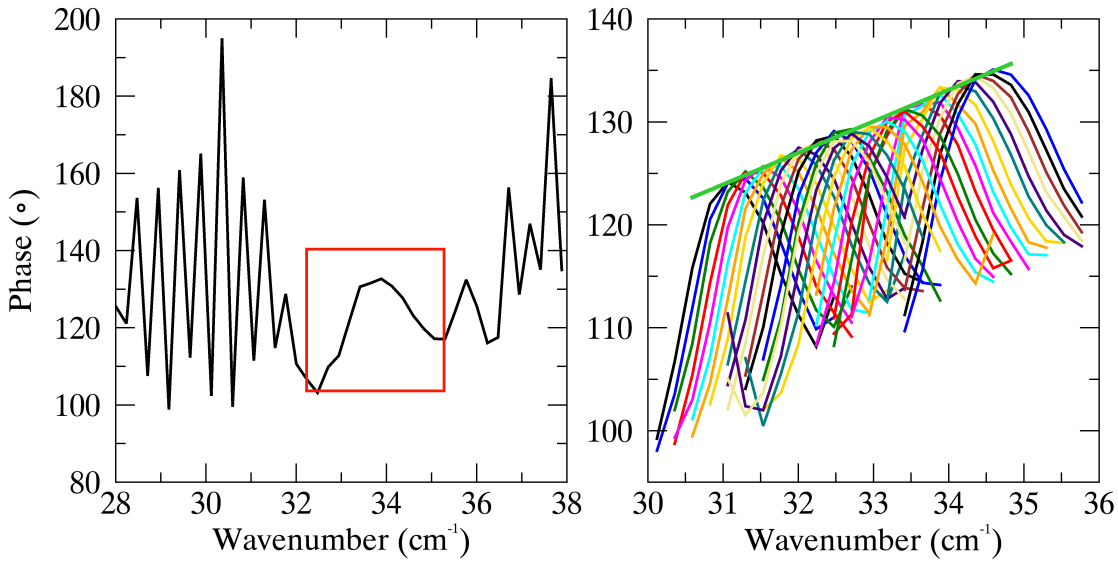

Figure 5.8: Determination of phase error in a PDPFTS. Left: Nonlinear phase response of a ∼1200 K blackbody measured by the PDPFTS (red). Note the narrowness of the band. Right: Phase response of a ∼1200 K blackbody across several scans of the post-dispersing element reveals a linear trend in the phase (green).

inspection, only a few of the measured values for the phase are near the expected value. This test demonstrates the fact that a reliable phase cannot be extracted from a single scan, meaning a new technique is required to find the phase.

5.3.2 Phase Correction Technique

The technique developed for extracting the phase for measurements obtained using a PDPFTS begins by exploring the phase of a single scan. As shown in Figures 5.6 and 5.8, one is tempted to assume that the measured phase is manifested as a Gaussian similar to the spectral response of the band. However, the true phase is weighted by the SNR, meaning the peak of the inband phase is nearest to the linear phase as it is the least impacted by the noise. By making multiple measurements across the spectral range of the PDPFTS, it was found that the peaks of each of the phase measurements presented a linear trend, as seen in Figure 5.8. The discovery of a linear trend in the peak of the phases was confirmed across multiple datasets. Preliminary studies indicate the phase can be recovered by combining individual spectra obtained from a series of grating scans.

Since a phase error is equivalent to an offset in the assumed ZPD and is thus common to all grating scans, it suggests a reliable means of determining a linear phase in the PDPFTS. The technique to phase correct data obtained by the PDPFTS is as follows. First, each of the measured interferograms across varying grating angles are compared in order to sort the scans by apparent ZPD, ensuring that the expected phases between each set of scans is similar. This step is possible due to the use of stable and repeatable position metrology on the translating stage of the cFTS. After the interferograms are sorted, each of the sorted sets are then averaged together before transformation. The resulting phase exhibits a wider band for extracting a fit while maintaining the observed linear trend. In essence, one is artificially generating an interferogram of a broadband source by averaging interferograms taken at different grating settings. The grating scans need not be contiguous for this method to work, but the more scans there are the better this method works. The extracted phase is then applied to each individual interferogram using the Forman method, as outlined in Chapter 2. These steps are repeated for each of the sorted sets of interferograms until all the data have been corrected. This novel technique to extract a dependable phase error allows for each narrow band spectrum to be reliably phase corrected.

5.4 Verification of the PDPFTS

5.4.1 Application

PDPFTS observations are made by first setting the grating angle, which sets the band-pass of the PDPFTS. Interferograms are then obtained at each grating angle using the cFTS. As described in Chapter 4, consideration must be given to the step size between scans. As an example, consider the measured spectra shown in Figure 5.9. In the red and blue spectra, the unresolved line appears as a weak signal, while in the green spectrum it dwarfs the blackbody continuum.

As shown in Figure 5.9, if the grating is stepped too largely then features can be missed. To avoid missing features, the scan procedure is broken into two steps. First, quick scans

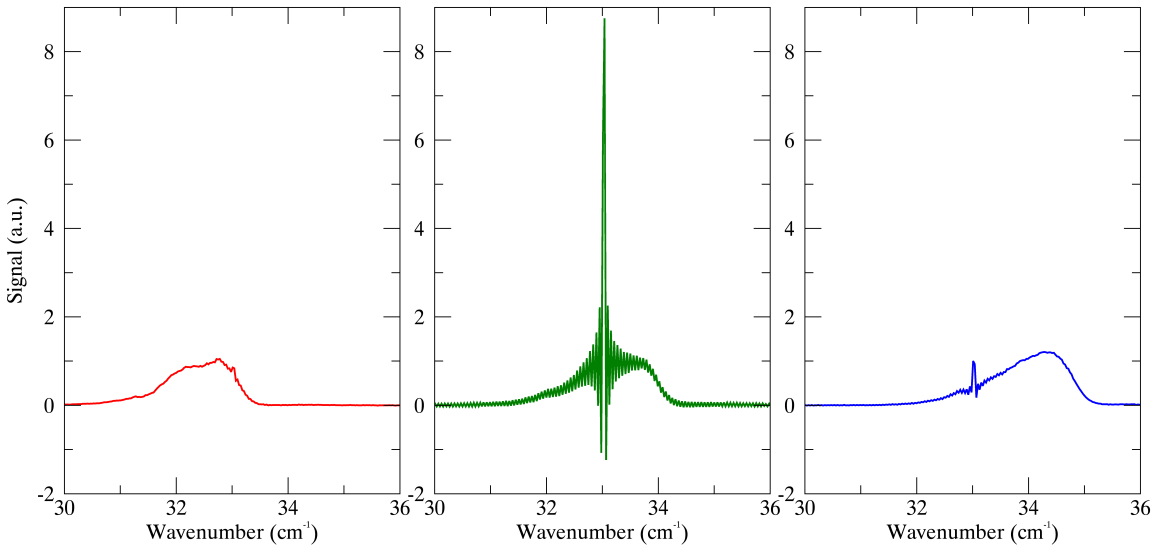

Figure 5.9: Demonstration of a series of scans observed using the PDPFTS measuring a blackbody continuum and photomixer line source. The photomixer line is held with fixed intensity at 33 cm^{-1}, and the grating is scanned across the position of the line with the centre of the profile at roughly 32.2 cm^{-1}, 33 cm^{-1}, and 34 cm^{-1} respectively for the panels from left to right. Observations were made by incrementally rotating the grating spectrometer and obtaining interferograms. The signal from the unresolved photomixer is visibly attenuated by the grating spectrometer.

are conducted to determine the position of any relevant features. Once found, a series of high-resolution scans are obtained while using the smallest change in angle of the grating for the given time constraints of the test. To avoid potential effects of hysteresis that could arise from the worm-wheel grating drive, the grating is rotated in one direction for a given series of scans.

A blackbody source was the first unit to be integrated into the source module, serving as a reference background for the system and defining the spectral response of the PDPFTS. Initial results were used to measure the resolution of the grating spectrometer and explore the requirements to reconstruct spectral features by stitching together individual grating profiles [91]. Early tests indicated a loss of resolution due to improper choice of entrance and exit slit sizes in the system, an issue which was promptly corrected. The absorption feature due to the transition of $H_2^{16}O$ at 32.95 cm^{-1} was used extensively as it provided a convenient means of calibrating the PDPFTS and has a relatively large absorptivity com-

pared to other features available to the PDPFTS [105]. As shown in Figure 5.10, with a relatively low resolution the absorption feature is easily observed.

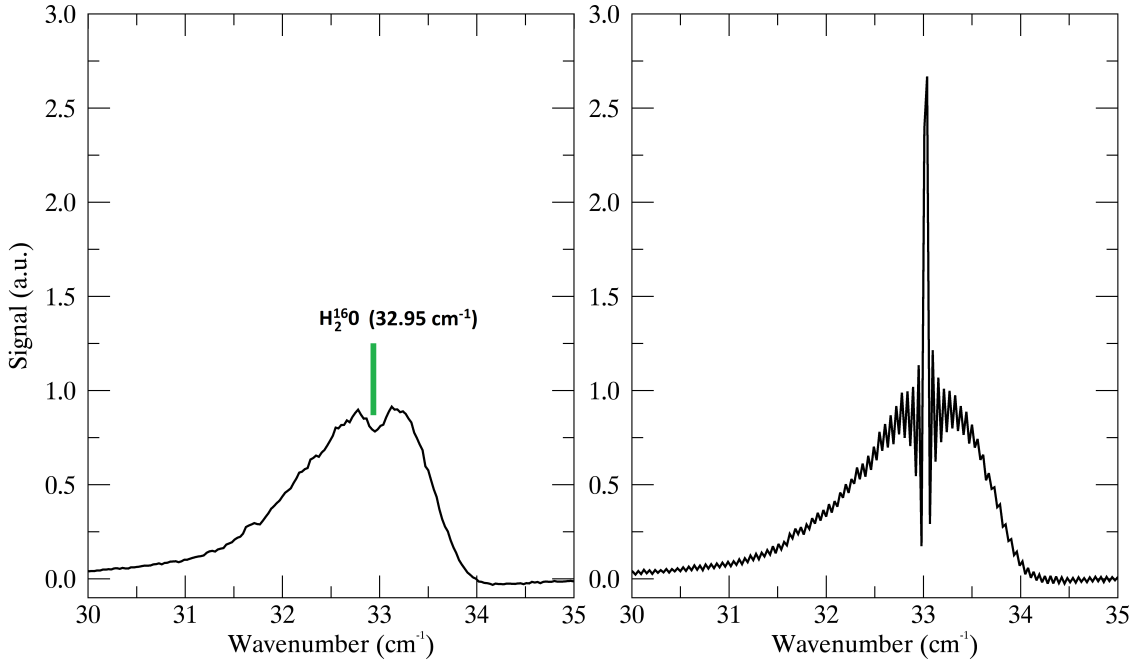

Figure 5.10: Results after integrating the first photomixer into the source module for the PDPFTS. Left: A continuum spectrum showing an absorption feature due to the transition of $H_2^{16}O$ at 32.95 cm^{-1} [105]. Right: An unresolved emission line at $\sim$33 cm^{-1} produced by a photomixer superimposed on the continuum spectrum.

The next series of tests added a tunable THz photomixer line source. The photomixer and blackbody sources were combined using an input polariser, shown previously in Figure 3.11. Since the output of the photomixer source is linearly polarised, care was taken to ensure the output polarisation was optimised to pass through the input polariser. In order to ensure both sources were observed in emission, as seen in Figure 5.10, radiation incident from the source module into the cFTS was encoded using a second input polariser. To observe a combination of emission and absorption features (Figure 5.12), the input polariser built into the cFTS was removed, allowing for the polariser in the source module to define the input ports. The inclusion of a photomixer in the source module allowed for the exploration of the post-dispersing element's impact on the instrumental line shape (ILS) of the FTS.

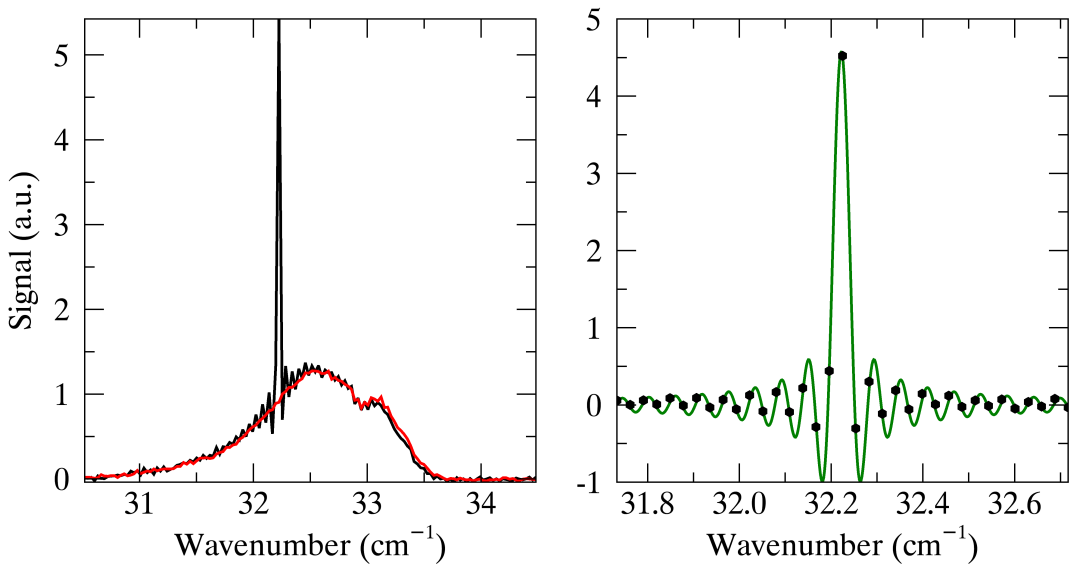

Figure 5.11: Analysis of an unresolved line source from a PDPFTS spectrum. Left: A blackbody emission continuum (red) with a superimposed unresolved line (black). Right: The difference between the two measured spectra (black symbols) and the predicted line profile fit (green) [108]. Compare with Figure 4.8.

The PDPFTS was used to measure an unresolved line superimposed on a continuum emission blackbody, an important step in evaluating the proof of concept of the instrument. Initially, the photomixer source was configured to produce a signal with a frequency in the range of 30 cm^{-1} to 35 cm^{-1}. The photomixer was then reconfigured using different lasers to produce a signal with a frequency in the range of 10 cm^{-1} to 22 cm^{-1}. These results showed that the photomixer line source achieved a signal 40 times greater than that of the blackbody, far overpowering the output of the blackbody source. This effect is due to the σ^2 dependence of the power of the blackbody and the σ^{-4} dependence of the photomixer; at the low wavenumber end of the spectrum the blackbody signal is its weakest, while the photomixer signal is its strongest.

Scans were taken of the source module both with and without the photomixer line. Figure 5.11 highlights that the measured spectra show excellent agreement at the continuum level despite being obtained on different days [108]. The residual of these spectra gives the spectrum of the line source whose profile agrees with the expected instrumen-

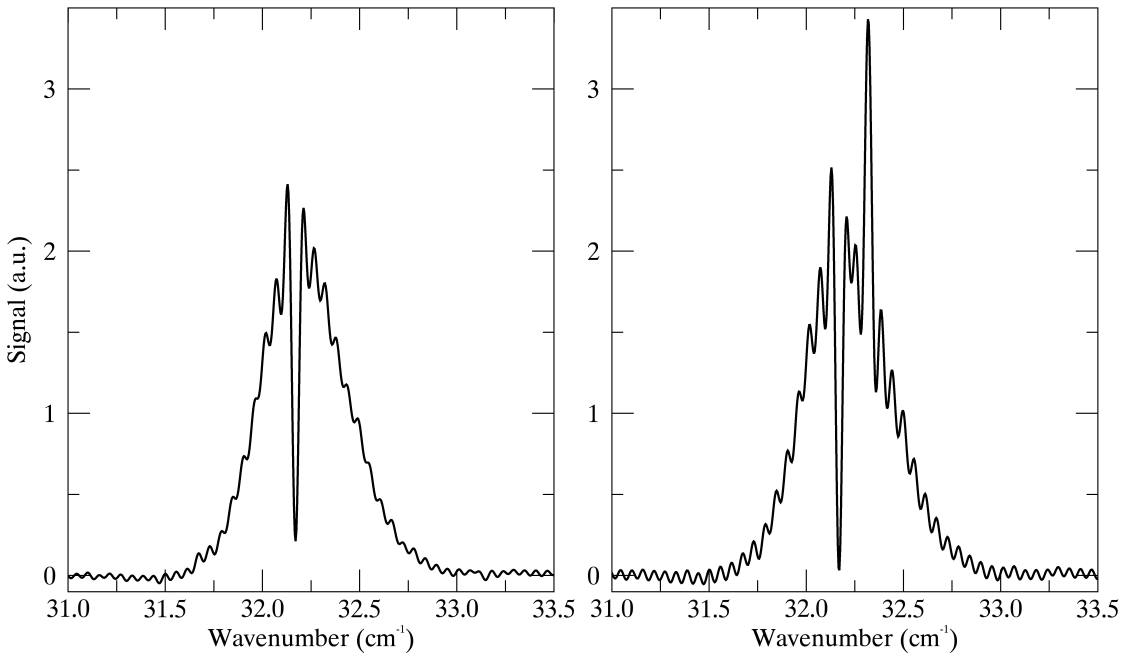

Figure 5.12: Results after integrating the second photomixer into the source module for the PDPFTS. Left: A continuum spectrum with a single unresolved absorption line. Right: Two unresolved lines, one in absorption and one in emission, superimposed on a continuum spectrum after integrating the second photomixer into the source module.

tal lineshape of an FTS. The experimental resolution of the line source was measured as 0.03491 ± 0.00005 cm^{-1} from the fit. This value agrees with the expected spectral resolution of 0.03491 cm^{-1} after truncation due to phase correction. Thus, these results confirm the prediction shown in Figure 4.8 that the post-dispersing element and the FTS are linear systems.

The final tests integrated a second photomixer into the source module. A method was derived to couple the existing source module with a second input. To maintain isolated polarisations, the third input was coupled to the previous source module using an intensity beam-divider [109], as shown in Figure 5.1. The third source was then mounted within the vacuum chamber of the cFTS and encoded via a separate input polariser. However, this configuration presents a problem: the current photomixers cannot be operated under vacuum. Therefore, depending on the desired test configuration, the cFTS at times was required to be operated in atmosphere. The new configuration allowed for the exploration

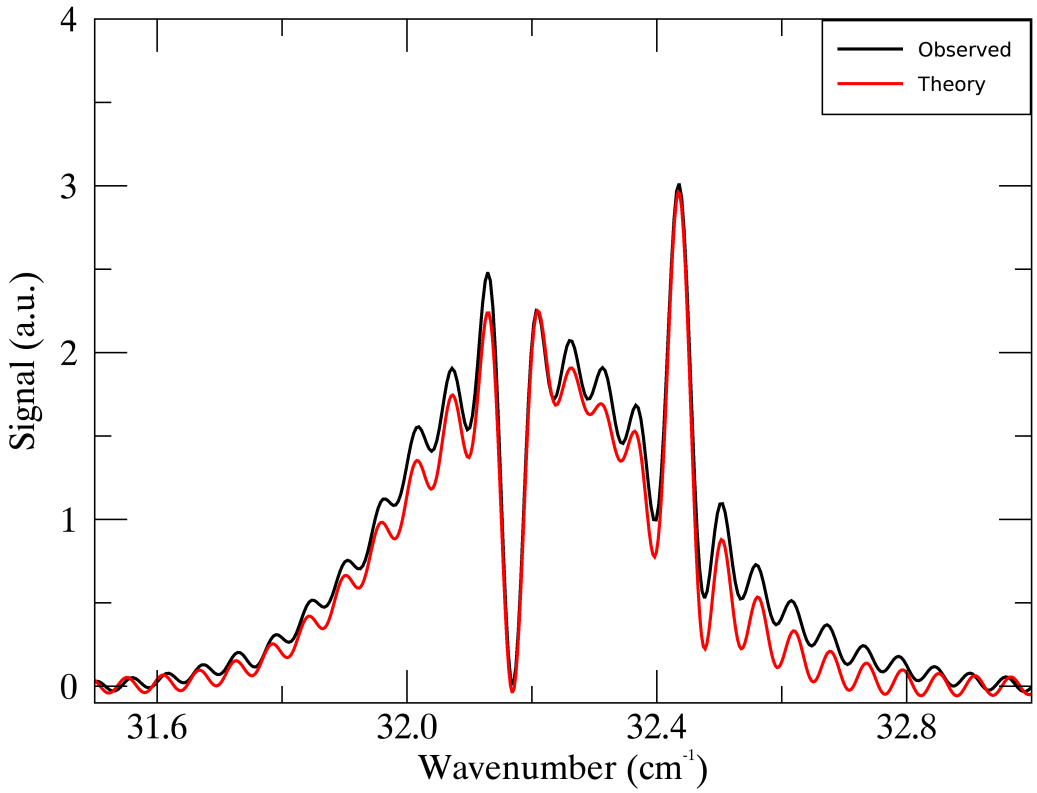

Figure 5.13: Measured PDPFTS spectrum of an unresolved emission and absorption line superimposed on a blackbody continuum (black) compared to a theoretical simulation of the PDPFTS spectrum (red) based on the measured grating spectrometer resolving power.

of multiple lines in either emission or absorption superimposed on a continuum, as shown in Figure 5.12. The expanded source module configuration will lead to the exploration and development of line extraction techniques.

The PDPFTS was used to measure two unresolved lines, one in emission and one in absorption, superimposed on a blackbody continuum. Figure 5.13 shows a comparison between simulated results (red) and observed spectra (black). The spectra show an absorption line at 32.170 $\pm$ 0.001 cm^{-1} and an emission line at 32.435 $\pm$ 0.001 cm^{-1} The discrepancy in amplitudes is attributed to atmospheric absorption in the system unaccounted for in the simulated results. Regardless, there is clearly excellent agreement between theory and experiment. As before, the ILS of the FTS is evident.

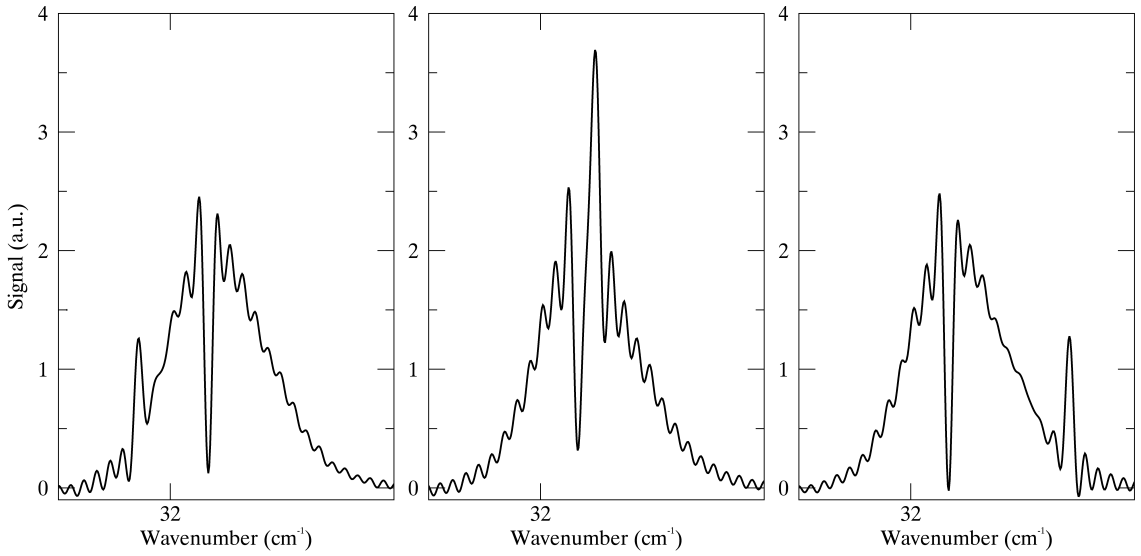

Figure 5.14: Measurements obtained from tuning one photomixer across the band while holding the other photomixer at a fixed frequency. These plots serve to illustrate the ability of the test set up to generate realistic astronomical spectra.

5.4.2 Integration of the Photomixers

Once both photomixers were integrated, the source module could be configured in two ways. From the lasers available for the photomixer, the source module could provide a monochromatic line anywhere in the spectral band of the PDPFTS (20 - 35 cm^{-1}). Alternatively, the photomixers can be configured to produce two monochromatic lines within a single resolution element of the PDPFTS in the finer range of $\sim$29.4 - 33.1 cm^{-1}. Both configurations allow for exploration of PDPFTS performance, such as the ability to extract key spectral parameters of emission/absorption features.

As shown in Figure 5.14, with the integration of the photomixers it is possible to generate realistic astronomical spectra consisting of continuum emission upon which is superimposed an unresolved emission and absorption line. Figure 5.14 depicts a series of such spectra measured with an absorption line fixed at 32.17 cm^{-1} while the second photomixer emission source is tuned across the band. These tests incorporated two temperature control systems; the absorption line was produced using an ILX LDC-3900 laser controller [110], and the emission line was produced using a Koheron laser controller [111].

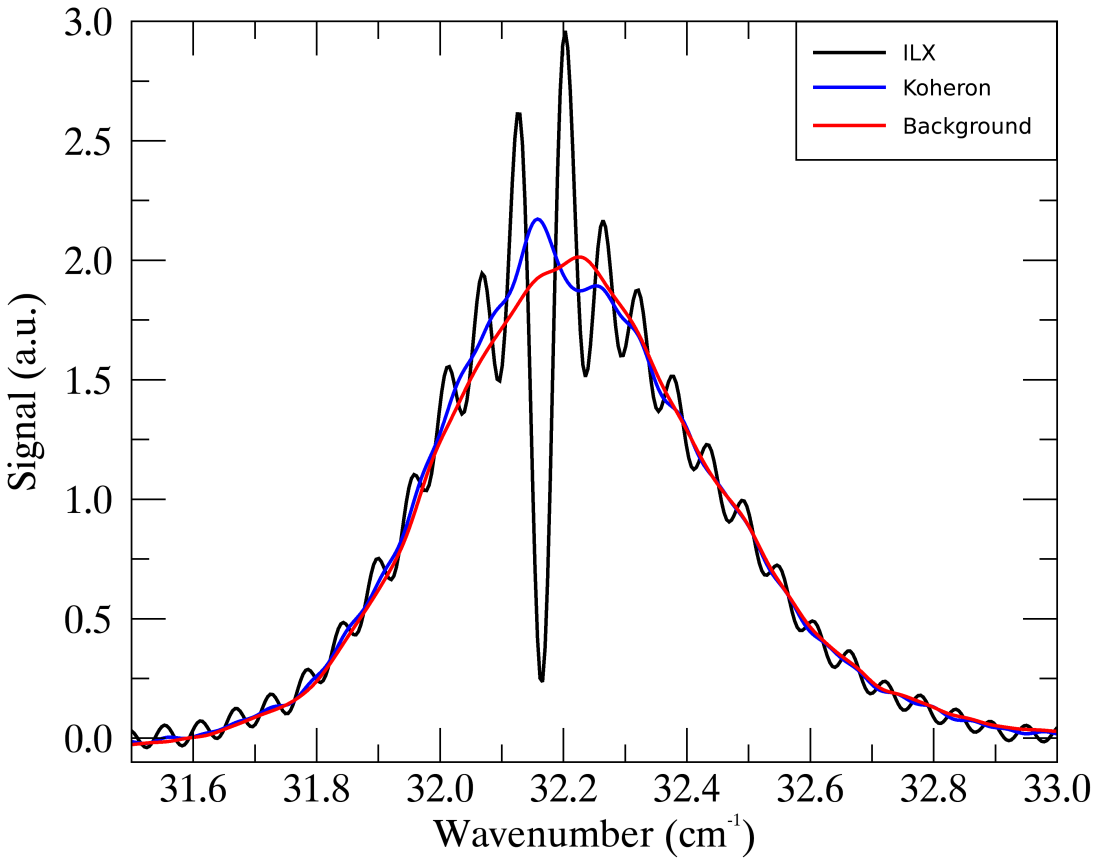

Figure 5.15: Results of the photomixer nulling test designed to compare the tuning precision of the two photomixer systems, the ILX (black) and Koheron (blue). Both photomixer systems are compared with the background (red) where neither photomixer was operating.

In order to probe the tuning precision of the laser controllers, a second test was performed where the wavelength and intensity of the absorption line was held fixed while the wavelength and intensity of the emission line was varied in an attempt to null the absorption line (Figure 5.15). The test was performed by first fixing the absorption line, then stepping the emission line at the temperature control resolution. The black trace shown in Figure 5.15 is the best nulling achieved by tuning an ILX LDC-3900 laser controller, which has a temperature control resolution of $\sim$0.1 K. The blue depicts the nulling achieved using the Koheron laser controller, which offers a temperature resolution of $<$ 1 mK. Both trials are compared directly with the background observed with both photomixers disabled (red trace). Using the Koheron laser controller, nulling is achieved not only at the line centre,

but also in the extended ILS sidelobes. Consequently, the ILX temperature controller was replaced with a second Koheron system.

5.4.3 Importance of Polarisation

As mentioned in Chapter 3, all gratings exhibit a polarization dependence which becomes increasingly important at higher angles of incidence. Consideration is required to ensure that the PDPFTS is properly aligned so as not to reduce the efficiency of the instrument. The PDPFTS was configured such that the output radiation from the cFTS was polarised parallel to the rulings of the grating spectrometer. Gratings are efficient for polarisations parallel to the rulings (P-Plane polarised) and far less efficient for polarisations perpendicular to the rulings (*S-Plane* polarised). The efficiency is critically dependent on the angles of incidence. Since gratings exhibit greater efficiency for P-Plane polarisation, and since the cFTS by nature outputs radiation with one polarisation, one can ensure that the cFTS outputs P-Plane polarised radiation into the the grating spectrometer. Thus, the efficiency of the system is optimized by aligning the polarisation between the cFTS and grating spectrometer.

To verify the sensitivity of the grating spectrometer, a test was performed where the input polariser and output analyser in the cFTS were each rotated 90° relative to their optimal orientation, meaning the radiation output from the cFTS was S-Plane polarised. The source module was configured to include a blackbody continuum and a photomixer line, both in emission. A series of measurements were made with the photomixer enabled and disabled, as shown in Figure 5.16. Since the output of the photomixer is linearly polarised, it was rotated to provide a maximum signal for both orientations of the polarisers. When compared with identical measurements taken in the optimal setup, the configuration producing perpendicularly polarised light exhibits a relative efficiency of $\sim$0.82. These results confirm that not only is the PDPFTS sensitive to the polarisation of input radiation, but also to the coupling between the cFTS and the grating module.

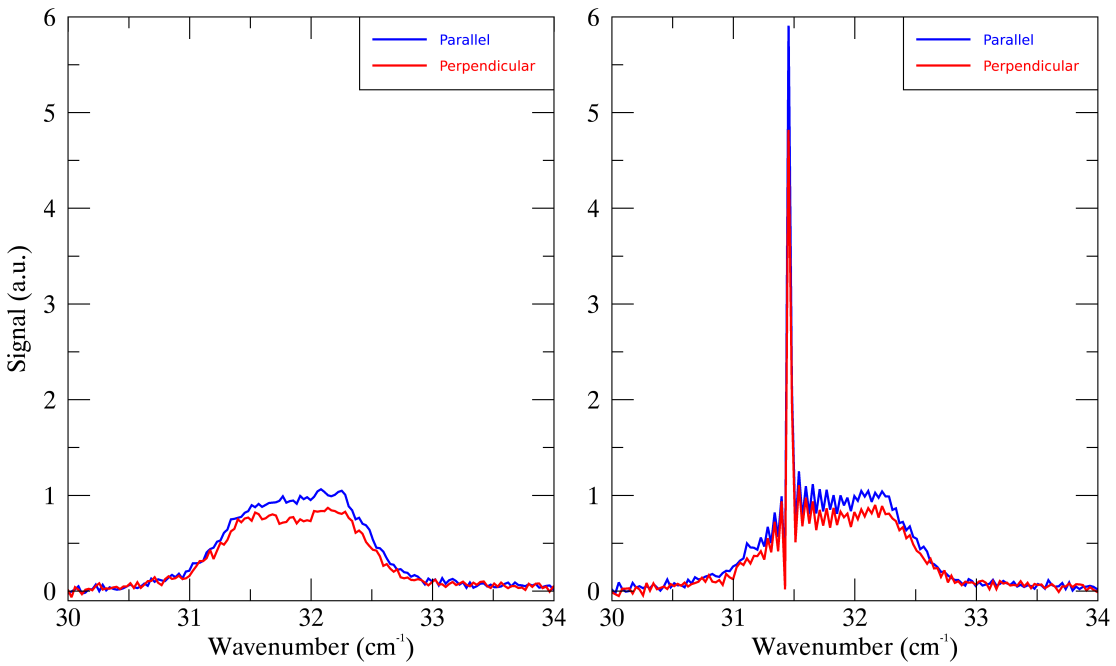

Figure 5.16: Preliminary PDPFTS measurements showing the polarisation sensitivity of the grating spectrometer. The polarisers in the cFTS were rotated such that the polarisation of the output radiation was parallel (blue) and perpendicular (red) to the rulings of the grating. The left panel depicts the results obtained when using only a blackbody source, while the right panels shows results from both the blackbody and photomixer sources. The results confirm that the system is more efficient when radiation passed into grating module is polarised parallel to the rulings.

5.4.4 Aliasing

Recall from Chapter 2 that failing to meet the Nyquist criteria results in an aliased interferogram. However, if a signal consists of only a narrow band with high out-of-band rejection, an aliased signal can potentially be reconstructed, a process known as *undersampling*. The sampling rate for a band limited Nyquist frequency is given by Equation 5.1. Undersampling can serve to reduce the amount of time required for a given scan, a feature important when observing conditions vary with time, such as atmospheric variations viewed by the James Clerk Maxwell Telescope (JCMT) [112]. Another advantage of undersampling is data reduction for a single scan, potentially reducing the requirements of communication protocols. However, in order to reduce the SNR to a value comparable to a spectrum whose sampling meets the Nyquist criterion, more observations are required.

$$\Delta x = \frac{1}{2(\sigma_N - \sigma_L)}. \qquad \text{[cm]} \quad (5.1)$$

The PDPFTS has the ability to exploit aliasing due to the narrow band produced by the grating module. Consequently, as shown in Figure 5.17, undersampling can be used to great effect due to the high out-of-band rejection. The black trace shows a spectrum sampled at a spacing of Δx =0.0032 cm ($\sigma_{Ny} = 156.25$ cm^{-1}), while the remaining traces were sampled at a spacing of Δx =$\sim$0.029 cm ($\sigma_{Ny} \approx 17.3$ cm^{-1}). The average of the aliased spectra was corrected using the relation $\sigma = 2m\sigma_{Ny} \pm \sigma_o$ and compared against the unaliased spectrum. The residual (green trace) shows that the emission continuum and ILS side lobes show excellent agreement, though there was a slight shift in the peak of the unresolved line which was less the resolution of the FTS. As seen in the right panel of Figure 5.17, the shift is within a fraction of the resolution element of the FTS.

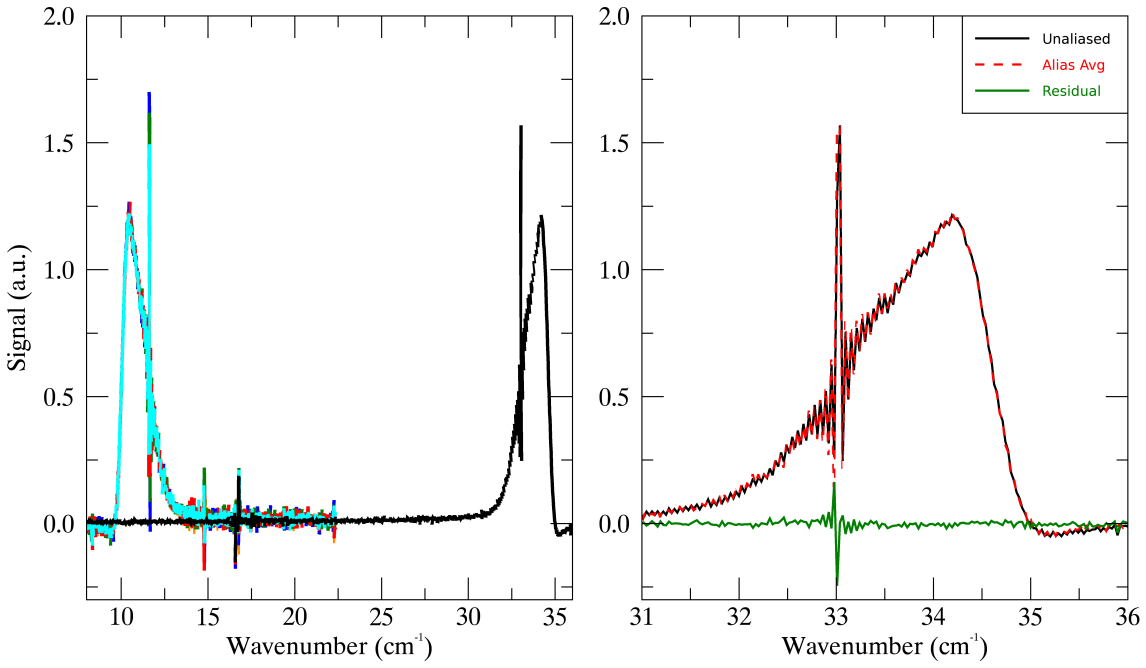

Figure 5.17: Exploiting aliasing in a PDPFTS. Left: A series of aliased spectra (coloured) compared to an unaliased spectrum (black). Right: The average of the aliased spectra are corrected (red) and compared to an unaliased spectrum. The residual indicates a slight difference, less than the resolution element of the FTS, in position of the unresolved line source between the aliased and unaliased spectra.

As mentioned above, undersampling helps to reduce the amount of data. In the case of the PDPFTS used throughout this thesis, the savings were not substantial due to a significant contribution from the metadata. However, undersampling provides a route for lossless data compression, which will be an important consideration in a space borne deployment, where data rates are always an issue. From a simplistic view, it can be seen from Equation 5.1 that the reduction in sampling could be up to the inverse of the resolving power of the grating, though in practice this could present issues with aliasing. This is especially important since a space borne deployment will use thousands of detectors. Thus, intentional aliasing becomes a built-in lossless compression algorithm.

5.5 Conclusion

Chapter 5 presented experimental results from a FIR PDPFTS. Section 5.2 introduced initial findings from the integration of the grating module into the PDPFTS, which informed a series of improvements to the system. Issues with phase correction in a PDPFTS were identified in Section 5.3, and a novel phase correction technique was presented. In Section 5.4, various aspects of the PDPFTS were verified, namely the functionality of the input ports (Section 5.4.1), the integration of the photomixers (Section 5.4.2), the sensitivity of the PDPFTS to polarisation (Section 5.4.3), and the ability of the PDPFTS to exploit aliasing (Section 5.4.4).

The results presented in this thesis show that the PDPFTS works as expected and there is excellent agreement between the simulations presented in Chapter 4 and the results presented in this chapter. In particular, it was confirmed that the cFTS and grating module are linear systems, leaving the ILS of the cFTS unchanged (Figure 5.11). Conclusions and future work on the FIR PDPFTS are presented in Chapter 6.

Chapter 6

Conclusions and Future Work

Don't adventures ever have an end? I suppose not.

Someone else always has to carry on the story.

Bilbo Baggins in The Fellowship of the Ring

J.R.R. TOLKIEN

6.1 Summary

This work has explored the design and verification of a novel far-infrared (FIR) hybrid post-dispersed polarising FTS (PDPFTS) system. As described in Chapter 1, the PDPFTS concept has been proposed as an instrument for the next generation of space-based observatories exploring the infrared universe. The theory of the FTS was explored in Chapter 2 with a focus on phase correction, which was predicted to be a challenge for the narrow spectral band available to the PDPFTS. Chapter 3 presented the theory and design of the PDPFTS, including the cryogenic grating spectrometer and calibration FTS (cFTS), as well as the extensive test suite of the PDPFTS used to characterize the system. In Chapter 4, simulations of the PDPFTS are presented for the purpose of exploring potential issues in analysing results obtained from a PDPFTS and the development of a processing pipeline. The simulator described in Chapter 4 produced theoretical spectra which were then compared and contrasted with experimental results obtained from the world's first FIR PDPFTS, the results of which are presented in Chapter 5.

6.2 PDPFTS Design

The PDPFTS prototype was constructed as a hybrid of a polarising FTS (the cFTS) [29] and a grating spectrometer [28], the former being held at room temperature under vacuum while the latter was cooled to 4 K within the Test Facility Cryostat (TFC). A complex source module was designed to measure two unresolved lines and a blackbody continuum. The system incorporated a Ge:Ga composite bolometer with a noise equivalent power (NEP) of $\sim 10^{-16}$ W$/\sqrt{\text{Hz}}$ which was cooled to temperatures of < 300 mK to increase the sensitivity of the detector [64].

The advantage of incorporating a polarising FTS is that the system can achieve high efficiency since the polarisation of the output radiation from the cFTS can be set to provide p-plane polarised light to the grating module. Additionally, the cFTS includes a second input port spatially separated from the first. Radiation incident to the orthogonal input maintains the orthogonal phase of the source, essentially inverting the two sources relative to each other. In this way, the input ports allow for the sources to simulate realistic astronomical features, particularly a combination of unresolved line sources measured as emission/absorption superimposed on an emission/absorption continuum.

Initial results from the PDPFTS showed a signal-to-noise ratio (SNR) between 50-75, which proved sufficient for line fitting. To provide a better analogue for future instruments, upgrades are currently underway for both the cFTS and grating module, as well as the instrumental test suite. A summary of these upgrades is as follows:

- The system's filtering will be upgraded to better match the passband of the PDPFTS.
- A longer stage will be incorporated into the cFTS, providing more than twice the resolution of the current configuration.
- A cryogenic slit will be included between the cFTS and grating module to enhance the resolution of the grating spectrometer while also reducing noise.

- A monolithic grating housing was designed to maintain mechanical and optical alignment at cryogenic temperatures and increase the optical throughput [91].
- The second photomixer source controller was upgraded to a pair of Koheron CTL200 controllers for finer temperature control [111].
- The photomixer bias boxes were upgraded to provide more power.
- The current photomixers will be replaced with units capable of operating under vacuum at cryogenic temperatures.
- The thermal braids in the TFC were upgraded to reduce both the cooling time and the temperature of the bolometer detector.

Future work on the PDPFTS will incorporate a fully cryogenic system, including the polarising FTS and the source module. Work within the astronomical instrumentation group (AIG) to develop a fully cryogenic polarising FTS is being assisted by industrial partners, ABB [86] and Blue Sky Spectroscopy [29]. The source module will include a flight spare of the spectrometer calibrator (SCAL) from the Herschel-SPIRE instrument [83], which is a continuum calibration source with space heritage. Since SCAL has been designed to operate under vacuum at cryogenic temperatures, the final challenge for the source module is to incorporate the unresolved line sources from the current photomixers, which are not hermetic, into the cryostat.

6.3 Phase Correction

In the field of FTS, such as Fourier-transform infrared spectroscopy, it is typical to extract phase over a broad spectral range. However, by design, the passband of the PDPFTS on a single detector is severely limited in this regard. Consequently, the limited passband diminishes the available phase information to a range of 0.5 - 2 cm^{-1} with minimal data points.

Early predictions of the PDPFTS functionality, included in the simulations, predicted a linear phase could be extracted with as few as three points in the measured spectrum as the linearity would be preserved. It was quickly noted, however, that the attenuation from the grating spectrometer introduced issues in extracting the phase as the SNR varied across the band. The results showed that a consistent phase could not be readily extracted from a single scan. However, as more scans were performed, it was found that a linear phase could be extracted by analysing the peaks of the measured phase from a series of scans across the band (see Figure 5.8). Thus, a procedure was developed whereby a coherent linear phase could be extracted under the assumption that there was no shift in the measured position of zero path difference (ZPD) across the scans.

The process of phase correction is further simplified when an array of detectors is used, such as the PDPFTS design proposed for the SPICA SAFARI instrument. When an array of detectors is used, the grating spectrometer can be fixed in place to avoid the issues of having moving parts in space. For phase correction, this proves advantageous since the phase information is simultaneously detected across each detector in the array, rather than measuring multiple scans and assuming no shift in ZPD. Thus, accurate phase correction is readily attainable across multiple forms of PDPFTS, and in particular, the format best suited for space-based applications.

6.4 Line Extraction

A key requirement for characterizing the PDPFTS is understanding the instrumental line shape (ILS) of the instrument. The ILS for both the grating spectrometer and FTS are well known and predictable. Early work with simulations predicted that the ILS for the PDPFTS is a combination of the characteristic *sinc* function of the FTS with the approximately *Gaussian* nature of the grating spectrometer. More specifically, the predictions indicated that the entirety of the *sinc* ILS was preserved. The apparent reduction in the amplitude is due to the fact that the signal is modulated by the spectral response function

of the grating spectrometer. As shown in Figure 5.11, these predictions were confirmed experimentally, with results showing that the *sinc* feature indicative of the FTS ILS can be extracted from a PDPFTS spectrum. In practice, the grating response function will be a calibration product, which will be used to restore the true amplitude of the *sinc* ILS.

Knowing how the ILS of both the grating spectrometer and FTS interact in the PDPFTS presents two interesting conclusions. Firstly, line extraction and analysis techniques for infrared spectroscopy can be readily applied to results from the PDPFTS. Secondly, the modulation of the signal from the ILS of the grating spectrometer presents a new challenge: calibration. Light is dispersed by the grating module, reducing the observed amplitude of any features across multiple positions (for a monochromator) or detectors (for a detector array).

6.5 Calibration Products

Characterization of the PDPFTS will necessitate calibration of both the source module and detector systems. Calibration of the former may be as simple as incorporating the flight spare of SCAL, since it has space heritage as a continuum calibration source. For the latter, responsivity of the bolometer must be characterized if the absolute flux calibration of the PDPFTS is to be determined.

While the PDPFTS used throughout this thesis incorporated one detector, any practical implementation will have a fixed grating and include thousands of detectors in an array to avoid moving parts. In order to reconstruct a full spectrum, in addition to the phase correction procedure discussed in this thesis, there is also an issue of numerous calibration products for both spatial and spectral, and possibly temporal, responses which will be needed to stitch the spectra together. As an example, four calibration products were required when viewing a point source using the Herschel-SPIRE instrument, with 6000 detectors on SPICA SAFARI the number of calibration products will easily exceed 10000 [113]. Additionally, viewing extended sources increases the number of calibration products

required. The campaign of characterizing the PDPFTS and accompanying test equipment represents future work to be performed at the AIG.

6.6 Conclusion

The design and exploration of a FIR PDPFTS and the accompanying challenges was successful, and experimental results from the PDPFTS prototype have been presented. Preliminary results show that analytical techniques associated with spectroscopy can be readily applied with minor adjustments. Performance of the PDPFTS was compared against simulations showing excellent agreement with theory. A significant focus of this work was directed towards the challenges of phase correction given the narrow bandwidth of the PDPFTS. These challenges were explored and a technique has been developed for reliable phase correction of PDPFTS spectra.

Several improvements to the PDPFTS were performed over the duration of this work. However, continuation of the PDPFTS characterization will see the instrument shift to a completely cryogenic design, including the source module. Advancements in this work will be performed by future graduate students at the AIG, which will incorporate the techniques developed throughout this work.

Bibliography

[1] D. Lutz. Far-infrared surveys of galaxy evolution. *Annual Review of Astronomy and Astrophysics*, 52(1):373 – 414, 2014.

[2] E. Hubble. A relation between distance and radial velocity among extragalactic nebulae. In *Proceedings of the National Academy of Sciences of the United States of America*, volume 15, pages 168 – 173, Mar. 1929.

[3] NASA: Cool Cosmos. IR Atmospheric Windows. `http://coolcosmos.ipac.caltech.edu/cosmic$_$classroom/ir$_$tutorial/irwindows.html`.

[4] I. Glass. *Handbook of Infrared Astronomy*. Cambridge Observing Handbooks for Research Astronomers. Cambridge University Press, 1999.

[5] Maunakea Observatories Support Services. Maunakea Visitor Information Station. `http://www.ifa.hawaii.edu/info/vis/visiting-mauna-kea.html`.

[6] A. Reinacher et al. The SOFIA Telescope in Full Operation. *Journal of Astronomical Instrumentation*, 07(04):1840007, 2018.

[7] J.E. Dyson and D.A. Williams. *The Physics of the Interstellar Medium*. 1997.

[8] M. Planck. *Über eine Verbesserung der Wienschen Spektralgleichung*, pages 175–178. Vieweg+Teubner Verlag, Wiesbaden, 1978.

[9] D. Farrah et al. Review: far-infrared instrumentation and technological development for the next decade. *Journal of Astronomical Telescopes, Instruments, and Systems*, 5(2):1 – 34, 2019.

[10] G. Neugebauer et al. The Infrared Astronomical Satellite (IRAS) mission. *The Astrophysical Journal Letters*, 278:L1–L6, March 1984.

[11] T. Matsumoto and H. Murakami. Infrared Telescope in Space (IRTS) mission. In Marija S. Scholl and Bjorn F. Andresen, editors, *Infrared Spaceborne Remote Sensing IV*, volume 2817, pages 238 – 247. International Society for Optics and Photonics, SPIE, 1996.

[12] M.F. Kessler. The infrared space observatory (iso) mission. *Advances in Space Research*, 30(9):1957–1965, 2002.

[13] M. Werner et al. The Spitzer Space Telescope Mission. *The Astrophysical Journal Supplement Series*, 154(1):1–9, sep 2004.

[14] H. Murakami et al. The Infrared Astronomical Mission AKARI. *Publications of the Astronomical Society of Japan*, 59(sp2):S369–S376, 10 2007.

[15] G. Pilbratt. Herschel mission overview and key programmes. In Jacobus M. Oschmann Jr., Mattheus W. M. de Graauw, and Howard A. MacEwen, editors, *Space Telescopes and Instrumentation 2008: Optical, Infrared, and Millimeter*, volume 7010, pages 1 – 12. International Society for Optics and Photonics, SPIE, 2008.

[16] M.J. Griffin, B.M. Swinyard, and L. Vigroux. The Herschel-SPIRE Instrument. In John C. Mather, editor, *Optical, Infrared, and Millimeter Space Telescopes*, volume 5487, pages 413 – 424. International Society for Optics and Photonics, SPIE, 2004.

[17] S. Ragan et al. The Earliest Phases of Star Formation (EPoS): a Herschel program - The precursors to high-mass stars and clusters. *Astronomy and Astrophysics*, 547:A49, 2012.

[18] S. Serjeant et al. Herschel ATLAS: The cosmic star formation history of quasar host galaxies. *Astronomy and Astrophysics*, 518:L7, 2010.

[19] A. Abergel et al. Evolution of interstellar dust with Herschel. First results in the photodissociation regions of NGC3. *Astronomy and Astrophysics*, 518:L96, 2010.

[20] P. Lightsey. James Webb Space Telescope: a large deployable cryogenic telescope in space. In Gregory J. Exarhos, Arthur H. Guenther, Keith L. Lewis, Detlev Ristau, M. J. Soileau, and Christopher J. Stolz, editors, *Laser-Induced Damage in Optical Materials: 2007*, volume 6720, pages 138 – 149. International Society for Optics and Photonics, SPIE, 2007.

[21] B. Swinyard et al. The space infrared telescope for cosmology and astrophysics: Spica a joint mission between jaxa and esa. *Experimental Astronomy*, 23(1):193–219, March 2009.

[22] P. Roelfsema et al. SPICA—a large cryogenic infrared space telescope: Unveiling the obscured universe. *Publications of the Astronomical Society of Australia*, 35:e030, 2018.

[23] European Space Agency. ESA selects three new mission concepts for study. `http://www.https://www.esa.int/Science_Exploration/Space_Science/ESA_selects_three_new_mission_concepts_for_study`.

[24] European Space Agency. SPICA NO LONGER CANDIDATE FOR ESA'S M5 MISSION SELECTION. `http://www.https://sci.esa.int/web/cosmic-vision/-/spica-no-longer-candidate-for-esa-s-m5-mission-selection`.

[25] D.L. Clements, S. Serjeant, and S. Jin. Explain esa's last-minute ditching of new space telescope. *Nature*, 587(548), November 2020.

[26] W. Jellema et al. Safari: instrument design of the far-infrared imaging spectrometer for spica. In Zoran Sodnik, Bruno Cugny, and Nikos Karafolas, editors, *International Conference on Space Optics — ICSO 2014*, volume 10563, pages 460 – 467. International Society for Optics and Photonics, SPIE, 2017.

[27] S.P. Davis et al. *Fourier Transform Spectrometry*. Academic Press, San Diego, California, 1 edition, 2001.

[28] A. Anderson. Design and testing of a cryogenic diffraction grating spectrometer. Honour's thesis, University of Lethbridge, 2020.

[29] Blue Sky Spectroscopy Inc. `www.blueskyspectroscopy.com/`.

[30] J.B.J. Fourier. *Mémoire sur la propagation de la chaleur dans les corps solides*, volume 2 of *Cambridge Library Collection - Mathematics*, page 213–222. Cambridge University Press, 2013.

[31] J.B.J. Fourier. *Théorie Analytique De La Chaleur*. F. Didot, 1822.

[32] I. Grattan-Guinness and J.R. Ravetz. *Joseph Fourier 1768-1830: a Survey of His Life and Work*. MIT Press, 1972.

[33] P.G. Lejeune-Dirichlet. Sur La Convergence Des Séries Trigonométriques Qui Servent à Représenter Une Fonction Arbitraire Entre Des Limites Données. *Journal Für Die Reine Und Angewandte Mathematik*, 4:157–169, 1929.

[34] D.C. Champeney. *A Handbook of Fourier Theorems*. Cambridge University Press, 1987.

[35] R.N. Bracewell. *The Fourier Transform and Its Applications*. McGraw-Hill, 1986.

[36] A.A. Michelson. Visibility of Interference-Fringes in the Focus of a Telescope. *Publications of the Astronomical Society of the Pacific*, 4(16):217–220, 6 1891.

[37] A.A. Michelson. *Light waves and their uses*. University of Chicago Press, 1903.

[38] A.A. Michelson. Application of Interference Methods to Spectroscopic Measurement. *Publications of the Astronomical Society of the Pacific*, 4:190, 1892.

[39] A.A. Michelson. Recent Advances in Spectroscopy. In *Nobel Lectures in Physics, 1901-1921*, chapter 1907, pages 166–178. World Scientific, 1998.

[40] R.J. Bell. *Introductory Fourier Transform Spectroscopy*. Academic Press, New York, New York, 1 edition, 1972.

[41] J.W. Cooley and J.W. Tukey. An algorithm for the machine calculation of complex Fourier series. *Mathematics of Computation*, 19(90):297–301, 4 1965.

[42] J. Connes and P. Connes. Near-infrared planetary spectra by Fourier spectroscopy. i. instruments and results. *J. Opt. Soc. Am.*, 56(7):896–910, Jul 1966.

[43] J. Connes, P. Connes, and J.P. Maillard. *Atlas des spectres dans le proche infrarouge de Venus, Mars, Jupiter et Saturn*. Ed. Du Centre National De La Recherche Scientifique, 1969.

[44] D.A. Naylor and B.G. Gom. FTS-2: A Submillimetre Astronomical Imaging Fourier Transform Spectrometer. In *Fourier Transform Spectroscopy/ Hyperspectral Imaging and Sounding of the Environment*, page FWA1. Optical Society of America, 2007.

[45] M.A. Parseval. *Mémoires presentés a L'Institut des Sciences, Lettres et Arts, par divers savantsèt lus dans ses assemblées : Sciences, Mathématiques et Physiques*, volume 1. Mémoires de mathématique et de physique, presentés par divers Scavans, & lûs dans ses Assemblées, 1806.

[46] T.G. Stockham. High-speed convolution and correlation. In *AFIPS '66 (Spring)*, 1966.

[47] K.F. Riley et al. *Mathematical Methods for Physics and Engineering*. Cambridge University Press, Cambridge, United Kingdom, 3 edition, 2006.

[48] E. Hecht. *Optics*. Pearson Education, USA, 5 edition, 2017.

[49] D.A. Naylor et al. The effects of beamsplitter emission in a balanced Fourier transform spectrometer. In *2008 33rd International Conference on Infrared, Millimeter and Terahertz Waves*, pages 1–2, Sep. 2008.

[50] P.B. Fellgett. *The Theory of Infrared Sensitivities and Its Application to Investigations of Stellar Radiation in the Near Infra-red*. PhD thesis, University of Cambridge, 1949.

[51] P.B. Fellgett. Equivalent Quantum-Efficiencies of Photographic Emulsions. *Monthly Notices of the Royal Astronomical Society*, 118(3):224–233, 06 1958.

[52] S.E. Schwarz and W.G. Oldham. *Electrical Engineering: An Introduction*. Oxford series in electrical and computer engineering. Oxford University Press, 1993.

[53] D.A. Naylor et al. Design and performance of a dual polarizing detector system for broadband astronomical spectroscopy at submillimeter wavelengths. *Review of Scientific Instruments*, 70(10):4097–4109, 1999.

[54] J.C. Mather. Bolometer noise: nonequilibrium theory. *Appl. Opt.*, 21(6):1125–1129, Mar 1982.

[55] D. Naylor et al. Development of a cryogenic far-infrared post-dispersed polarizing Fourier transform spectrometer: a demonstrator for the SPICA SAFARI instrument. In Jonas Zmuidzinas and Jian-Rong Gao, editors, *Millimeter, Submillimeter, and Far-Infrared Detectors and Instrumentation for Astronomy X*, volume 11453, pages 117 – 127. International Society for Optics and Photonics, SPIE, 2020.

[56] J.P. Maillard. Signal-To-Noise Ratio and Astronomical Fourier Transform Spectroscopy. In G. Cayrel de Strobel and Monique Spite, editors, *The Impact of Very High S/N Spectroscopy on Stellar Physics*, volume 132 of *IAU Symposium*, pages 71–78, 1988.

[57] D.C. Backer. The 1.5 millisecond pulsar. *Comments on Astrophysics*, 10:23–26, September 1983.

[58] C. Kittel. *Introduction to Solid State Physics*. Oxford University Press, New York, 8 edition, 2005.

[59] K.D. Irwin and G.C. Hilton. *Transition-Edge Sensors*, pages 63–150. Springer Berlin Heidelberg, Berlin, Heidelberg, 2005.

[60] R.F. Voss and J. Clarke. Flicker ($\frac{1}{f}$) noise: Equilibrium temperature and resistance fluctuations. *Phys. Rev. B*, 13:556–573, Jan 1976.

[61] H.V. Malmstadt, C.G. Enke, and S.R. Crouch. *Electronics and Instrumentation for Scientists*. Benjamin/Cummings Publishing Company, 1981.

[62] Aerotech Inc. `www.aerotech.com/`.

[63] A.S. Sedra and K.C. Smith. *Microelectronic Circuits*. Oxford University Press, New York, 1998.

[64] B.G. Gom. A cryogenic detector for submillimetre astronomy. Master's thesis, University of Lethbridge, 1999.

[65] A.J. Diefenderfer and B.E. Holton. *Principles of Electronic Instrumentation*. Saunders College Publishing, USA, 3 edition, 1994.

[66] D.A. Naylor et al. Increased efficiency through undersampling in fourier transform spectroscopy. In *Fourier Transform Spectroscopy/ Hyperspectral Imaging and Sounding of the Environment*, pages 1–3. Optical Society of America, 2005.

[67] E.O. Brigham. *The Fast Fourier Transform and its Applications*. Prentice Hall, Englewood Cliffs, New Jersey, 1 edition, 1988.

[68] C.F. Gauss. *Werke*, volume 3, chapter Theoria interpolationis methodo nova tractata, pages 265–327. Göttingen, Germany: Königliche Gesellschaft der Wissenschaften, 1866.

[69] David Naylor. The evolving role of Fourier transform spectroscopy in far-infrared space astronomy. In *2020 45th International Conference on Infrared, Millimeter, and Terahertz Waves (IRMMW-THz)*, pages 1 – 3, 2020.

[70] J. Connes. *Spectroscopic studies using Fourier transformation*, volume 3157. US Naval Ordnance Test Station, 1963.

[71] T.R. Fulton et al. The data processing pipeline for the Herschel/SPIRE imaging Fourier Transform Spectrometer. In Jacobus M. Oschmann Jr., Mattheus W. M. de Graauw, and Howard A. MacEwen, editors, *Space Telescopes and Instrumentation 2008: Optical, Infrared, and Millimeter*, volume 7010, pages 846 – 857. International Society for Optics and Photonics, SPIE, 2008.

[72] L. Mertz. *Transformations in optics*. John Wiley and Sons Ltd, 1965.

[73] M.L. Forman. Fast Fourier-transform technique and its application to Fourier spectroscopy. *J. Opt. Soc. Am.*, 56(7):978–979, Jul 1966.

[74] T.P. Sheahen. Importance of proper phase analysis in using Fourier transforms. *American Journal of Physics*, 44(1):22–25, 1976.

[75] D.G. Johnson, W.A. Traub, and K.W. Jucks. Phase determination from mostly one-sided interferograms. *Applied optics*, 35 16:2955–9, 1996.

[76] F. Binczyk, R. Tarnawski, and J. Polanska. Strategies for optimizing the phase correction algorithms in nuclear magnetic resonance spectroscopy. *Biomed Eng Online*, 14, 2015.

[77] D.A. Naylor, T.A. Clark, and G.R. Davis. Polarizing Fourier transform spectrometer for astronomical spectroscopy at submillimeter and mid-infrared wavelengths. In David L. Crawford and Eric R. Craine, editors, *Instrumentation in Astronomy VIII*, volume 2198, pages 703 – 714. International Society for Optics and Photonics, SPIE, 1994.

[78] HyperPhysics. C.R. Nave. `http://hyperphysics.phy-astr.gsu.edu/`.

[79] D.H. Martin and E. Puplett. Polarised interferometric spectrometry for the millimetre and submillimetre spectrum. *Infrared Physics*, 10(2):105 – 109, 1970.

[80] Wikipedia contributors. Polarizer — Wikipedia, the free encyclopedia. `http://https://en.wikipedia.org/wiki/Polarizer`, 2021. [Online; accessed 01-June-2021].

[81] L. Zehnder. Ein neuer Interferenzrefraktor. *Zeitschrift für Instrumentenkunde*, 11:275–285, 1891.

[82] L. Mach. Ueber einen Interferenzrefraktor. *Zeitschrift für Instrumentenkunde*, 12:89–93, 1892.

[83] P. Hargrave et al. Performance of flight-model on-board calibration sources on Herschel-SPIRE. In Jonas Zmuidzinas, Wayne S. Holland, Stafford Withington, and William D. Duncan, editors, *Millimeter and Submillimeter Detectors and Instrumentation for Astronomy III*, volume 6275, pages 353 – 364. International Society for Optics and Photonics, SPIE, 2006.

[84] G. D'Alessandro et al. Common-mode rejection in Martin-Puplett spectrometers for astronomical observations at millimeter wavelengths. *Appl. Opt.*, 54(31):9269 – 9276, Nov 2015.

[85] P.S. Barry. *On the development of SuperSpec; a Fully Integrated On-chip Spectrometer for Far-infrared Astronomy*. PhD thesis, Cardiff University, 2014.

[86] A. Cournoyer et al. Design of a novel cryogenic stiffness-compensated reactionless scan mechanism for the Fourier transform spectrometer of SPICA SAFARI instrument. In Jonas Zmuidzinas and Jian-Rong Gao, editors, *Millimeter, Submillimeter, and Far-Infrared Detectors and Instrumentation for Astronomy X*, volume 11453, pages 526 – 545. International Society for Optics and Photonics, SPIE, 2020.

[87] I.T. Veenendaal. *A Novel Fabry-Pérot Interferometer for Far-Infrared Astronomy*. PhD thesis, University of Lethbridge, 2019.

[88] C. Palmer. *Diffraction Grating Handbook*. Three centuries of science in America. Newport, 7 edition, 2014.

[89] M. Czerny and A.F. Turner. Über den Astigmatismus bei Spiegelspektrometern. *Zeitschrift fur Physik*, 61(11-12):792–797, November 1930.

[90] D.J. Griffiths. *Introduction to Electrodynamics*. Pearson, 4 edition, 2013.

[91] A. Anderson et al. Development of a cryogenic far-infrared grating spectrometer for a post-dispersed fourier transform spectrometer. In *2020 45th International Conference on Infrared, Millimeter, and Terahertz Waves (IRMMW-THz)*, pages 1–2, 2020.

[92] Scitec Instruments ltd. IR Sources. `www.scitec.uk.com/`.

[93] TOPTICA Photonics. GaAs and InGaAs Photomixers. `www.toptica.com/`.

[94] E. Pliński. Terahertz photomixer. *Bulletin of the Polish Academy of Sciences: Technical Sciences*, 58(No 4):463–470, 2010.

[95] S. Preu et al. Tunable, continuous-wave terahertz photomixer sources and applications. *Journal of Applied Physics*, 109(6):061301, 2011.

[96] M. Tani et al. Generation of terahertz radiation by photomixing with dual- and multiple-mode lasers. *Semiconductor Science and Technology*, 20:S151, 06 2005.

[97] G. Makiwa. Performance Characterization of a Millimeter-Wave Photomixer. Master's thesis, University of Lethbridge, 2011.

[98] Furukawa Electric Co., ltd. Fitel Products. `www.fitel.com/`.

[99] Cryomech. `www.cryomech.com/`.

[100] Chase Research Cryogenics ltd. `www.chasecryogenics.com/`.

[101] I.T. Veenendaal. A cryogenic test facility. Master's thesis, University of Lethbridge, 2016.

[102] Vishay Semiconductors. H11A1. www.vishay.com/docs/83730/h11a1.pdf.

[103] Measurement Computing. USB-1808 Series. www.mccdaq.com/.

[104] Harris Geospatial Solutions, Inc. www.l3harrisgeospatial.com/.

[105] I.E. Gordon et al. The hitran2016 molecular spectroscopic database. *Journal of Quantitative Spectroscopy and Radiative Transfer*, 203:3 – 69, 2017. HITRAN2016 Special Issue.

[106] R. Stephens. *Beginning Database Design Solutions*. Wiley Publishing, Inc., 1 edition, 2009.

[107] A. Anderson et al. Development of a Far-infrared Grating Spectrometer for a Post-dispersed Fourier Transform Spectrometer. In *OSA Optical Sensors and Sensing Congress*. International Society for Optics and Photonics, OSA, 2021. Accepted.

[108] A. Huber et al. Development of a Fourier Transform Spectrometer to Assess Performance of an Analogue of the SPICA SAFARI Instrument. In *2020 45th International Conference on Infrared, Millimeter, and Terahertz Waves (IRMMW-THz)*, pages 1–2, 2020.

[109] P.A.R. Ade et al. A review of metal mesh filters. In Jonas Zmuidzinas, Wayne S. Holland, Stafford Withington, and William D. Duncan, editors, *Millimeter and Submillimeter Detectors and Instrumentation for Astronomy III*, volume 6275, pages 248 – 262. International Society for Optics and Photonics, SPIE, 2006.

[110] Newport Corp. LDC-3900 Modular 4-Channel Laser Diode Controller. www.newport.com/.

[111] Koheron SAS. Digital butterfly laser diode controller. www.koheron.com/.

[112] D. Naylor et al. Astronomical spectroscopy using an aliased step-and-integrate Fourier transform spectrometer. In Jonas Zmuidzinas, Wayne S. Holland, and Stafford Withington, editors, *Millimeter and Submillimeter Detectors for Astronomy II*, volume 5498, pages 685 – 694. International Society for Optics and Photonics, SPIE, 2004.

[113] T. Fulton et al. Overcoming Processing Challenges for a Post-dispersed Fourier Transform Spectrometer. In *OSA Optical Sensors and Sensing Congress*. International Society for Optics and Photonics, OSA, 2021. Accepted.

[114] B. Riemann. *Ueber die Darstellbarkeit einer Function durch eine trigonometrische Reihe*. Dieterich, Göttingen, 1867.

[115] G.B. Folland. *Fourier Analysis and Its Applications*. American Mathematical Society, 2009.

[116] P.A.M. Dirac. *The Principles of Quantum Mechanics*. Clarendon Press, 1930.

[117] EXFO Inc. WA-1500 and WA-1000 Wavemeter. www.exfo.com/.

Appendix A

Derivation of the Fourier Transform

When Fourier made his claim in 1807 that a function may be represented as a sum of sine and cosine terms, his work was aimed at exploring heat flow in a solid [31]. He defined the initial temperature distribution, $f(x)$ of a one-dimensional solid to be given as

$$f(x) = \sum_{n=0}^{\infty} [a_n \cos(nkx) + b_n \sin(nkx)], \tag{A.1}$$

where a_n and b_n are the *Fourier Coefficients*, x is position along the 1-D solid (m), n is an integer, and k is the angular wavenumber defined as $k = \frac{2\pi}{\lambda}$ [31]. Throughout Appendix A an arbitrary wavelength will be represented as L, such as seen in Figure A.1.

A.1 Dirichlet Conditions

The assertions made by Fourier, however appealing, lacked mathematical rigour, and a formal proof was not given until 1829 when Dirichlet proved the convergence of the Fourier series [32]. The proof given by Dirichlet required a set of restrictive conditions which, if met, ensured the convergence of the Fourier series [33]. These restrictions are called the *Dirichlet conditions*, and are summarized as follows for a function $f(x)$:

i) f must be periodic

ii) f must be single valued and continuous, with the exception of a finite number of finite discontinuities

iii) f must have a finite number of maxima and minima within one period

iv) f must be absolutely integrable over one period

For finite discontinuities the value of the expanded function will be the mean of the upper and lower limit of the discontinuity. In most physical applications of Fourier series, the final three conditions are almost always met. Many functions are not periodic and fail to meet the first condition without manipulation, which is possible only for functions within a fixed range. However, any function can be extended in such a way as to make it periodic. Any function can be expressed as a combination of an even and an odd function, which not only simplifies analysis but often provides insight into the system being studied. A simple example is given in Figure 1, where a function is extended to be asymmetric, odd, and even.

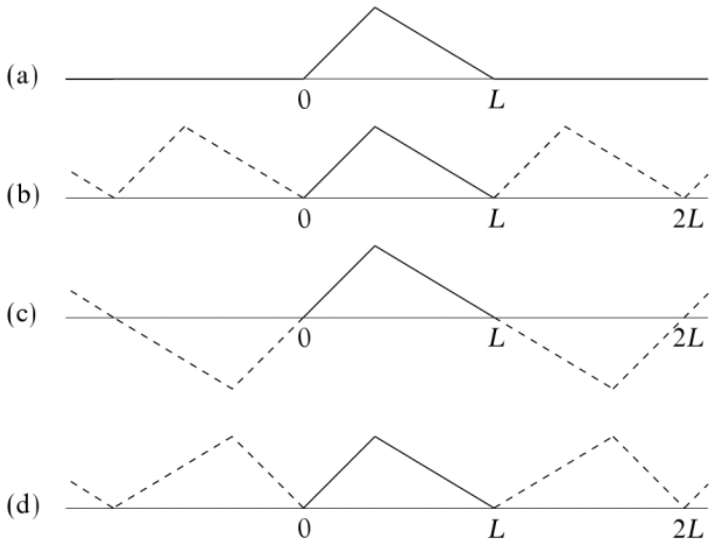

Figure A.1: Periodic extension of a function. A non-periodic function in a fixed range (a) may be made periodic by extending the function outside the fixed range in a periodic fashion. (b) shows the asymmetric function produced by repeating (a), while (c) and (d) show the extended function may be manipulated to produce odd and even functions respectively [47].

A significant feature of the Fourier series is that all the terms are mutually orthogonal. In other words, the integral of the product of two terms converges only for identical terms where the value of n is greater than zero. Consider two terms of finite wavelength, L, with $n = r$ and $n = p$ respectively. The following properties are true [47, 27]:

$$\int_{x_o}^{x_o+L} \sin\left(\frac{2\pi rx}{L}\right)\cos\left(\frac{2\pi px}{L}\right)\,\mathrm{d}x = 0 \quad \text{for all } r \text{ and } p, \tag{A.2}$$

$$\int_{x_o}^{x_o+L} \cos\left(\frac{2\pi rx}{L}\right)\cos\left(\frac{2\pi px}{L}\right)\,\mathrm{d}x = \begin{cases} L, & \text{for } r = p = 0. \\ L/2, & \text{for } r = p > 0. \\ 0, & \text{for } r \neq p. \end{cases} \tag{A.3}$$

$$\int_{x_o}^{x_o+L} \sin\left(\frac{2\pi rx}{L}\right)\sin\left(\frac{2\pi px}{L}\right)\,\mathrm{d}x = \begin{cases} 0, & \text{for } r = p = 0. \\ L/2, & \text{for } r = p > 0. \\ 0, & \text{for } r \neq p. \end{cases} \tag{A.4}$$

x_o is an arbitrary point, though is often assumed to be either 0 or $-L/2$.

A.2 Fourier Coefficients

Under the assumption that the Dirichlet conditions are met, the Fourier coefficients may be calculated. Recall that a function $f(x)$ may be defined as Fourier series of the form given by Equation A.1. The first step in calculating the Fourier coefficients is to multiply $f(x)$ by

$\cos(pkx)$, or $\cos(2\pi px/L)$, and integrating over one period:

$$\int_{x_o}^{x_o+L} f(x)\cos\left(\frac{2\pi px}{L}\right)\,\mathrm{d}x = \sum_{n=0}^{\infty} a_n \int_{x_o}^{x_o+L} \cos\left(\frac{2\pi nx}{L}\right)\cos\left(\frac{2\pi px}{L}\right) + \sum_{n=0}^{\infty} b_n \int_{x_o}^{x_o+L} \sin\left(\frac{2\pi nx}{L}\right)\cos\left(\frac{2\pi px}{L}\right). \tag{A.5}$$

Recall the orthogonality conditions from Equations A.2-A.4. These conditions imply that the second term vanishes, leaving only the solutions for a_n. The same process could be performed using $\sin(2\pi px/L)$ to obtain the values for b_n. Going forward it is clear that the result depends on whether or not $n = p$ and whether or not $p > 0$. When $p = 0$ the result is:

$$\int_{x_o}^{x_o+L} f(x)\,\mathrm{d}x = a_0 L \tag{A.6}$$

It is common practice to represent a_0 by a value $a_0/2$ such that all the coefficient a_n may be defined by the same equation [34, 47]. The result is given as:

$$\int_{x_o}^{x_o+L} f(x)\,\mathrm{d}x = \frac{a_0}{2} L. \tag{A.7}$$

Looking back at Equation A.5, the modified form of a_0 matches that given when $p \neq 0$:

$$\int_{x_o}^{x_o+L} f(x)\cos\left(\frac{2\pi nx}{L}\right)\,\mathrm{d}x = \frac{a_n}{2} L. \tag{A.8}$$

A similar solution may be derived for b_n. Th coefficients are therefore defined as:

$$a_n = \frac{2}{L}\int_{x_o}^{x_o+L} f(x)\cos\left(\frac{2\pi nx}{L}\right)\,\mathrm{d}x, \tag{A.9}$$

and

$$b_n = \frac{2}{L}\int_{x_o}^{x_o+L} f(x)\sin\left(\frac{2\pi nx}{L}\right)\,\mathrm{d}x. \tag{A.10}$$

With the inclusion of the $1/2$ factor for the a_0, Equation A.1 may be expressed as

$$f(x) = \frac{a_0}{2} + \sum_{n=1}^{\infty} [a_n \cos(nkx) + b_n \sin(nkx)]. \tag{A.11}$$

A.3 Complex Fourier Series

Alternatively, equation A.1 may be expressed in complex notation using Euler's law, $e^{i\phi} = \cos(\phi) + i\sin(\phi)$. The result is the *Complex Fourier series*, which is given as:

$$f(x) = \sum_{n=-\infty}^{\infty} c_n \exp(inkx). \tag{A.12}$$

In the complex notation Equations A.2-A.4 may be simplified. The resulting orthogonality relations are then given in the simpler form

$$\int_{x_o}^{x_o+L} \exp(-irkx)\exp(ipkx)\,\mathrm{d}x = \begin{cases} L, & \text{for } r = p, \\ 0, & \text{for } r \neq p > 0, \end{cases} \tag{A.13}$$

where the complex series is multiplied by the term $\exp(-irkx)$. Recall that $k = 2\pi/L$, similar to the derivations above. The corresponding complex Fourier coefficients are given by:

$$c_n = \frac{1}{L}\int_{x_o}^{x_o+L} f(x)exp(-inkx)\,\mathrm{d}x. \tag{A.14}$$

The complex Fourier coefficients have the following relations to the coefficients generated in Equations A.9 and A.10:

$$\begin{aligned} c_n &= (a_n - ib_n)/2, \\ c_{-n} &= (a_n + ib_n)/2. \end{aligned} \tag{A.15}$$

Regardless of the way the Fourier series is expressed the goal is always to compute the coefficients to expand a function as a Fourier series [31, 34].

A.4 The Fourier Transform

The Fourier transform is a generalization of the Fourier series of a function, $f(x)$, given over an infinite interval (i.e. $x \to \infty$) which is assumed to be periodic even though the function appears to lack any particular periodicity. The result is still defined in terms of the superposition of sinusoidal waves. The requirement of such a function in this representation is that $\int_{-\infty}^{\infty}|f(x)|dx$ is finite [47].

Recall the complex Fourier series notation given in Equation A.12. As the period becomes infinite, the *frequency quantum*, $\Delta k = 2\pi/L$, becomes infinitesimal and the allowed frequencies given by $k_n = 2\pi n/L$ become continuous.

For the purposes of this thesis the spatial frequency or *wavenumber*, σ with units of cm^{-1}, is used in place of the angular frequency, k, where $k = 2\pi\sigma$. Since it is common practice in spectroscopy to express the derived spectrum in wavenumber, the final steps of the derivation will be performed by substituting angular frequency for wavenumber. The complex Fourier series and coefficients may then be written respectively as:

$$f(x) = \sum_{n=-\infty}^{\infty} c_n \exp(i2\pi\sigma_n x) \tag{A.16}$$

and

$$c_n = \Delta\sigma \int_{-L/2}^{L/2} f(x)e^{-i2\pi\sigma_n x}\,\mathrm{d}x, \tag{A.17}$$

where the boundary of the integral has been shifted for symmetry. When Equations A.16

and A.17 are combined, the result may be expressed in the general form of

$$f(x) = \sum_{n=-\infty}^{\infty} \Delta\sigma \int_{-L/2}^{L/2} f(u) e^{-i2\pi\sigma_n u}\, e^{i2\pi\sigma_n u}\, \mathrm{d}u. \tag{A.18}$$

Assuming then that L tends towards infinity, then $\Delta\sigma$ becomes infinitesimal and the summation becomes an integral [114, 35]. The result is *Fourier's inversion theorem* [47]:

$$f(x) = \int_{-\infty}^{\infty} e^{i2\pi\sigma x}\, \mathrm{d}\sigma \int_{-\infty}^{\infty} f(u) e^{-i2\pi\sigma u}\, \mathrm{d}u. \tag{A.19}$$

Fourier's inversion theorem states that in general a function can be recovered from its Fourier transform [35, 115]. The implication is if the frequency and phase information of a particular wave are known, then the original wave can be determined. How Equation A.19 may then be interpreted is

$$f(x) = \mathscr{F}^{-1}[\widetilde{f}(\sigma)] = \int_{-\infty}^{\infty} \widetilde{f}(\sigma) e^{i2\pi\sigma x}\, \mathrm{d}\sigma, \tag{A.20}$$

which is defined as the *inverse Fourier transform* [34, 35, 115]. Here $\mathscr{F}^{-1}$ represents the inverse Fourier transform and $\widetilde{f}(\sigma)$ is the Fourier transform, denoted as $\mathscr{F}$, of $f(x)$. From Fourier's inversion theorem we likewise find the *Fourier transform*, which is defined as

$$\widetilde{f}(\sigma) = \mathscr{F}[f(x)] = \int_{-\infty}^{\infty} f(x) e^{-i2\pi\sigma x}\, \mathrm{d}x. \tag{A.21}$$

Thus the Fourier transform and its inverse define the relationship between the spatial and spectral domains [27, 34, 35].

A.5 Properties of Fourier Transforms

This section outlines some properties of the Fourier transform which were used throughout this work. A comprehensive list of properties is given in Table A.1, though the focus of this section will be on symmetry, translation, and common transform pairs..

A.5.1 Symmetry

As was discussed in Chapter 2, an ideal Michelson interferometer produces an intrinsically symmetric interferogram. It is useful to review the symmetry properties of the Fourier transform. These properties become readily apparent when Euler's law is applied to Equation 2.1:

$$f(x) = \int_{-\infty}^{\infty} [a(\sigma)\cos(2\pi\sigma x) + ib(\sigma)\sin(2\pi\sigma x)]\, \mathrm{d}x = f_c(x) + f_s(x). \tag{A.22}$$

Here $a(\sigma)$ and $b(\sigma)$ are the Fourier coefficients, where $c(\sigma) = a(\sigma) + ib(\sigma)$. $a(\sigma)$ contains only even terms and $b(\sigma)$ contains only odd terms [34]. The resulting terms, $f_c(x)$ and $f_s(x)$, are the *inverse Fourier cosine transform* and *inverse Fourier sine transform* of $a(\sigma)$ and $b(\sigma)$ respectively [47].

Table A.1: Comprehensive list of Fourier Transform properties as they relate to FTS. The Fourier transform of $f(x)$ is denoted by $\widetilde{f}(\sigma)$.

Operation	$f(x)$	$\mathscr{F}[f(x)]$
Addition	$f_1(x)+f_2(x)$	$\widetilde{f_1}(\sigma)+\widetilde{f_2}(\sigma)$
Scalar Multiplication	$kf(x)$	$k\widetilde{f}(\sigma)$
Reversal	$f(-x)$	$\widetilde{f}(-\sigma)$
Symmetry	$\widetilde{f}(-x)$	$f(-\sigma)$
Scaling (a $\in \mathbb{R}$)	$f(ax)$	$\frac{1}{\lvert a\rvert}\widetilde{f}\left(\frac{\sigma}{a}\right)$
OPD Shift	$f(x-x_0)$	$\widetilde{f}(\sigma)e^{-i2\pi\sigma x_0}$
Frequency Shift ($\omega_0 \in \mathbb{R}$)	$f(x)e^{i2\pi\omega_0 x}$	$\widetilde{f}(\sigma-\sigma_0)$
OPD Convolution	$f_1(x)*f_2(x)$	$\widetilde{f_1}(\sigma)\widetilde{f_2}(\sigma)$
Frequency Convolution	$f_1(x)f_2(x)$	$\widetilde{f}(\sigma)*\widetilde{f}(\sigma)$
OPD Modulation	$f(x)\times\cos(2\pi\omega_0 x)$	$\frac{1}{2}\widetilde{f}(\sigma-\sigma_0)+\frac{1}{2}\widetilde{f}(\sigma+\sigma_0)$
OPD Differentiation	$\frac{\mathrm{d}^n f(x)}{\mathrm{d}x^n}$	$(i2\pi\sigma)^n\widetilde{f}(\sigma)$
OPD Integration	$\int_{-\infty}^{x} f(x')\,\mathrm{d}x'$	$\frac{\widetilde{f}(\sigma)}{i2\pi\sigma}+\pi\widetilde{f}(0)\delta(\sigma)$

Using Fourier's inversion theorem, the symmetry properties of the Fourier transform allow for an alternate form of analysis. Consider an even function $f_e(x)$ given a general form:

$$f_e(x)=\cos(2\pi\sigma_0 x), \tag{A.23}$$

where σ_0 is the spatial frequency. The Fourier transform of such as function is given as [35, 47, 115]:

$$\widetilde{f_e}(\sigma)=\mathscr{F}[f_e(x)]=\int_{-\infty}^{\infty}\frac{1}{2}\delta(\sigma\mp\sigma_0)\,\mathrm{d}\sigma, \tag{A.24}$$

where δ is the *Dirac delta function*, or more commonly just the *delta function* [47, 35, 116]. The delta function is defined as

$$\int_{-\infty}^{-\infty}\delta(\sigma-\sigma_0)\,\mathrm{d}\sigma=\begin{cases}1, & \text{for } \sigma=\sigma_0.\\ 0, & \text{for } \sigma\neq\sigma_0.\end{cases} \tag{A.25}$$

Since the range of the even function is symmetric about $x=0$, the result is likewise symmetric due to the inherent symmetry of the Fourier transform. Thus the unit amplitude expected from the definition of the delta function is split between the delta functions in both the positive and negative frequencies [34, 35]. The negative frequencies produced by the Fourier transform are non-physical and typically discarded [27].

The derivation of a corresponding relation for an odd function, $f_o(x)$, is similar to the derivation above. Considering a function

$$f_o(x)=\sin(2\pi\sigma_0 x), \tag{A.26}$$

The Fourier transform of $f_o(x)$ is defined as

$$\int_{-\infty}^{-\infty} \widetilde{f}_o(\sigma)\, d\sigma = \pm\frac{i}{2}\int_{-\infty}^{\infty} \delta(\sigma \mp \sigma_0)\, d\sigma = \begin{cases} \frac{i}{2}, & \text{for } \sigma = \sigma_0. \\ \frac{-i}{2}, & \text{for } \sigma = -\sigma_0. \\ 0, & \text{for } \sigma \neq \pm\sigma_0. \end{cases} \tag{A.27}$$

Thus the Fourier transform of a real asymmetric function is an imaginary asymmetric function, whereas the Fourier transform of a real symmetric function is a real symmetric function. In general, an arbitrary function is asymmetric and, by Fourier decomposition, can be represented as a sum of even and odd terms [31, 35]. Consequently, the Fourier transform contains real and imaginary components. A full list of the symmetry properties of Fourier transform pairs is given in Table A.2.

Table A.2: Symmetry properties of Fourier transform pairs. $f(x)$ is an arbitrary function and $\widetilde{f}(\sigma)$ is the Fourier transform of $f(x)$.

$f(x)$		$\widetilde{f}(\sigma)$	
Real	Imaginary	Real	Imaginary
even	0	even	0
odd	0	0	odd
0	even	0	even
0	odd	odd	0
asymmetric	0	even	odd
0	asymmetric	odd	even
even	odd	asymmetric	0
odd	even	0	asymmetric
even	even	even	even
odd	odd	odd	odd
asymmetric	asymmetric	asymmetric	asymmetric

A.5.2 Translation

The translation property of the Fourier transform defines the relationship between translation and phase, as discussed in Section 2.6. A translation, or shift, can occur in either optical path difference (OPD) or frequency, though in FTS the shift is almost exclusively in the OPD. A arbitrary shift in OPD of x_0 for a function $f(x)$ modifies Equation A.21 with a change of variable to

$$\mathscr{F}[f(x+x_0)] = \int_{-\infty}^{\infty} f(u)e^{-i2\pi\sigma(u-x_0)}\, du = \int_{-\infty}^{\infty} f(u)e^{-i2\pi\sigma u}e^{i2\pi\sigma x_0}\, dx, \tag{A.28}$$

where $u = x + x_0$. Here the term $e^{i2\pi\sigma x_0}$ is constant and may be pulled out of the integral

such that

$$\mathscr{F}[f(u)] = e^{i2\pi\sigma x_0}\int_{-\infty}^{\infty} f(u)e^{-i2\pi\sigma u}\,\mathrm{d}x = e^{i2\pi\sigma x_0}\widetilde{f}(\sigma). \tag{A.29}$$

The result of Equation A.29 indicates the introduction of a phase in the system. For example, as discussed in Chapter 2 if ZPD is not sampled exactly it corresponds to an introduction of phase. Let $\phi = 2\pi\sigma x_0$, then the introduced phase becomes apparent using Euler's law:

$$\mathscr{F}[f(u)] = e^{i\phi}\widetilde{f}(\sigma) = \cos(\phi)\widetilde{f}(\sigma) + i\sin(\phi)\widetilde{f}(\sigma). \tag{A.30}$$

The implications of the introduction of a phase due to a translation in OPD as they relate to FTS are explored in Section 2.6.2.

A.5.3 Transform Pairs

There are many functions commonly encountered in Fourier analysis, with sine and cosine be the most common [115, 35]. As shown above, the transform pairs of the sine and cosine functions are a superposition of Dirac delta functions. This section will explore other common functions seen throughout this work. The first is the *Gaussian function*, which takes the form e^{-ax^2} where a is a constant. The Fourier transform of a Gaussian function is another Gaussian function:

$$e^{-ax^2} = \int_{-\infty}^{\infty}\sqrt{\frac{\pi}{a}}e^{-\frac{(\pi\sigma)^2}{a}}e^{i2\pi\sigma x}\,\mathrm{d}\sigma \tag{A.31}$$

and

$$\sqrt{\frac{\pi}{a}}e^{-\frac{(\pi\sigma)^2}{a}} = \int_{-\infty}^{\infty} e^{-ax^2}e^{-i2\pi\sigma x}\,\mathrm{d}x. \tag{A.32}$$

By defining the constant as $a = \pi$, these equations are further simplified as:

$$e^{-\pi x^2} = \int_{-\infty}^{\infty} e^{-\pi\sigma^2}e^{i2\pi\sigma x}\,\mathrm{d}\sigma \tag{A.33}$$

and

$$e^{-\pi\sigma^2} = \int_{-\infty}^{\infty} e^{-\pi x^2}e^{-i2\pi\sigma x}\,\mathrm{d}x. \tag{A.34}$$

The Gaussian function approximates the spectral profile produced by a grating dispersion system (Chapter 3).

The second function commonly encountered is the *boxcar function*, which is defined as

$$\Pi(x) = \begin{cases} 1, & \text{for } |x| < L, \\ 0, & \text{for } |x| > L. \end{cases} \tag{A.35}$$

The boxcar function is fundamental to the FTS as it is responsible for the instrumental line shape, which is discussed in Section 2.4.4. The Fourier transform of the boxcar function, as shown in Bracewell [35], is

$$\mathscr{F}[\Pi(x)] = \int_{-\infty}^{\infty}\Pi(x)e^{i2\pi\sigma x}\,\mathrm{d}x = 2L\frac{\sin(2\pi\sigma L)}{2\pi\sigma L}, \tag{A.36}$$

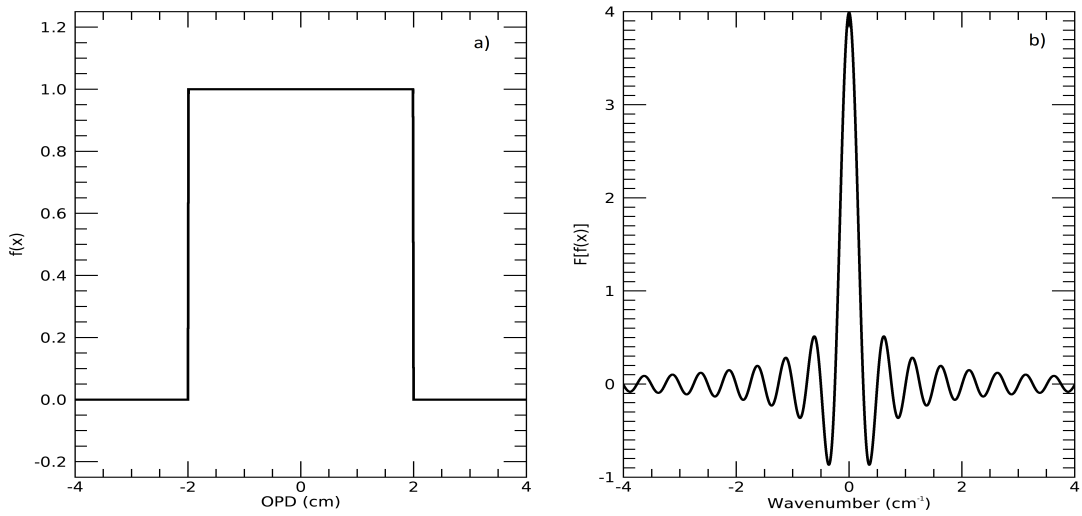

Figure A.2: The Fourier transform of the boxcar function. The boxcar function is given in panel a), and its transform pair, the sinc function, is shown in panel b).

where the term $\frac{\sin(2\pi\sigma L)}{2\pi\sigma L}$ is referred to as the *sinc function*, $\mathrm{sinc}(2\pi\sigma L)$. As previously mentioned, the sinc function is commonly encountered in Fourier analysis and the properties of the sinc function are therefore well understood. The sinc function has a full-width at half-maximum (FWHM) of $\frac{1.207}{2L}$, and crosses zero when σ is an integer multiple of $1/2L$ [35, 115]. The boxcar function and its transform are shown in Figure A.2.

The final function that will be explored is the *Dirac comb*, which relates a continuous function to a discretely sampled function. The Dirac comb is defined as

$$\text{Ш}(ax) = \frac{1}{|a|}\sum_{n=-\infty}^{\infty}\delta\left(x-\frac{n}{a}\right), \tag{A.37}$$

where a is the sampling interval, which is defined as Δx for an FTS. From Davis *et al.* [27], the Fourier transform of a Dirac comb is another Dirac comb scaled by a:

$$\text{Ш}(ax) = \int_{-\infty}^{\infty}\text{Ш}\left(\frac{\sigma}{a}\right)e^{i2\pi\sigma x}d\sigma, \tag{A.38}$$

and

$$\text{Ш}\left(\frac{\sigma}{a}\right) = a\sum_{n=-\infty}^{\infty}\delta(x-an) = \int_{-\infty}^{\infty}\text{Ш}(ax)e^{-i2\pi\sigma x}dx. \tag{A.39}$$

From these equations it can be seen that for finite sampling, doubling the spectral resolution requires sampling over twice the distance at the same interval [27].

Appendix B

The Phase Correction Function

Understanding the nature and derivation of the phase correction function (PCF) provides diagnostic insights into the process of phase corrections. An important feature of the PCF is that it must by definition be real.

$$PCF(x) = \mathscr{F}^{-1}[e^{-i\phi(\sigma)}] = \int_{-\infty}^{\infty} e^{-i\phi(\sigma)} e^{i2\pi\sigma x}\, \mathrm{d}\sigma. \tag{B.1}$$

Recall the dependence of phase on the spatial frequency ($\phi \equiv \phi(\sigma)$) and the definition of the PCF above. Using Euler's law, the PCF becomes

$$PCF = \int_{-\infty}^{\infty} \cos(\phi) e^{i2\pi\sigma x}\, \mathrm{d}\sigma - i \int_{-\infty}^{\infty} \sin(\phi) e^{i2\pi\sigma x}\, \mathrm{d}\sigma. \tag{B.2}$$

These inverse Fourier transforms may be further reduced by analysing the properties of $\sin(\phi)$ and $\cos(\phi)$. The definition of an odd function such as $\sin(\phi)$ is given as $F_o(-\sigma) = -F_o(\sigma)$, while the definition of an even function such as $\cos(\phi)$ is given as $F_e(-\sigma) = F_e(\sigma)$. The Fourier transforms in Equation B.2 may be modified using these definitions. Consider an odd function $F_o(\sigma)$, the inverse transform is given as

$$f(x) = \int_{-\infty}^{\infty} F_o(\sigma) e^{i2\pi\sigma x}\, \mathrm{d}\sigma, \tag{B.3}$$

where Euler's law is applied to $e^{i2\pi\sigma x}$, yielding

$$f(x) = \int_{-\infty}^{\infty} F_o(\sigma) \cos(2\pi\sigma x)\, \mathrm{d}\sigma + i \int_{-\infty}^{\infty} F_o(\sigma) \sin(2\pi\sigma x)\, \mathrm{d}\sigma. \tag{B.4}$$

Since the product of even function and odd function is an odd function and the integral is symmetric, the first term vanishes. Consequently

$$f(x) = i \int_{-\infty}^{\infty} F_o(\sigma) \sin(2\pi\sigma x)\, \mathrm{d}\sigma. \tag{B.5}$$

By symmetry, Equation B.5 may be further reduced to

$$f(x) = 2i \int_{0}^{\infty} F_o(\sigma) \sin(2\pi\sigma x)\, \mathrm{d}\sigma. \tag{B.6}$$

Similarly, an even function, $F_e(\sigma)$, can be simplified as

$$f(x) = 2\int_0^\infty F_e(\sigma)\cos(2\pi\sigma x)\,\mathrm{d}\sigma. \tag{B.7}$$

Recall that $\phi \equiv \phi(\sigma)$. Thus the even and odd functions may be defined as $F_e = \cos(\phi)$ and $F_o = \sin(\phi)$ respectively. By combining Equations B.2, B.6, and B.7 the result is

$$\mathrm{PCF} = 2\int_0^\infty \cos(\phi)\cos(2\pi\sigma x)\,\mathrm{d}\sigma + 2\int_0^\infty \sin(\phi)\sin(2\pi\sigma x)\,\mathrm{d}\sigma, \tag{B.8}$$

which has no imaginary component. The lack of an imaginary component in the PCF serves as a useful check during algorithm development.

Appendix C

Laser Diode Calibration

As discussed in Chapter 3, a source module was required to investigate the performance of the PDPFTS capable of producing both continuum and unresolved line emission. The unresolved line emission by the output of a photomixer illuminated by two lasers, with the heterodyne difference frequency being emitted by the photomixer. In order to determine the THz differential frequency generated by the photomixer, it was important to establish the frequency dependence of the individual lasers. The laser frequency is primarily dependent upon the temperature, but also the laser current to a lesser extent.

Each photomixer incorporated two Fitel laser diodes [98] (see Table C.1), each with differing nominal frequencies based on the laser output at 25°C using the maximum drive current (200 mA). A series of measurements were taken using an Exfo WA-1500 Wavemeter [117]. Each diode was connected to a Koheron CTL200-2 digital laser diode controller (Koheron) [111]. The Koheron controls the laser temperature using a *thermoelectric cooler* (TEC) measuring fluctations in resistance with a *thermistor*. The relationship between temperature and resistance is given by the *Steinhart-Hart equation*, which depends upon the calibration of a given thermistor.

Initially, the power output of the system was too great for the wavemeter, resulting in saturation of the detector. A custom attenuator was incorporated into the feed of the wavemeter, the addition of which proved sufficient to attenuate the signal such that the detector was no longer saturated.

Each diode was measured at two temperatures, which were based both on the limits of the laser diode and the Koheron. The minimum consistent temperature was $\sim$16.2°C with the TEC was set to 14.9 kΩ. The maximum temperature was set to 35°C, which corresponds to 6545 Ω, based on the safe operating limit of the laser diode. The frequency of the diode at each of these temperatures was measured twice, once with a current of 50 mA, and again with a current of 100 mA.

Three of the diodes are near their nominal frequencies: the FOL15DCWD-19300-SNL (193.00 THz), FOL15DCWD-19338-SNL (193.38 THz), and FRL15DCWD-A81-19375 (193.75 THz). The FRL15DCWD-A81-19450 (194.50 THz) was an outlier, consistently measuring above its nominal frequency. Each of the diodes exhibited a temperature response of -0.012 THz/K, which agrees with previous measurements [87]. A look-up table was generated from the results (Figure C.1). Clearly the effective range of the photomixer given any combination of the laser diodes can be extrapolated as roughly 3.9 - 60 cm^{-1}. I developed an algorithm to determine possible laser combinations and temperature differences required for a given wavenumber.

Table C.1: Typical technical specification sheet for the Fitel laser diodes [98].

1550nm CW DFB Laser Diode Module

FRL15DCWA-Axx-xxxxx-x
FRL15DCWB-Axx-xxxxx-x
FRL15DCWD-Axx-xxxxx-x

1. Absolute Maximum Ratings

Parameters	Sym.	Min.	Max.	Unit	Condition
Storage Temperature	Tstg	-40	85	°C	
Case Operating Temperature	Tc	-5	70	°C	
LD Operating Temperature	T_{LD}	20	35	°C	
LD Forward Current	IfLD	-	350	mA	
LD Reverse Voltage	VrLD	-	2	V	
PD Forward Current	IfPD	-	5	mA	
PD Reverse Voltage	VrPD	-	20	V	
TEC Current	Itec	-	1.6	A	
TEC Voltage	Vtec	-	2.6	V	
Relative Humidity	RH	0	85	%	
Fiber Bend Radius	-	30	-	mm	
Fiber Axial Pull Force	-	-	10	N	
Lead Soldering Temperature	-	-	260	°C	
Lead Soldering Duration	-	-	10	sec	
Torque Force (Flatness : <20μm)	-	-	0.1	Nm	

2. Performance Specifications (Tc=25°C, BOL unless otherwise specified)

Parameters	Sym.	Min.	Typ.	Max.	Unit	Condition
Optical Output Power						
FRL15DCWA	Pf	10	-	-	mW	CW
FRL15DCWB		20	-	-		
FRL15DCWD		40	-	-		
LD Forward Current						
FRL15DCWA	If	-	-	80	mA	Rated Power
FRL15DCWB		-	-	150		
FRL15DCWD		-	-	300		
LD Operating Temperature	T_{LD}	20	-	35	°C	Rated power, CW
LD Forward Voltage						
FRL15DCWA,B	Vf	-	-	1.8	V	Rated power, CW
FRL15DCWD		-	-	2.5		
LD Threshold Current	Ith	-	15	40	mA	BOL
Peak Emission Wavelength	λ	λ_{-ITU}-0.1	λ_{-ITU}	λ_{-ITU}+0.1	nm	Rated Power, CW
Spectral Linewidth						
FRL15DCWA, B, D		-	-	10		Rated Power, CW
FRL15DCWA, B, D	Δν	-	-	5	MHz	Rated Power, CW, Optional (-A)
FRL15DCWA, B, D		-	-	2		Rated Power, CW, Optional (-B)
FRL15DCWD		-	-	1		Pf=40mW, CW, Optional (-C)
Side Mode Suppression Ratio	SMSR	35	45	-	dB	Rated Power,CW
Optical Isolation	Iso	30	-	-	dB	FWHM, Rated Power, CW
Relative Intensity Noise						
FRL15DCWA	RIN	-	-	-133	dB/Hz	CW, Op_{RL}<-25dB, 100MHz<f<10GHz
FRL15DCWB		-	-	-138		
FRL15DCWD		-	-	-140		
Monitor Current						
FRL15DCWA	Im	0.05	-	1	mA	Rated power, CW, VrPD=5V
FRL15DCWB		0.1	-	2		
FRL15DCWD		0.15	-	3		
Monitor Dark Current	Id	-	-	100	nA	VrPD=5V
Tracking Error	TE	-0.5	-	0.5	dB	Tc=-5°C/25°C/70°C, Im=const.
TEC Current	Itec	-	-	1.2	A	Tc=70°C, Rated Power, CW
TEC Voltage	Vtec	-	-	2.4	V	Tc=70°C, Rated Power, CW
Thermistor Resistance	Rth	9.5	-	10.5	kΩ	T_{LD}=25°C
Thermistor B Constant	Bth	-	3900	-	K	T_{LD}=25°C
Polarization Extinction Ratio	Er	20	-	-	dB	Rated power, CW

BOL:Beginning of Life, Op_{RL}:Optical Return Loss

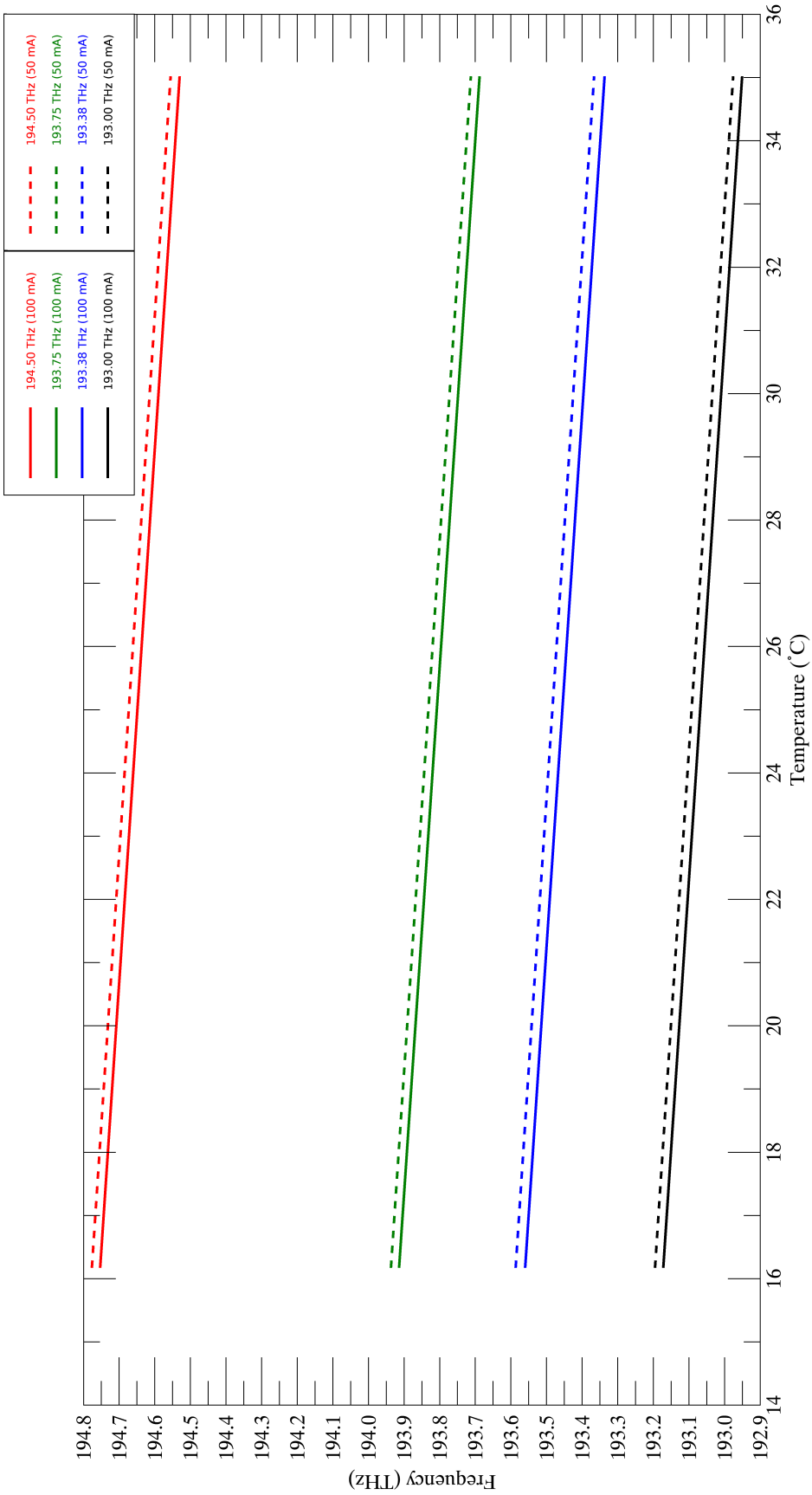

Figure C.1: Calibration of the lasers used in the photomixers showing the strong dependence of frequency on temperature and the weaker dependence on laser current. Two photomixer combinations can be nulled when the 194.50 THz and 193.38 THz lasers are at 16.2°C and 35.4°C, and the 193.75 THz and 193.00 THz lasers are at 35.7°C and 16.2°C respectively (see Chapter 3).